ISTANBUL TECHNICAL UNIVERSITY ★ GRADUATE SCHOOL

PRODUCTION and CHARACTERIZATION of W-Ni MATRIX COMPOSITES REINFORCED with CeB_6, NdB_6, ErB_4 PARTICULATES by POWDER METALLURGY METHODS

M.Sc. THESIS

Burçak BOZTEMUR

Department of Metallurgical and Materials Engineering

Ceramic Engineering Programme

JULY 2022

ISTANBUL TECHNICAL UNIVERSITY ★ GRADUATE SCHOOL

PRODUCTION and CHARACTERIZATION of W-Ni MATRIX COMPOSITES REINFORCED with CeB_6, NdB_6, ErB_4 PARTICULATES by POWDER METALLURGY METHODS

M.Sc. THESIS

Burçak BOZTEMUR
(506201302)

Department of Metallurgical and Materials Engineering

Ceramic Engineering Programme

Thesis Advisor: Assoc. Prof. Dr. Duygu AĞAOĞULLARI

JULY 2022

İSTANBUL TEKNİK ÜNİVERSİTESİ ★ LİSANSÜSTÜ EĞİTİM ENSTİTÜSÜ

CeB_6, NdB_6, ErB_4 PARTİKÜLLERİ ile TAKVİYE EDİLMİŞ W-Ni MATRİS KOMPOZİTLERİN TOZ METALURJİSİ YÖNTEMLERİ ile ÜRETİMİ ve KARAKTERİZASYON ÇALIŞMALARI

YÜKSEK LİSANS TEZİ

Burçak BOZTEMUR
(506201302)

Metalurji ve Malzeme Mühendisliği Anabilim Dalı

Seramik Mühendisliği Programı

Tez Danışmanı: Doç. Dr. Duygu AĞAOĞULLARI

TEMMUZ 2022

Burçak BOZTEMUR, a M.Sc. student of ITU Graduate School student ID 506201302 successfully defended the thesis entitled "PRODUCTION and CHARACTERIZATION of W-Ni MATRIX COMPOSITES REINFORCED with CeB_6, NdB_6, ErB_4 PARTICULATES by POWDER METALLURGY METHODS", which she prepared after fulfilling the requirements specified in the associated legislations, before the jury whose signatures are below.

Thesis Advisor :	**Assoc. Prof. Dr. Duygu AĞAOĞULLARI** Istanbul Technical University	.....
Jury Members :	**Prof. Dr. M. Lütfi ÖVEÇOĞLU** Istanbul Technical University	.....
	Doç. Dr. Nazlı AKÇAMLI Bursa Technical University	.....

Date of Submission : 08 July 2022
Date of Defense : 22 July 2022

To my wonderful family,

FOREWORD

I am grateful for the experience to work in ITU Particulate Materials Laboratory (PML) under the supervision of Assoc. Prof. Dr. Duygu AĞAOĞULLARI. I would like to thank Assoc. Prof. Dr. Duygu AĞAOĞULLARI who has always answered my questions, supported me, guided through my studies and showed me alternative solutions. I would like to thank Prof. Dr. M. Lütfi ÖVEÇOĞLU who introduced me to ITU Particulate Materials Laboratory, support me with TÜBİTAK 119M980 project and whom I admire for both of his knowledge and expertise. This project was supported from ITU BAP (Project no: MYL202243606).

I also would like to thank Dr. Hasan GÖKÇE, Prof. Dr. Hüseyin ÇİMENOĞLU, Prof. Dr. Murat BAYDOĞAN, Prof. Dr. C. Bora DERİN and Doç. Dr. Nuri SOLAK for helping me by letting me to work on their facilities and sharing their experience.

I also would like to thank Prof. Dr. Laima Luo, Prof. Dr. Fei Sun, Assoc. Prof. Jing Wang and Dr. Yue Xu in HFUT for helping me for experiments carrying out in China.

Special thanks to Halil ŞENOL and M. Sc. Ammar ALKRAIDI for contributions to this work and their friendship. Res. Assist. Mümin BIYIKLIOĞLU, Res. Assist. Sıddıka MERTDİNÇ, Res. Assist. İlayda SÜZER, M. Sc. Amir AKBARİ, Cem ÇİÇEK and M. Sc. Sina KAVAK for their friendship during this work. I am especially grateful to work with such amazing people at ITU PML where I have worked with a cheerful and committed group.

I am also thankful to Res. Assist. Mertcan KABA for helping on mechanical test experiments. Also, Res. Assist. Faruk KAYA for his help during my FACTSAGE and rietveld analysis. They have contributed to this work considerably.

Finally, my parents Sultan BOZTEMUR and Metin BOZTEMUR should take all the credit especially during these periods. Also, I am thankful to my brother Burak BOZTEMUR for carrying me to school, it was very long way.

July 2022

Burçak BOZTEMUR
(Metallurgy and Material Engineer)

TABLE OF CONTENTS

Page

ABBREVIATIONS

BCC : Base Centered Cubic
CIP : Cold-isostatic Pressing
EDS : Energy Dispersive X-Ray Spectroscope
FCC : Face Centered Cubic
HCP : Hexagonal Closed Packed
HFUT : Hefei University of Technology
ITER : International Thermonuclear Experimental Reactor
ITU : Istanbul Technical University
LPG : Liquefied Petroleum Gas
MA : Mechanical Alloying
PFM : Plasma Facing Materials
PM : Powder Metallurgy
PS : Pressureless Sintering
PSIEC : Plasma-Surface Interaction System under Extreme Conditions
SEM : Scanning Electron Microscope
SPS : Spark Plasma Sintering
TEM : Transmission Electron Microscope
XRD : X-Ray Diffractometer

SYMBOLS

%	**:** Percentage
at%	**:** Atomic percentage
wt%	**:** Weight percentage
°C	**:** Celsius Degree
Hz	**:** Hertz
K	**:** Kelvin
µm	**:** Micrometer
nm	**:** Nanometer
h	**:** Hour
s	**:** Second
g	**:** Gram
min	**:** Minute
Pa	**:** Pascal
MPa	**:** Mega Pascal
GPa	**:** Giga Pascal
mm	**:** Millimeter
cm	**:** Centimeter
ml	**:** Milliliter
rpm	**:** Revolutions Per Minute
mm^2	**:** Millimeter Square
m^2	**:** Meter Square
N	**:** Newton
kN	**:** Kilonewton
cm^3	**:** Cubic Centimeter
M	**:** Molar
2-D	**:** Two-Dimensional
mA	**:** Milliampere
kV	**:** Kilovolt
Å	**:** Angstrom
ρ	**:** Density

atm **:** Atmosphere

kJ **:** Kilojoule

ΔH **:** Enthalpy

ΔG **:** Gibbs Free Energy

dk **:** Dakika

sn **:** Saniye

sa **:** Saat

H_2 **:** Hydrogen

Ar **:** Argon

He **:** Helium

mS **:** Milisiemens

LIST OF TABLES

Page

LIST OF FIGURES

Page

PRODUCTION and CHARACTERIZATION of W-Ni MATRIX COMPOSITES REINFORCED with CeB_6, NdB_6, ErB_4 PARTICULATES by POWDER METALLURGY METHODS

SUMMARY

Energy is the most important topic for centuries. An alternative energy resource should be considered for the survival of humanity and environment because of decreasing resources of energy. Although, fusion is not commercialized yet, it has the potential to be an excellent alternative even to renewable energy resources due to its lack of radioactive waste and harmful emissions. There are many types of fusion energy. Tokamak where magnets form a donut shape is one of fusion energy type. Many experiments have been carried out in these Tokamaks all over the world, the largest currently being built in France, known as ITER (International Thermonuclear Experimental Reactor). Plasma facing materials (PFMs), which act as the protective armor of fusion reactors and directly face the huge energy from fusion reactions, become one of the main problems that limit the practical application of fusion reactions.

Tungsten (W) and its alloys are considered to be the most promising PFM candidates as the armor material in divertor components due to its high melting point, high strength at elevated temperatures, high elastic modulus, low thermal expansion, high thermal conductivity, high sputtering threshold, low hydrogen isotope retention, high resistance to neutron damage and low activation compared to other fusion relevant materials. However, the extremely harsh operational environment in the fusion reactor would inevitably result in serious performance degradation of PFMs. Under helium ion irradiation, the microstructure of tungsten-based materials is obviously changed and causes the brittleness of materials. Under the thermal shock loads, the W-based materials experience severe plastic deformation and crack growth. Therefore, improving the resistance of helium ion irradiation and thermal shock is of vital importance for engineering application. In order to overcome the severe problems of W-based materials which are hard to produce due to its high melting point, researchers investigated grain refinement, second phase addition and deformation. The most valid technique proposed to overcome these difficulties is the method called activated sintering. Activated sintering is the process of improving sinterability as a result of small additives to the powder composition or various changes made in the sintering atmosphere. In order to achieve activated sintering, the metal with a low melting temperature (various transition metals such as Pd, Pt, Ni, Cu, Co and Fe) must be dissolved in the metal with a high melting temperature. In this way, the sintering path is shortened and the process is facilitated. In addition, up to now, various carbides and nitrides such as TiC, ZrC, HfC, TiN, various oxides such as La_2O_3, Y_2O_3, HfO_2, Sm_2O_3, ThO_2 and various borides such as TiB_2, HfB_2, ZrB_2, CrB_2 were incorporated into W matrix to form composites. It has been revealed that composites which are reinforced with oxide, carbide, nitride, boride phases offer better and superior mechanical properties. Moreover, oxide, boride or carbide reinforced and activated

sintered W matrix composites such as W-Cu-CeO_2, W-Ni-TiC-Y_2O_3, W-Cu-Ni-Y_2O_3, W-Ni-La_2O_3, W-Ni-TiB_2, W-Ni-TiB_2-La_2O_3, etc. exhibit enhanced microstructural and mechanical properties.

In this study, CeB_6, NdB_6 and ErB_4 rare-earth borides were produced with mechanochemical synthesis. Different milling time (0, 2, 3, 4, 5, 6, 7 and 8 h) and speed (920 and 1188 rpm) were tried for production. Also, 5 h and 920 rpm were used for optimization of milling. For this process, stainless steel balls and vials were used. Then, pure boride powders were synthesized after HCl leaching process. 99 wt% W and 1 wt% Ni were mechanically alloyed for 800 rpm and 6 h. For all process, WC balls and vials were used and a ball-to-powder weight ratio was 10:1. After that, rare-earth boride powders (1, 2, 5 and 10 wt%) were added into W1Ni with 6 h mechanical alloying.

For phase characterization of composite powders, XRD was used: four main W peaks were obtained with small amount WC impurity. The lattice strains and crystallite sizes of the milled powders were calculated with TOPAS software based on the XRD patterns. When the lattice strains increased, the crystallite sizes decreased because of the milling process. Then, density of powders was measured using a He gas pycnometer. When amount of rare-earth boride particulate increased, density of W1Ni composite powders decreased. Particle size of powders was measured with ethanol solution and lognormal distribution was obtained. Also, particle sizes were decreasing with increasing amount of reinforcing. Powder morphology, size and distribution were determined with SEM/EDS. TEM analysis was done for NdB_6 and ErB_4 powders.

After powder characterization, two different methods that are pressureless sintering and spark plasma sintering were used for consolidation of powders. Before pressureless sintering, powders were compacted 13 mm diameter and 5 mm height with hydraulic pressing (480 MPa, 1 min) and cold isostatic pressing (390 MPa, 1 min). Then, pressureless sintering was applied to the bulk samples. Samples were holded in vacuum atmosphere until 100 °C. Then, Argon gas was given into chamber between 100-750 °C. Hydrogen gas was used for getting rid of oxide phases between 750-900 °C. After this period, Ar gas was used always and cooling/heating rate is 10 °C /min. These samples were holded at 1400 °C for 1 h. Producing powders were spark plasma sintered in graphite mold as 20 mm diameter and 2 mm height with graphite foils in the Hefei University of Technology (HFUT). For SPS, cooling/heating rate was 100 °C/min until 600 °C. Samples were holded 5 min at 600 °C. After that, temperature was reached to 1410 °C for 1 min with 90 °C /min and cooled. In all this process, pressure was started with 4.4 kN and increased to 9.4 kN.

After producing of bulk samples, XRD analyses were done for all samples. According to the results, four main W peaks were obtained with other smallest peaks. However, W_2B was started to be main phase after adding 5 wt% rare-earth borides. Densities of the sintered samples were measured with Archimedes' principle. The highest density was obtained for W1Ni reinforcing with 10 wt% NdB_6 particulates SPS sample that had 100% relative density. SEM/EDS was done for all samples. Three different phases as grey, black and white were determined for samples. Vicker microhardness test was done for samples at 200 gram and 10 sec. The SPS'd W1Ni sample reinforced with 10 wt% ErB_4 particulates had the highest value (21.16±0.72 GPa). After that, wear resistance test was done for samples. Wear testing conditions were selected as a sliding speed of 6 mm/s, sliding distance of 20 m and the wear track length of 2 mm. The tests were performed with a normal load of 4 N at room temperature. The SPS'd W1Ni

sample reinforced with 10 wt% ErB_4 particulates had the lowest wear volume loss (0.341×10^{-4} mm^3). Finally, He^+ irradiation tests were applied to samples in HFUT. All samples were exposed to 20-eV He^+ ion irradiation with a flux of 1.102×10^{21} ions/(m^2s). Irradiance fluence was set 1.32×10^{24} ions/m^2 with 20 min durations. After this test, XRD peaks of W1Ni and all reinforced with 2 wt% CeB_6, NdB_6, ErB_4 and 5 wt% ErB_4 pressureless sintered samples were shifting to right. Also, XRD peaks of reinforced with 1 wt% CeB_6, NdB_6, ErB_4, 5 wt% CeB_6, NdB_6 and 10 wt% ErB_4 pressureless sintered samples were shifting to left side. While 5 wt% NdB_6 pressureless sintered sample gave bad results, 2 wt% CeB_6 pressureless sintered sample had less surface deformation after irradiation test as SEM images results.

As a conclusion, two different production methods and different amounts of rare-earth boride particulates were compared in this study. Different characterization methods were used for analysing samples. Properties of W1Ni composite material was improved with adding rare-earth boride particulates. Enhanced hardness and wear resistance properties were achieved for potential high-temperature applications and fusion reactor applications.

CeB_6, NdB_6, ErB_4 PARTİKÜLLERİ ile TAKVİYE EDİLMİŞ W-Ni MATRİS KOMPOZİTLERİN TOZ METALURJİSİ YÖNTEMLERİ ile ÜRETİMİ ve KARAKTERİZASYON ÇALIŞMALARI

ÖZET

Enerji, insanlığın yüzyıllardır en önemli konularından biridir. Azalan enerji kaynakları nedeniyle insanlığın ve çevrenin devamı için alternatif bir enerji kaynakları düşünülmektedir. Füzyon henüz ticarileştirilmemiş olsa da, radyoaktif atık ve zararlı emisyon içermemesi nedeniyle yenilenebilir enerji kaynaklarına bile mükemmel bir alternatif olma potansiyeline sahiptir. Füzyon enerjisinin birçok türü vardır. Mıknatısların halka şekli oluşturduğu Tokamak, füzyon enerjisi türlerinden biridir. Dünyanın her yerinde Tokamaklar'da birçok deney gerçekleştirilmiştir, en büyüğü şu anda Fransa'da inşa edilmekte olup, ITER (Uluslararası Termonükleer Deneysel Reaktör) olarak bilinmektedir. Füzyon reaktörlerinin koruyucu zırhı görevi gören ve füzyon reaksiyonlarından kaynaklanan devasa enerjiyle doğrudan karşı karşıya olan plazma kaplama malzemeleri (PFM'ler), füzyon reaksiyonlarının pratik uygulamasını sınırlayan ana sorunlardan biri haline gelir.

Tungsten (W) ve alaşımları, yüksek ergime noktası, yüksek sıcaklıklarda yüksek mukavemet, yüksek elastik modül, düşük termal genleşme, yüksek termal iletkenlik, yüksek püskürtme eşiği, düşük hidrojen izotop tutma, nötron hasarına karşı yüksek direnç özellikleri sayesinde füzyon ile ilgili diğer malzemelere kıyasla iyi özellikler göstermektedir. Bununla birlikte, füzyon reaktöründeki aşırı zorlu çalışma ortamı, kaçınılmaz olarak PFM'lerin ciddi performans düşüşüne neden olmaktadır. Helyum iyonu ışıması altında, Tungsten bazlı malzemelerin mikro yapısı değişir ve malzemelerin kırılganlığına neden olur. Termal şok yükleri altında, W-tabanlı malzemeler ciddi plastik deformasyon ve çatlak büyümesi yaşar. Bu nedenle, helyum iyonu ışıması ve termal şok direncinin geliştirilmesi, mühendislik uygulamaları için hayati önem taşımaktadır. Araştırmacılar, yüksek ergime noktası nedeniyle üretilmesi zor olan W bazlı malzemelerin ciddi sorunlarının üstesinden gelmek için tane inceltme, ikinci faz ilavesi ve deformasyonu geliştirdiler. Bu zorlukların üstesinden gelmek için önerilen en geçerli teknik, aktifleştirilmiş sinterleme adı verilen yöntemdir. Aktif sinterleme, toz bileşimine yapılan küçük katkılar veya sinterleme atmosferinde yapılan çeşitli değişiklikler sonucunda sinterlenebilirliğin iyileştirilmesi işlemidir. Aktive edilmiş sinterlemenin sağlanabilmesi için ergime sıcaklığı düşük olan metalin (Pd, Pt, Ni, Cu, Co ve Fe gibi çeşitli geçiş metalleri), yüksek ergime sıcaklığına sahip metal içinde çözülmesi gerekir. Bu sayede sinterleme yolu kısaltılır ve süreç kolaylaşır. Ayrıca, TiC, ZrC, HfC, TiN gibi çeşitli karbürler ve nitrürler, La_2O_3, Y_2O_3, HfO_2, Sm_2O_3, ThO_2 gibi çeşitli oksitler ve TiB_2, HfB_2, ZrB_2, CrB_2 gibi çeşitli borürler W matrisine dahil edilerek kompozitler oluşturulmuştur. Oksit, karbür, nitrür, borür fazları ile takviye edilen kompozitlerin daha iyi ve gelişmiş mekanik özellikler sunduğu ortaya konmuştur. Ayrıca, W-Cu-CeO_2, W-Ni-TiC-Y_2O_3, W-Cu-Ni-Y_2O_3, W-Ni-La_2O_3, W-Ni-TiB_2, W-Ni-TiB_2-La_2O_3 vb. gibi oksit, borür veya karbür takviyeli

aktifleştirilmiş sinterlenmiş W matrisli kompozitler, gelişmiş mikroyapısal ve mekanik özellikler sergiler.

Bu çalışmada mekanokimyasal sentez ile CeB_6, NdB_6 ve ErB_4 nadir toprak borürleri üretilmiştir. Üretim için farklı öğütme süreleri (0, 2, 3, 4, 5, 6, 7 ve 8 sa) ve hız (920 ve 1188 devir/dk) denenmiştir. Ayrıca öğütmenin optimizasyonu için 5 sa ve 920 devir/dk kullanılmıştır. Bu işlem için paslanmaz çelik bilyalar ve kaplar kullanılmıştır. Daha sonra HCl liç işleminden sonra saf borür tozları sentezlenmiştir. Ağırlıkça %99 W ve ağırlıkça %1 Ni, 800 devir/dk ve 6 sa boyunca mekanik olarak alaşımlanmıştır. Tüm işlemler için WC bilyalar ve kaplar kullanılmıştır. Bilya/toz ağırlık oranı 10:1 idi. Bundan sonra, 6 sa'lik mekanik alaşımlama ile W1Ni'ye nadir toprak borür tozları (ağırlıkça %1, 2, 5 ve 10) ilave edildi.

Kompozit tozların karakterizasyonu için, fazların analizi XRD kullanılarak yapılmıştır. Az miktarda WC safsızlığı ile dört ana W piki elde edildi. Öğütülmüş tozların kafes gerilmeleri ve kristal boyutları TOPAS yazılımı ile hesaplanmıştır. Kafes gerilmeleri arttığında, öğütme işlemi nedeniyle kristalit boyutları küçülmüştür. Daha sonra He gazlarının kullanıldığı piknometre ile tozların yoğunlukları ölçüldü. Nadir toprak borür partikül miktarı arttığında, takviyeli nadir toprak borürlü W1Ni kompozitlerin yoğunluğu azalmıştır. Tozların partikül boyutu etanol çözeltisi içinde ölçülerek ve lognormal dağılım elde edildi. Ayrıca, artan takviye miktarı ile tane boyutları azalmaktadır. Toz morfolojisi, boyutu ve dağılımı SEM/EDS ile belirlendi. NdB_6 ve ErB_4 tozları için TEM analizi yapıldı.

Toz karakterizasyonundan sonra tozların konsolidasyonu için basınçsız sinterleme ve spark plazma sinterleme olmak üzere iki farklı yöntem kullanılmıştır. Basınçsız sinterleme öncesinde tozlar 13 mm çapında ve 5 mm yüksekliğinde hidrolik presleme (480 MPa, 1 dk) ve soğuk izostatik presleme (390 MPa, 1 dk) ile sıkıştırılmıştır. Daha sonra numunelere basınçsız sinterleme uygulanmıştır. Numuneler 100 °C 'ye kadar vakum atmosferinde tutulmuştur. Ardından 100-750 °C arasında odaya argon gazı verildi. 750-900 °C arasında oksit fazlarından kurtulmak için hidrojen gazı kullanılmıştır. Bu süreden sonra her zaman argon gazı kullanılmış ve soğutma/ısıtma hızı 10 °C /dk'dır. Numuneler 1400 °C 'de 1 sa tutuldu. Üretilen tozlar, Hefei Teknoloji Üniversitesi'nde (HFUT) grafit folyolarla grafit kalıpta 20 mm çapında ve 2 mm yüksekliğinde spark plazma sinterlendi. SPS için soğutma/ısıtma hızı 600 °C 'ye kadar 100 °C /dk idi. Örnekler 600 °C' de 5 dakika tutuldu. Daha sonra 1 dk 1410 °C sıcaklığa tutulmuş ve 90 °C /dk ile soğutulmuştur. Tüm bu süreçte basınç 4,4 kN ile başlatılmış ve 9,4 kN'ye yükseltilmiştir.

Tüm numuneler üretildikten sonra XRD analizi yapılmıştır. Sonuç olarak, diğer en küçük pik noktalarıyla birlikte dört ana W pik noktası elde edildi. Ancak W_2B, ağırlıkça %5 oranında nadir toprak borürleri eklendikten sonra ana faz olmaya başlamıştır. Sinterlenmiş numunelerin yoğunlukları Arşimet prensibi ile ölçülmüştür. En yüksek yoğunluk, %100 bağıl yoğunluğa sahip ağırlıkça %10 NdB_6 partikül takviyeli W1Ni SPS numunesi için elde edilmiştir. Tüm numuneler için SEM/EDS yapıldı. Örnekler için gri, siyah ve beyaz olmak üzere üç farklı faz belirlenmiştir. Numuneler için 200 g ve 10 sn'de Vicker mikrosertlik testi yapıldı. Sonuç olarak, ağırlıkça %10 ErB_4 partikül takviyeli W1Ni SPS numunesi en yüksek değere (21,16±0,72 GPa) sahipti. Daha sonra numuneler için aşınma direnci testi yapılmıştır. Aşınma testi koşulları 6 mm/s kayma hızı, 20 m kayma mesafesi ve 2 mm aşınma izi uzunluğu olarak seçilmiştir. Testler, oda sıcaklığında 4 N normal yük ile gerçekleştirilmiştir. Sonuç olarak, ağırlıkça %10 ErB_4 partikül takviyeli W1Ni SPS

numunesi en düşük aşınma hacim kaybına ($0{,}341x10^{-4}$ mm^3) sahipti. Son olarak, HFUT'ta numunelere He^+ radyasyon testleri uygulandı. Tüm numuneler, 1.102×10^{21} iyon/(m^2s) akı ile 20-eV He^+ iyon radyasyonuna maruz bırakıldı. Radyasyon akışı, 20 dakikalık sürelerle 1.32×10^{24} iyon/m^2 olarak ayarlandı. Bu testten sonra, W1Ni'nin XRD pikleri ve ağırlıkça %2 CeB_6, NdB_6, ErB_4 ve yine ağırlıkça %5 ErB_4 ile güçlendirilmiş basınçsız sinterlenmiş numunelerin XRD pikleri sağa kayıyordu. Ayrıca ağırlıkça %1 CeB_6, NdB_6, ErB_4, ağırlıkça %5 CeB_6, NdB_6 ve ağırlıkça %10 ErB_4 basınçsız sinterlenmiş numunelerin XRD pikleri sola kayıyordu. SEM sonuçları incelendiğinde, ağırlıkça %5 NdB_6 basınçsız sinterlenmiş numune kötü sonuçlar verirken, ağırlıkça %1 ErB_4 basınçsız sinterlenmiş numunede radyasyon testi sonrasında daha az yüzey deformasyonu görülmüştür.

Sonuç olarak bu çalışmada iki farklı üretim yöntemi ve farklı miktarlardaki nadir toprak borür partikülü takviyesi karşılaştırılmıştır. Örnekleri analiz etmek için farklı karakterizasyon yöntemleri kullanılmıştır. W1Ni kompozit malzemenin özellikleri, nadir toprak borür partiküllerinin eklenmesiyle iyileştirilmiştir. Yüksek sıcaklık uygulamaları ve füzyon reaktörü uygulamaları için potansiyel olarak geliştirilmiş sertlik ve aşınma direnci özellikleri elde edildi.

1. INTRODUCTION

Energy is the most important topic for centuries. Humanity can meet our needs, unfortunately with the cost of polluting the environment with waste and releasing several billion tons of CO_2 into Earth's atmosphere [1,2]. Scientists are recently interested in the signs of climate change, however it started to be obvious. Also, it is well known that most of the energy reserves such as oil and natural gas are actually limited in supply. For that reason, an alternative energy resource should be considered for the survival of humanity and environment [3,4].

Although, fusion is not commercialized yet, it has the potential to be an excellent alternative even to renewable energy resources due to its lack of radioactive waste and harmful emissions [5]. Fusion is a physical process by which atoms release energy when they are forced to gather into bigger atoms. Firstly, fusion power barely releases any CO_2. The primary energy source for stars is hydrogen fusion, which is also considered to be one of the most promising candidate sources to provide safe, environment friendly and economical energy for human beings [6]. Of all the possible fusion reactions the hydrogen isotopes deuterium-tritium (D-T) reaction is the most attractive one. If a nucleus of deuterium fuses with a nucleus of tritium, an α-particle (He) is produced and a neutron (n) is released, a very simple reaction that involves no CO_2. The nuclear rearrangement results in a reduction in total mass and a consequent release of energy in the form of the kinetic energy of the reaction products ($E=(\Delta m)c^2$). The energy released is 17.6 MeV per reaction. In macroscopic terms, just 1 kg of this fuel would release 10^8 kWh of energy and would provide the requirements of a 1 GW (electrical) power station for a day [7]. Deuterium is readily found in seawater and can be easily isolated/extracted with today's technology. For tritium, this isotope is much rarer, however, the genius of the fusion reaction is that the neutron released can be used with ^{6}Li to produce tritium. Effectively, the raw materials coming into the plant are deuterium and lithium, the latter being relatively abundant (comparable to chlorine in the earth's crust). In fission reactors, very large atoms such as uranium is split into smaller atoms such as krypton and barium, which split further and further until

radioactive nuclei are all that result. The thermal output is very large for the uranium pellets that is used in nuclear reactors, making the reactor economical in a sense. Just 20 g of uranium fuel can make as much energy as 400 kg of coal. Just a very small of uranium pellets in gram order can power a house for a year [8]. In fusion, the product again is simply He gas, the former being reused for the reaction and the latter coming in handy in a world, where helium is becoming more and more scarce. An additional bonus that is made apparent through the comparison with fission plants is that there is no possibility for a nuclear meltdown in fusion plants. Interrupting or tampering with the reaction simply returns the hot plasma at its center to regular gas. Finally, unlike renewables such as solar and wind, nuclear fusion is not at the mercy of environmental conditions meaning it can be controlled to always meet energy demand [9]. Therefore, fusion reactors are possible to obtain sustainable clean energy, and the fuel for fusion has extremely high energy density meaning that a very small amount of fuel produces a very large amount of energy.

A common approach is that of the 'Tokamak', where magnets form a donut shape the inside of which the plasma would circulate. Many experiments have been carried out in these Tokamaks all over the world, the largest currently being built in France, known as ITER (International Thermonuclear Experimental Reactor) [10,11] ITER is basically a powerful version of the Tokamak reactor which can sustain plasma for more than an hour, enough to power 50,000 households [12]. The truth is we just have not had the technology (mainly strong enough magnets and big enough reactors) to accomplish a 'breakeven' reaction where more power is extracted than that put in. ITER, however, is the largest, most expensive and most technologically advanced scientific experiment in the history of mankind. In the ITER, plasma-material interactions (PMI) can reduce the availability of a fusion reactor through the shortened lifetime of wall components and through limitations originating from safety regulations [10,13] These issues need urgently to be addressed, both in experiments and by modelling, to improve the predictions and to optimize the solutions for ITER and beyond. Plasma facing materials (PFMs), which act as the protective armor of fusion reactors and directly face the huge energy from fusion reactions, becomes one of the main problems that limit the practical application of fusion reactions [11]. Tungsten (W) and its alloys are considered to be the most promising PFM candidates as the armor material in divertor components due to its high melting point, high

strength at elevated temperatures, high elastic modulus, low thermal expansion, high thermal conductivity, high sputtering threshold, low hydrogen isotope retention, high resistance to neutron damage and low activation compared to other fusion relevant materials [14–16] However, the extremely harsh operational environment in the fusion reactor would inevitably result in serious performance degradation of PFMs. Under helium ion irradiation, the microstructure of tungsten-based materials is obviously changed and causes the brittleness of materials. Under the thermal shock loads, the W-based materials experience severe plastic deformation and crack growth. Therefore, improving the resistance of helium ion irradiation and thermal shock is of vital importance for engineering application [14,16,17].

In order to overcome the severe problems of W-based materials which are hard to produce due to its high melting point, researchers investigated grain refinement, second phase addition and deformation [18]. The most valid technique proposed to overcome these difficulties is the method called activated sintering. Activated sintering is the process of improving sinterability as a result of small additives to the powder composition or various changes made in the sintering atmosphere. In order to achieve activated sintering, the metal with a low melting temperature (various transition metals such as Pd, Pt, Ni, Cu, Co and Fe) must be dissolved in the metal with a high melting temperature. In this way, the sintering path is shortened and the process is facilitated. In addition, various carbides and nitrides such as TiC, ZrC, HfC, TiN, various oxides such as La_2O_3, Y_2O_3, HfO_2, Sm_2O_3, ThO_2 and various borides such as TiB_2, HfB_2, ZrB_2, CrB_2 were incorporated into W matrix to form composites. It has been revealed that composites which are reinforced with oxide, carbide, nitride, boride phases offer better and superior mechanical properties. Moreover, oxide, boride or carbide reinforced and activated sintered W matrix composites such as W-Cu-CeO_2, W-Ni-TiC-Y_2O_3, W-Cu-Ni-Y_2O_3, W-Ni-La_2O_3, W-Ni-TiB_2, W-Ni-TiB_2-La_2O_3, etc. exhibit enhanced microstructural and mechanical properties.

In this study, rare-earth borides were produced with mechanochemical synthesis. Then, synthesized rare-earth borides were added into W1Ni matrix with 6 h mechanical alloying. Also, two different methods were used for consolidation of powders. One of these methods was pressureless sintering at 1400 °C for 1 h. Another of them was spark plasma sintering at 1410 °C for 1 min. Then, characterization studies

were applied on the samples such as XRD, SEM/EDS, density, wear resistance, hardness and He^+ irradiation tests.

2. LITERATURE REVIEW

2.1 Properties of Particulate Reinforced W-Based Composites

In order to improve the physical and mechanical properties of tungsten (W), dispersion and precipitation hardened composites have been developed. It is possible to obtain tungsten composites with excellent properties by combining the properties of W with the properties of reinforcement elements. An example of the first application made in this direction is W with potassium additive, which has been made for the filaments in lamps, which has gained excellent creep strength by making a kind of dispersion strengthening [19]. Tungsten and its alloys are attractive candidate materials for various elevated temperature structural applications due to their excellent properties such as high melting point, high modulus, high resistance [19,20]. Since W-based materials are hard to produce due to its high melting point, researchers investigated grain refinement, second phase addition and deformation treatments. Some properties of W were shown in Table 2.1.

Table 2.1 : Properties of tungsten.

Properties of W	**Values**
Density	19.3 g/cm^3
Melting point	3410 °C
Thermal conductivity	175 W/m.K
Hardness	3.5 GPa
Thermal expansion coefficient	4.6×10^{-6} °C^{-1}
Young's modulus	3.27×10^5 N/mm^2

Tungsten and its alloys are considered to be the most promising plasma facing material (PFM) candidate as the armor material in divertor components due to its high melting point, high strength at elevated temperatures, high elastic modulus, low thermal expansion, high thermal conductivity, high sputtering threshold, low hydrogen isotope retention, high resistance to neutron damage and low activation compared to other

fusion relevant materials [11,21] However, the extremely harsh operational environment in the fusion reactor would inevitably result in serious performance degradation of PFMs. Under helium ion irradiation, the microstructure of W-based materials is obviously changed and causes the brittleness of materials. Under the thermal shock loads, the W-based materials experience severe plastic deformation and crack growth. Therefore, improving the resistance of helium ion irradiation and thermal shock is of vital importance for engineering application.

2.1.1 Mechanical properties of W-based composites

W-based composites have high hardness, high melting point, high thermal and electrical conductivity, high wear resistance and high strength [22]. In literature, some hardness values were given in Table 2.2. As results of hardness, W-1Ni-15TiC samples have 10.79 GPa, and this value is very high for W-based composites.

Table 2.2 : Properties of W-based composites.

W-Based Composites	Hardness (GPa)	References
W-5Ni-3Cu-0.4Y_2O_3	4.94	[23]
W-1Ni-2TiC	6.0	[24]
W-1Ni-15TiC	10.79	[25]
W-1Ni-2Al_2O_3	5.98	[26]
W-1Ni-1La_2O_3-2TiB_2	5.72	[27]
W–1Ni–1La_2O_3–2HfB_2	7.97	[28]
W-Cu-0.5CeO_2	1.87	[29]
W-1Ni-1Y_2O_3-2ZrC	7.16	[30]
W-1Ni-1Y_2O_3-2TiB_2	7.23	[31]
W-1Ni-0.5Y_2O_3-5TiB_2	8.54	[32]

Also, wear volume loss values of W-based composites are very low. These composites have good wear resistance properties [7-15].

2.1.2 Radiation behaviour of W-based composites

Tungsten which is being used as PFM in fusion devices that has divertor part, is brittle at low temperature [15]. Also, it is susceptible to embrittlement by irradiation and thermal overload [14]. So that, radiation resistance of W is increasing with adding some particulate borides, carbides and oxides. When W is exposured to irradition, its

structure is transformed to fuzz structure [33]. This fuzz structure is decreasing with adding particulate reinforcement.

2.2 Production Methods of Particulate Reinforced W-Based Composites

Tungsten (W) is one of the materials which is hard to produce. However, there are many different type of production methods. In order to improve W properties at radioactive and high temperature environment, some oxide, carbide and boride phases can add to W, and there are many studies about its activated sintering such as spark plasma sintering and pressureless sintering [4-18]. There are many production methods for W-based composites such as mechanical alloying and spark plasma sintering.

There are many studies about carbide reinforced W-based composites. W–2 wt% TiC powders were mechanically alloyed for 3, 6, 12 and 24 h. Then, W-1 wt% Ni was added for 20 min milled powders using the same MA conditions. Powders milled for different times were sintered with Anter Dilatometer at 1400 °C for 1 h. With increasing milling time, microhardness values were increased from 5.42 GPa to 6.00 GPa. Relative density was nearly around 94.2% [24]. Also, another study presented that W – x wt% TiC (x = 5, 10 and 15) powders were mechanically alloyed for 30 h. 1 wt% Ni was added for 1 h milled powders using the same MA conditions. Then, these powders were sintered with Anter Dilatometer at 1400 °C for 2 h and as-sintered samples were annealed at 1600 °C for 6 h. As-sintered W–1 wt% Ni (A), W–5 wt% TiC-1 wt% Ni (B), W–10 wt% TiC-1 wt% Ni (C) and W–15 wt% TiC-1 wt% Ni (D) samples had relative density values of 96.4%, 93.3%, 90.3% and 85.2%, respectively, and relative densities of annealing samples were measured as 99.8±0.1%, 98.1±0.4%, 93.1±0.9% and 91.7±0.8%, respectively. Relative densities of both as-sintered and heat treated samples are decreased with increasing TiC content. Whereas the respective microhardness values of the as-sintered A, B, C and D samples were 5.11±0.18, 7.14±0.51, 9.65±0.95 and 10.79±1.51 GPa and those for the heat treated samples were 4.62±0.11, 5.49±0.17, 7.22±0.39 and 8.1±0.47 GPa. After heat treatment, the microhardness values of the as-sintered samples decreased. As showing in article, the wear resistance values of the sintered samples (A, B, C, D) containing different TiC amounts, which wear resistance increased with increasing TiC content. A wear amount for the as-sintered A (that is no containing TiC), B, C and D samples were measured as 12.56±1.23, 6.70±0.07, 1.13±0.15 and 0.69±0.33 $mm^3N^{-1}m^{-1}$, respectively. As a

result, increasing TiC content improved the mechanical properties of W–TiC composites [25].

Oxide form can be added into W matrix. In another study, W-1 wt% Ni and W-1 wt% Ni-x wt% Al_2O_3 (x = 0.5, 1, 1.5 and 2) were mechanically alloyed for 18 h. Producing powders were sintered with Linn furnace at 1400 °C for 1 h. After this process, microhardness of W increased with adding Ni from 2.81±0.34 GPa to 4.07±0.16 GPa. When the amount of Al_2O_3 increased, microhardness of composite materials increased. The highest hardness value was 5.98±0.31 GPa for the sintered W-1 wt% Ni-2 wt% Al_2O_3 sample. Also, relative density of composite materials decreased with increasing amount of Al_2O_3. The relative density values of the samples were changing between 97.81% and 99.26% [26]. This article showed that W- 5 wt%. Ni- 3 wt%. Cu- x wt%. Y_2O_3 (x = 0, 0.2. 0.4, and 0.6) were mechanically alloyed by a high energy planetary ball mill for 25 h. Then, obtaining powders were sintered two methods which are conventional sintering at 1400 °C for 30 min and spark plasma sintering at 1100 °C for 4 min. As results, wear volume loss of samples was decreasing and microhardness of samples were increasing with increasing amount of reinforcement in the both of methods. SPS results were better then conventional sintering. As results, W-Ni-Cu-0.6 wt% Y_2O_3 SPS sample had the highest microhardness (504 HV), relative density (96.90%) and the lowest wear volume loss and wear rate [23]. Another study presented that W and CeO_2 powders were placed in an aqueous solution with a specified ratio of nitric acid (60–80 mL/L) and hydrogen peroxide (30–40 mL/L), respectively. A supersonic wave (40 kHz, 100 W) was applied for 30 min as pretreatment before electroless plating to produce a surface with catalytic activity. Various Cu–CeO_2 powders that depended on CeO_2 concentrations (0, 0.25, 0.5, 1 and 2 wt%) were added into the W–Cu composite powders by blending. Liquid phase sintering was applied to green bodies at 1300 °C for 1 h. When amount of CeO_2 was increased, relative densities of samples were decreased. The best electric conductivity was observed for W-Cu-0.25 wt% CeO_2 as 69.41% IACS. Then, electric conductivity decreased. Addition of CeO_2 to 1 wt% and 2 wt% slightly reduced the microhardness and bending strength resulting from CeO_2 agglomerations. W-Cu-0.5 wt% CeO_2 showed good mechanical properties. Microhardness and bending strength of this composite material were measured 190.23 HV and 1102.7 MPa, respectively [29]. In another study, W-10 wt% Ni-1 wt% x (x= Y_2O_3, Al_2O_3 and La_2O_3) were mechanically alloyed as 1, 5 and

10 h with high energy planetary ball milling. Powders that mechanically alloyed for 10 h were sintered at 1400 and 1500 °C for 2 h in the furnace. When sintering temperature increased, amount of oxide phases increased. All the relative density and microhardness results were increasing at 1500 °C. The highest relative density (90%), compressive strength (2.25 GPa) and microhardness (5.53 GPa) results were obtained in W-10 wt% Ni-1 wt% Y_2O_3 [34]. In another work, the preparation of W-0.25 wt% $(Y_{0.9}La_{0.1})_2O_3$ composite powder by improved wet chemical method is divided into two stages, namely the preparation and reduction of the precursor. First, the 0.272 g of yttrium nitrate hexahydrate ($Y(NO_3)_3$ $6H_2O$, 0.034 g of lanthanum nitrate hexahydrate (La $(NO_3)_3$ $6H_2O$) and 1 ml of triethanolamine oleate ($C_{24}H_{49}NO_5$) are dissolved in 400 ml of deionized water and stirred to obtain the mixed solution. The 50 g of ammonium metatungstate and 0.636 g of precipitant oxalic acid ($C_2H_2O_4$ $2H_2O$) is added to the mixed solution. Another study presented that the W-$(Y_{0.9}La_{0.1})_2O_3$ precursor is obtained. Then, nine W-$(Y_{0.9}La_{0.1})_2O_3$ composite materials were sintered at different temperatures (1550, 1600 and 1650 °C) and pressures (50, 75 and 100 MPa). Relative densities of samples were increasing with increasing sintering temperature and pressure 75 MPa and 1600 °C sintered sample showed the most excellent mictostructure. It has nearly 500 HV. In addition, the fine-dispersed distribution of $(Y_{0.9}La_{0.1})_2O_3$ particles in the tungsten-based composites can effectively improve the resistance of helium ion irradiation and laser thermal shock [35].

Boride, carbide and oxide form materials can be added into W-based composites. Another study showed that W and 1 wt% Ni were mechanically alloyed for 6 h [27]. Then, 2 wt% TiB_2 and x wt% La_2O_3 (x= 0.5, 1) were added into W-1 wt% Ni for 6 and 12 h. After that, obtaining powders were sintered at 1400 ^{0}C for 1 h in the Linn furnace. As microhardness results, W-1 wt% Ni had 4.08±0.28 GPa. With adding reinforcement, microhardness increased to 5.72±0.19 GPa for 12 h milled W-1 wt% Ni-1 wt% La_2O_3-2 wt% TiB_2 composite materials. Also, highest relative density was obtained with this composite as 98.38%. The lowest wear rate was observed for 12 h milled W-1 wt% Ni-1 wt% La_2O_3-2 wt% TiB_2 composite materials as 2.11±0.28 $(mm^3N^{-1}m^{-1})\times10^{-9}$ [27]. In different study, W-1 wt% Ni was mechanically alloyed (MA) as 6 h, and was reinforced with 0.5 wt% Y_2O_3 and x wt% TiB_2 (x = 1, 2, 3, 4 and 5) for 12 h. Obtained powders were sintered in a Linn furnace at 1400 °C for 1 h. Microhardness and relative density of W – 1 wt% Ni composite was measured as

4.54±0.1 GPa and 97.03 %. Also, highest microhardness value and relative density were obtained with W-1 wt% Ni-0.5 wt% Y_2O_3-5 wt% TiB_2 as 8.54±0.25 GPa and 95.67%, respectively [32]. In another study, different boride and oxide forms added into W–1 wt% Ni matrix. Powders were mechanically alloyed for 12 h. Compositions of W–1 wt% Ni, W–1 wt% Ni–1 wt% x, and W–1 wt% Ni–1 wt% x–2 wt% y (x = La_2O_3 and Y_2O_3; y = CrB_2, HfB_2, and ZrB_2) were produced. Then, these powders were sintered at 1400 °C for 1 h in the Linn furnace. Also, higher microhardness value and lower volume loss of results were obtained with adding La_2O_3 as Y_2O_3. Also, addition of HfB_2 gave the highest microhardness value (7.97±0.50 GPa) and lowest volume loss (153.88 μm^3) values [28]. In a different study, it was reported that W and 1 wt% Ni were mechanically alloyed for 6 h. Also, 2 wt% ZrC and 1 wt% Y_2O_3 were added to W–1 wt% Ni as 6 h by mechanical alloying [30]. Different milling types that are room temperature and cryogenic condition (S1, S2 and S3) were examined. As-blended W-1 wt% Ni-1 wt% Y_2O_3-2 wt% ZrC powder milled for 12 h at room temperature is referred to as S1, cryomilled for 10 min in the presence of externally circulated liquid nitrogen is referred to as S2 and sequentially milled at room temperature for 12 h and cryogenic condition for 10 min is referred to as S3. Also, producing powders were sintered at 1400 °C for 1 h in the Linn furnace. Sequentially milled (S3) and sintered sample exhibited the highest microhardness (7.16±0.59 GPa), the highest relative density (95.09 %) and the lowest wear volume loss (66.0 μm^3) value [30]. Another article showed that W and 1 wt% Ni were mechanically alloyed for 6 h. Also, 1 wt% Y_2O_3 and 2 wt% TiB_2 were added to W–1 wt% Ni as 6 h by mechanical alloying. Different milling types that are room temperature and cryogenic condition (S1, S2 and S3) were examined [31]. As-blended W-1 wt% Ni-1 wt% Y_2O_3-2 wt% TiB_2 powder milled for 12 h at room temperature is referred to as S1, cryomilled for 10 min in the presence of externally circulated liquid nitrogen is referred to as S2 and sequentially milled at room temperature for 12 h and cryogenic condition for 10 min is referred to as S3. Also, producing powders were sintered at 1400 °C for 1 h in the Linn furnace. Sequentially milled (S3) and sintered sample exhibited the highest microhardness (7.23 GPa), the highest relative density (95.77%). Also, yielded a nanohardness and elastic modulus for this sample were measured as 8.9 and 373.7 GPa, respectively [31]. The appropriate amounts of ammonium tungstate ($(NH_4)_6H_2W_{12}O$ 40% XH_2O), yttrium nitrate ($Y(NO_3)$ 3% $6H_2O$), and TiC particles were mixed in deionized water under ultrasound conditions [36]. A certain amount of oxalic acid (C_2H_2O 4% $2H_2O$)

as a precipitating agent during precursor preparation was added to the mixed liquid. The precursor powder was obtained by drying the solution, which was reduced in a hydrogen atmosphere to obtain W-1 vol% TiC-1 vol% Y_2O_3 (W-TiC-Y_2O_3) composite powder. Then, obtained powders were sintered at different sintering temperatures (1100, 1200, 1350, 1600 and 1800 °C) for 5 min. Density and microhardness value of samples increased with increasing sintering temperatures. Also, the highest microhardness value was measured as 363.64 HV [36]. Another study showed that irradiation test was applied to previous study sample. After they passed through the particles, cracks propagated through the interface between the tungsten and Y_2O_3 for W-Y_2O_3. Moreover, the crack width becomes narrow and the direction of crack propagation was changed under the effect of particles. Melting of W-Y_2O_3 was more evident than that of pure tungsten, due to the doping of a low-melting-point material. Although ablation was observed in pure tungsten, it was not in W-Y_2O_3 [37]**.** In another study reported that examining of different mechanical properties in W-1 wt% Ni-2 wt% WB-x wt% La_2O_3 (x=0.5 and 1) composite materials. After La_2O_3 powders were milled for 6 h, they were added to W-1 wt% Ni-2 wt% WB that were milled for 6 h. Totally after 18 h, obtaining powders were sintered at 1400 °C for 1 h in the Linn furnace. As results, after adding La_2O_3, while volume loss was decreasing (up 292.5 to 115.8 μm^3), relative density was increasing (up 91.70% to 96.97%). Finally, microhardness of W-1 wt% Ni-2 wt% WB-0.5 wt% La_2O_3 and 1 wt% La_2O_3 decreased to 5.35 and 6.02 GPa from 6.05 GPa, respectively [38]. This study showed that the powders of composite were fabricated from 87.5 wt% pure W powder, 5 wt% Cu powder, 3 wt% Ni powder, 0.5 wt% Y_2O_3 powder, 0.5–3.5 wt% zirconium powder, 0.5–3.5 wt% titanium powder, respectively. These powders were milled for 36 h with 500 rpm. 3.5 wt% Ti and 0.5 wt% Zr; 0.5 wt% Ti and 3.5 wt% Zr composite materials were named as T and Z, respectively. These powders were spark plasma sintered at 1050 ºC for 2 min. Relative densities of these samples were exceeded to 100%. While ths highest microhardness (911.9 HV) was obtaining with T sample, the best electirical conductivity (19.9 mS/m) was obatined with Z sample [39].

Ta, V, Cr and Ti can be added into W for improving properties of W-based composites. In study, $W_{90}(TaVCrTi)_{10}$, $W_{80}(TaVCrTi)_{20}$, $W_{70}(TaVCrTi)_{30}$, and $W_{60}(TaVCrTi)_{40}$ powders were mechanically alloyed for 25 h with 400 rpm milling speed. Then, producing powders were sintered at 1400 °C for 5 min [40]. When the radiation test

was applied, the damage of the W70-M30 alloy was the lowest. $W_{70}(TaVCrTi)_{30}$ alloy showed the best surface stability among the five materials under the He^- irradiation conditions thanks to self healing mechanism. Also, ultra fine grain structure played more important for this. Finally, the samples were heated by the plasma column during the irradiation test. The temperature of the irradiated sample increased with the addition of Ta, V, Cr and Ti. Also, the thermal diffusivity decreased with an increase in the Ta, V, Cr, and Ti contents [40]. In another study, WV_5Ta_5 powders were produced with 400 rpm and 25 h milling process. Then, obtaining powders were sintered 1400 °C for 5 min. Relative density of composite material increased to 98.6% from 88%. Also, microhardness, tensile and compressive strength of material was measured as 7.97 GPa, 453 MPa and 3656 MPa, respectively. The higher He^- irradiation resistance of WV_5Ta_5 can mainly attribute to the ultrafine grains, while it also has the relationship with the higher compressive and tensile strength of WV_5Ta_5 [33].

2.2.1 Mechanical alloying

Mechanical alloying (MA) is a powder metallurgy method in which a composite powder with a controlled, and fine structure can be produced in a high energy ball mill as a result of repeated re-welding, cold welding, and fracture. Solid state alloying, which is not possible with conventional grinding processes, is performed by mechanical alloying in attritor, planetary ball mill, some vibratory mills and laboratory scale Spex mills providing high energy grinding environment [41,42]. With a history of nearly 40 years, MA is a low-temperature alloy synthesis method in which powders are subjected to continuous fracture and cold welding and re-fracture in normal and/or inert environments to produce very fine microstructures. Mechanical alloying is the process of turning the raw material into desired microstructure and grain size as a result of a mechanical effect in the presence of grinding medium (inert or air) and ball with the help of a milling device [43]. As schematically, mechanical alloying was given in Figure 2.1.

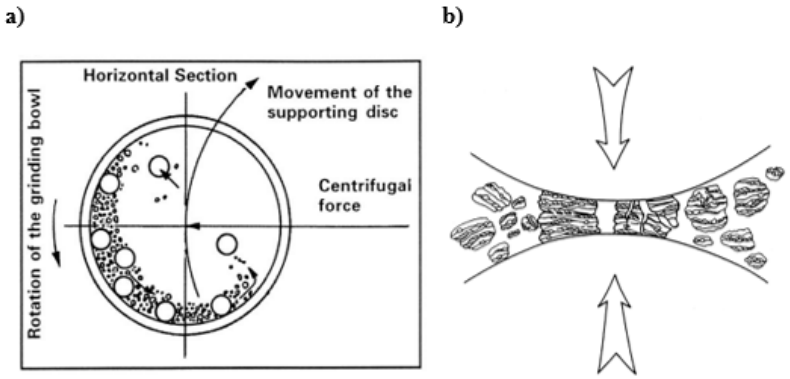

Figure 2.1 : a) Schematic depicting the ball motion inside the ball mill and b) Schematic of ball-powder collision [43].

The final stage regular structure was obtained, and a balance was reached between the welding level, which causes the increase in the particle size, and the fracture mechanisms, which have the effect of reducing the particle size. As a result, small particles and large particles mix with each other, and form a homogenized structure in dimension [43]. The structure obtained after this step is the same as the starting composition. The lamellar structure formed in the first stages is no longer visible. Further alloying after this stage will not affect the more homogeneous dispersion of the dispersoids. The particle size distribution range is narrowed. Large particles were reduced to average size, and small-sized particles agglomerated to this level. Mechanical alloying is a very efficient technique due to its technical advantages. One of its most important advantages is the ability to synthesize new alloys or to alloy elements that cannot be alloyed with normal methods. The reason for this is that MA is a completely solid state process, and the limitations specified in the phase diagrams do not apply to the MA process [43]. There are many process parameters such as milling temperature, ball-to-powder weight ratio, process control agent, ball diameter, etc [43]. Effect of milling time to particle size was shown in Figure 2.2.

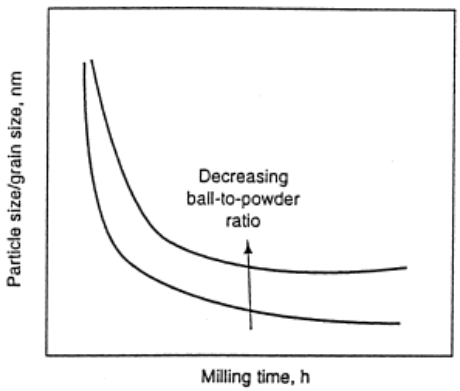

Figure 2.2 : Refinement of grain and particle sizes with milling time [43].

2.2.2 Activated sintering

The manufacturing process is difficult due to the high melting point and low ductility of tungsten. Even when powder metallurgy technology is used, sintering of tungsten requires temperatures of 2400–2800 ºC [44]. However, the addition of some transition metals such as Pd, Pt, Ni, Co and Fe in very small amounts causes a significant decrease in the sintering temperature of W [44,45]. The decrease in the sintering temperature is due to the decrease in the activation energy between the W particles. For example, the volumetric diffusion activation energy of W is 135 kcal/mol. This value is 68 kcal/mol when Ni is added to activate W [45].

In activated sintering, very small amounts of additives must be added to increase the sintering kinetics. It is thought that the additive material added as an activator may facilitate sintering by removing the oxide layer on the metal surface or by making the metal atoms diffuse faster. Materials with high melting temperatures require very high sintering temperatures in order to achieve sufficient diffusion rate during sintering. However, at these temperatures, phases with low melting points will naturally have very high diffusion rates. Based on this, activated sintering can be defined as the ease of sintering that occurs due to the dissolution of a sample with a high melting temperature in a sample with a low melting temperature [46]. The most commonly applied refractory materials of activated sintering processes are: Mo, W, Cr, Rh, Ta [47]. In order to better understand the mechanism of activated sintering, it is necessary to examine the studies conducted to understand this issue. In a study carried out by Hayden and Brophy, the mechanism of activated sintering were interpreted in three main stages [45]. First, after the supporting phase formed by the additive material begins to form on the surface of the W particle, W begins to dissolve where the particles contact. In the second part, necking is provided by the diffusion of W atoms at the contact points formed along the interface formed by the supporting phase and the W particle. Finally, the distance between neighboring particles decreases, resulting in intense shrinkage [45,48]. Brophy et al. There is a schematic representation of nickel (Ni) added W powders [45], it was shown in Figure 2.3.

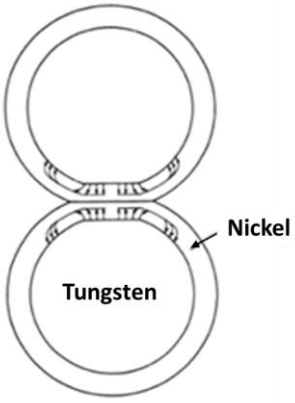

Figure 2.3 : Schematic representation of the sintering of nickel-doped tungsten powders [45].

There is also a publication by Toth et al. on the activation sintering mechanism [49]. They stated that the activator-tungrum interface was formed by the additive material forming an activator layer, and tungsten dissolved along this surface. This allows the activation layer to move towards the contact point between neighboring particles, and form the sintering structure called as neck, as seen in Figure 2.4 [49,50].

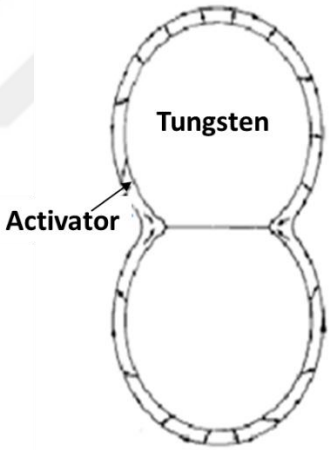

Figure 2.4 : Schematic representation of the activation sintering of W [49].

2.3 Usage Area of W-Based Composites

Tungsten is generally using harsh conditions such as high temperature, high neutron and flux [51]. Also, fusion devices have very hard conditions. However, W is very good oppurtunity for this conditions thanks to high melting point, high sputtering threshold energy, low tritium retention and low neutron activation [51]. Divertor part of Tokamak was shown in Figure 2.5.

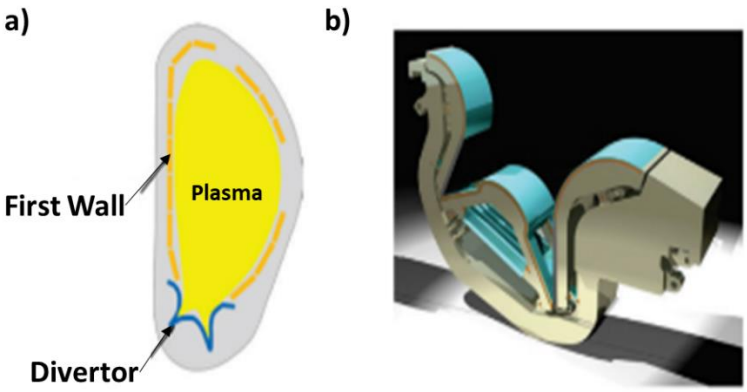

Figure 2.5 : a) Schematic of cross-section of Tokamak and b) solid model illustration of divertor [51].

Also, W-based composites are using to need high wear resistance, high hardness and high temperature [52].

2.4 General Information about Rare-Earth Borides

Metal borides are important and unique materials utilized at high-temperature applications. Rare-earth (RE) borides are a family of high-temperature materials with extremely fascinating chemical and structural properties [53]. Thanks to particular strong covalent bonding of boron, great stability and high hardness in extreme conditions are observed for these boride materials. As a new development, exciting magnetic and electronic physical properties have been found in the newly discovered rare-earth boron compounds [54].

2.5 Properties of Cerium Hexaboride

Cerium hexaboride (CeB_6), a refractory ceramic material, has attracted significant interest in recent years among transition metal borides and rare-earth metal borides. It crystallizes in a CsCl-type structure with a space group of Pm3m symmetry, where the cerium ions occupy the Cs sites, and octahedral B_6 molecules are located at the Cl sites [55]. CeB_6 exhibits low density (~4.79 g/cm^3), high melting temperature (~2550 °C), high hardness (~2530 HV), high chemical and thermal stability, low electrical resistivity (~30 μΩ·cm), high thermal conductivity (~34 W/m·K), low electronic work function (~2.5 eV), low coefficient of thermal expansion (~7.4×10^{-6} °C $^{-1}$) and high neutron absorbability [55–62]. These properties were shown in Table 2.3.

Table 2.3 : Properties of CeB_6.

Properties of CeB_6	**Values**
Density	4.79 g/cm^3
Melting point	2330 °C
Thermal conductivity	34 W/m.K
Hardness	24.81 GPa
Thermal expansion coefficient	7.4×10^{-6} °C^{-1}
Electrical resistivity	30 μΩ·cm
Electronic work function	2.5 eV

Among the known hexaborides, CeB_6 has the interesting physical property of dense Kondo behaviour [38-46]. The combination of these properties enables CeB_6 to be used in special applications, such as materials for wave absorption, cathode emission and nuclear fields [64]. The known hexaborides, CeB_6 has the interesting physical property of dense Kondo behaviour [55,63]. The combination of these properties enables CeB_6 to be used in special applications, such as materials for wave absorption, cathode emission and nuclear fields [64]. CeB_6 is considered as an excellent field electron emitter source for various devices with its low work function [56,59]. It is also used in high energy optical systems and in sensors for high-resolution detectors due to its long service life time and low volatility at high temperatures [2]. CeB_6 has also attracted considerable attention because it shows several interesting phases in the presence of magnetic field and temperature such as antiferro-quadrupolar ordered phase and antiferromagnetic ordered phase [46,48].

As phase diagram which is shown in Figure **2.6**, CeB_6, CeB_4 are the main phases between cerium and boron. However, CeB_6 is the most stable phase in the diagram [66].

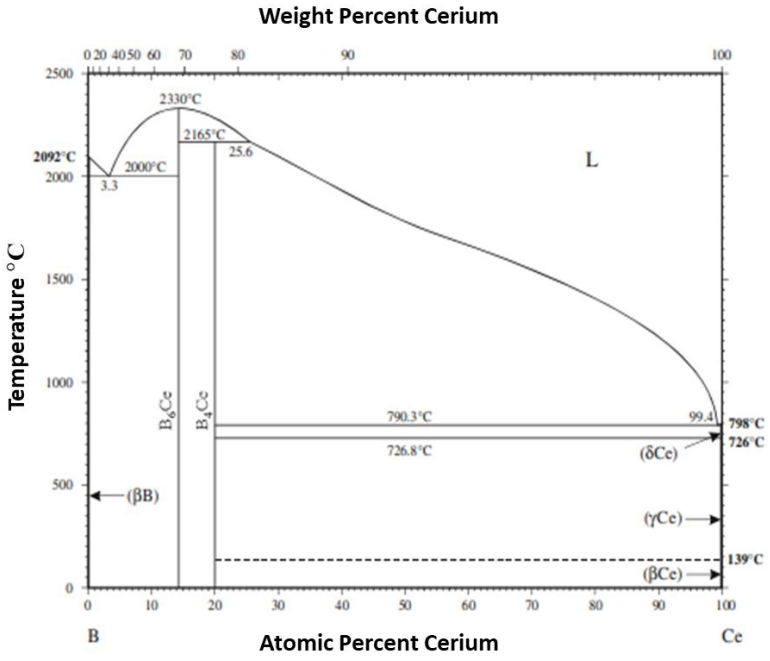

Figure 2.6 : Phase diagram of Ce-B system [66].

2.6 Production Methods of Cerium Hexaboride

Traditionally, CeB_6 is synthesized by high temperature reaction processes such as direct solid-phase reaction of cerium or its oxides with elemental boron and carbothermal synthesis using carbon and boron carbide [59,63,64,67,68]. However, the disadvantages of these methods, such as high content of carbon or high processing temperatures, limit the possibility of preparing CeB_6 powders with high purity and fine particle sizes [64]. In the literature, CeB_6 was produced by borothermal reduction of CeO_2 with a boron source, under formation of volatile boron suboxides at 1200–1800 °C in vacuum [68]. Recently, CeB_6 powders were prepared via different synthesis techniques, such as self-propagating high temperature synthesis (SHS - also known as combustion synthesis), mechanochemical, electrochemical and gas phase synthesis methods. Accordingly, nanoscale CeB_6 powders were prepared by SHS using CeO_2, B_2O_3 and Mg as raw materials [64,69]. After leaching of the SHS products, CeB_6 powders were obtained with purity higher than 99% and an average particle size of 30–70 nm [64]. Furthermore, CeB_6 nanowires with a diameter of around 20–100 nm were synthesized by self-catalyst metal-gas reaction method at 1125 °C on a Si substrate using Ce powders and BCl_3 / H_2 / Ar gas mixtures [59]. Furthermore, several investigations relate the synthesis of CeB_6 films or coatings and their field emission properties [63]. Additionally, electrochemical synthesis (at 900 °C) was performed to

obtain CeB_6 crystals by using the molten salt technique from the electrolyte consisting of and LiF / B_2O_3 / $CeCl_3$ as raw materials [62]. In the present study, polycrystalline bulk CeB_6 ceramics were produced by using SPS with CeO_2 and coarse, nano B powders. In-situ synthesis and densification of CeB_6 ceramics were conducted applying a two-step heating schedule and temperature of process was chosen as 1000 °C and 1950 °C with using FactSage thermochemical software. CeB_6 that has coarse boron in 8 wt% lack ratio showed the highest CeB_6 content (98.4 vol%), high hardness (16.0 GPa), high fracture toughness (2.8 MPa $m^{1/2}$) and low electrical resistivity (1.58×10 Ωm). So that, polycrystalline bulk CeB_6 was synthesized at 1950 °C for 15 min under 15 kN with SPS technique from CeO_2-coarse B powder mixture in 8 wt% lack B ratio. This sample has a good potential to be used as electron emitters such as in electron microscopes. [70].

2.7 Properties of Neodymium Hexaboride

Among rare-earth (RE) borides, rare-earth hexaborides (REB_6) have attracted more attention thanks to their extreme characteristics like high hardness, melting point, chemical stability, magnetic properties and superconductivity [71]. REB_6 are of considered interest due to their usage as field-emission sources in various devices. They are generally used in high-energy optical systems, as sensors for high-resolution detectors, and as electrical coatings for resistors because of their low work function, small optical size, high brightness, low volatility at high temperatures, their long service life and the mono energetic character of their electrons [55,72].

Neodymium hexaboride (NdB_6) is an important member of rare-earth hexaborides and has very interesting magnetic and mechanical properties. According to the Nd-B binary phase diagram, there are four stable phases that their stoichiometries are Nd_2B_5, NdB_4, NdB_6 and NdB_{66}. When phase diagram is considered, NdB_6 was observed as the most stable phase as shown in Figure 2.7 [73].

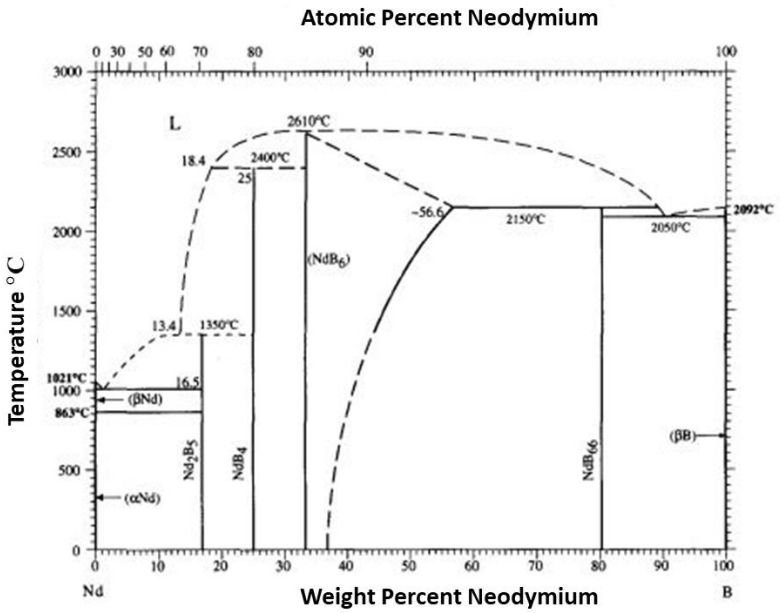

Figure 2.7 : Phase diagram of Nd-B system [73].

NdB_6 has a cubic structure with a space group of Pm-3m, in which Nd atoms centered by a boron atom octahedron [74]. NdB_6 has low density (4.95 g/cm^3), high melting point (2610 °C), good thermal conductivity (47 W/m.K), high hardness (24.9 GPa) and good thermal expansion coefficient (7.3×10^{-6} °C^{-1}) as given in the Table 2.4 [75]. NdB_6 orders in an A-type collinear antiferromagnetic structure below $T_N \approx 8$ K. [76].

Table 2.4 : Properties of NdB_6.

Properties of NdB_6	**Values**
Density	4,95 g/cm^3
Melting point	2610 °C
Thermal conductivity	47 W/m.K
Hardness	24.9 GPa
Thermal expansion coefficient	7.3×10^{-6} °C^{-1}

2.8 Production Methods of Neodymium Hexaboride

Neodymium hexaboride powders can be fabricated by using very different synthesis methods. Recently, NdB_6 have been synthesized with carbothermal synthesis method using carbon and boron carbide, combustion synthesis method, mechanochemical synthesis, flux-controlled self-catalyzed method and a facile catalysis-free method [74, 77-81]. In literature, NdB_6 powders were produced from Nd_2O_3–B_4C system under the

conditions of 10^{-2} Pa vacuum and 4 h holding time at temperature above 1500 °C [74]. Moreover, ultra-fine NdB_6 powders were fabricated via combustion synthesis method starting from B_2O_3, Nd_2O_3 and Mg powder mixtures [77]. Pure NdB_6 nanocrystals were synthesized by mechanochemical alloying of Nd, B_2O_3 and Mg powders at room temperature with milling rate of 300 rpm for different durations up to 30 h and by subsequent CH_3COOH leaching [78]. NdB_6 submicroawls were produced with a simple flux-controlled self-catalyzed method by using BCl_3 gas and Nd powders as starting materials at 1000 °C [79]. Also, NdB_6 nanowires synthesized via a facile self-catalysis growth method using Nd powders and BCl_3/H_2 gas mixture [80]. Amorphous boron with purity of 99.99% was mixed with rare-earth oxide Nd_2O_3 with a purity of 99.9%. Also, these powders were weighed in the ratio B:Nd = 5:1, then was placed in a high pressure assembler [81].

2.9 Properties and Production Methods of Erbium Tetraboride

Rare-earth tetraborides (RB_4) have a tetragonal crystal structure with a space group D54h-P4/mbm. RB_4 compounds behave as good metals and order antiferromagnetically. However, only PrB_4 orders ferromagnetically [80,82]. Melting point was calculated as 2360 °C [83]. In the Er-B phase diagram, ErB_2, ErB_4, ErB_{12}, and ErB_{65} are possibility phases that can occurs. Also, the most stable phase is ErB_4 as phase diagram of Er-B that is shown in the Figure 2.8 [84].

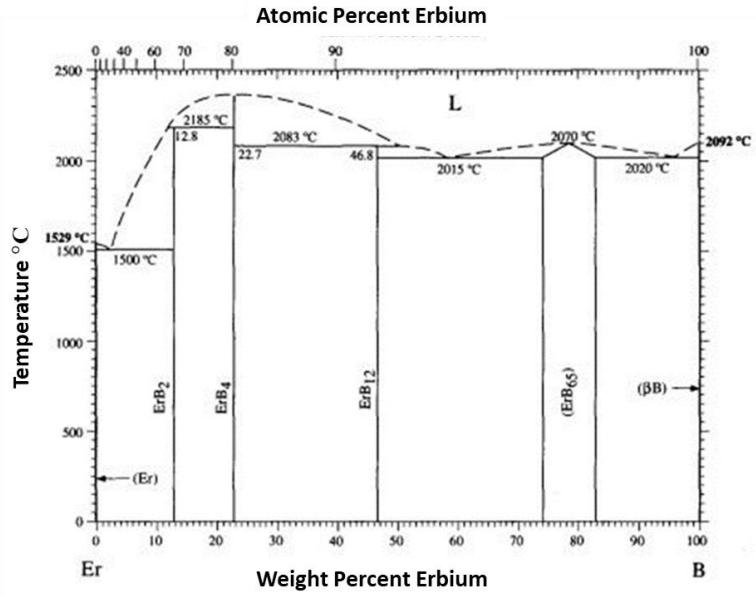

Figure 2.8 : Phase diagram of Er-B system [84].

Production of erbium tetraboride (ErB_4) powders has very unique process. In literature, there is not too much examples about production method. In one study, the polycrystal of ErB_4 was produced with the borothermal reduction of metal from its oxide in a vacuum ($5\ 10^{-5}$ Torr, 1750 ^oC and 2.5 h) [85].

Apart from the reported literature, in this thesis, nanostructured Ce, Nd and Er hexa/tetraborides powders were produced by using mechanochemical synthesis route which is a simple and room temperature process enabling control of the product microstructure (phase, shape, size, etc.) and obtaining homogeneous materials [86,87]. There are very limited number of studies focused on the synthesis of these powders in the literature. In the reported studies, different raw materials such as elemental and oxide powders, boron, boron carbide, boron trichloride raw materials were used for the preparation of these borides. However, the formation of hexa or tetra borides by mechanochemical synthesis and leaching affected by different raw material amounts has not been investigated in detail yet. So, this thesis will fulfill this gap in the archival literature.

3. EXPERIMENTAL PROCEDURE

3.1 Raw Materials

CeO_2, Nd_2O_3, Er_2O_3, B_2O_3, Mg, W and Ni powders were used for this study. Properties of these powders were given in Table 3.1.

Table 3.1 : Properties of raw materials.

Samples	Producer	Purity	Particle size (µm)
CeO_2	ABCR	99.99%	9.5
Nd_2O_3	Alfa Aesar	99%	5.069
Er_2O_3	ABCR	99.99%	7.271
B_2O_3	ETI Mine	98%	385.994
Mg	Alfa Aesar	99.8%	107.619
W	China	99%	< 40
Ni	APS	99.9%	<7

XRD analysis was done to raw materials in 10-90º range with 2 º. As XRD results, CeO_2 (ICDD Card No: 00-034-0394, Bravais lattice: cubic, a = 0.541 nm), Nd_2O_3 (ICDD Card No: 01-075-2255, Bravais lattice: hexagonal, a = 0.383 nm and c = 0.599 nm), NdO_2 (ICDD Card No: 00-046-1074, Bravais lattice: cubic, a = 0.554 nm), Er_2O_3 (ICDD Card No: 00-008-0050, Bravais lattice: cubic, a = 1.055 nm), B_2O_3 (amorphous structure in the presence of absorbed water), W (ICDD Card No: 00-001-1204, Bravais lattice: cubic, a = 0.316 nm) and Ni (ICDD Card No: 00-004-1074, Bravais lattice: cubic, a = 0.352 nm) were given in Figure 3.1.

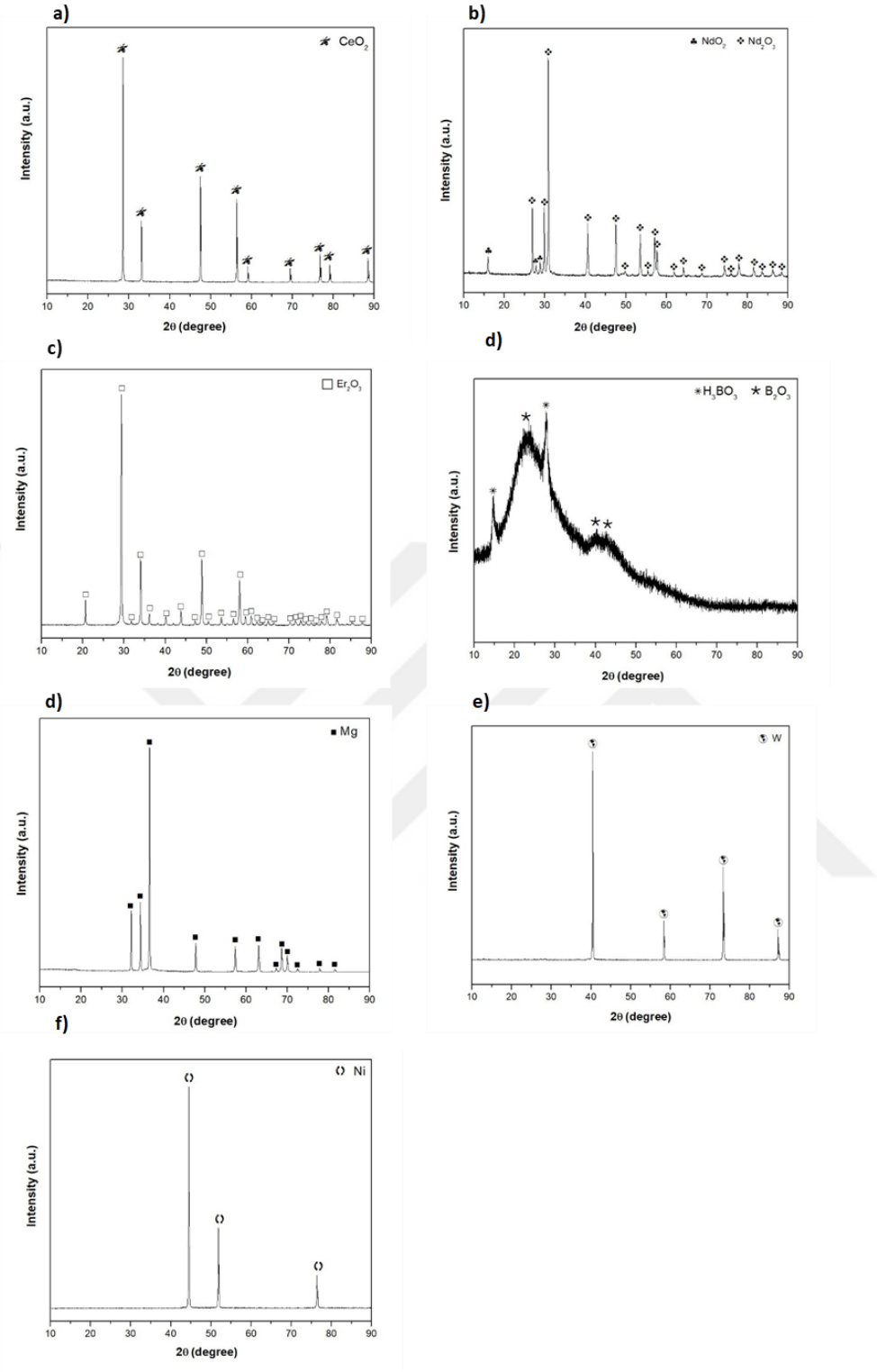

Figure 3.1 : XRD patterns for raw materials a) CeO_2, b) Nd_2O_3, c) Er_2O_3, d) B_2O_3, e) Mg, f) W and g) Ni.

3.2 Preparation, Mechanochemical Synthesis and Purification of Rare-Earth Boride Powders

CeO_2, B_2O_3 and Mg powders were used as the starting materials for producing of powders. Stoichiometry for the synthesis of CeB_6 from the CeO_2, B_2O_3 and Mg powders was given by the reduction reaction in Eq. (3.1). The stoichiometric amounts of the initial reactants CeO_2 : B_2O_3 : Mg were 1.593 : 1.933 : 2.474 g for powders as per Eq. (3.1).

$$CeO_2 + 3\,B_2O_3 + 11\,Mg \rightarrow CeB_6 + 11\,MgO \quad (3.1)$$

Nd_2O_3, B_2O_3 and Mg powders were used as the starting materials for producing of NdB_6 and NdB_4 powders. Stoichiometry for the synthesis of NdB_6 from the Nd_2O_3, B_2O_3 and Mg powders was given by the reduction reaction in Eq. (3.2). The stoichiometric amounts of the initial reactants Nd_2O_3 : B_2O_3 : Mg were 1.598 : 1.984 : 2.424 g for powders as per Eq. (3.2). Stoichiometry for the synthesis of NdB_4 and NdB_6 from the Nd_2O_3, B_2O_3 and Mg powders was given by the reduction reaction in Eq. (3.3). The stoichiometric amounts of the initial reactants Nd_2O_3 : B_2O_3 : Mg were 1.8 : 1.861 : 2.34 g for powders as per Eq. (3.3). Stoichiometry for the synthesis of NdB_4 from the Nd_2O_3, B_2O_3 and Mg powders was given by the reduction reaction in Eq. (3.4). The stoichiometric amounts of the initial reactants Nd_2O_3 : B_2O_3 : Mg were 2.0626 : 1.7071 : 2.2348 g for powders as per Eq. (3.4).

$$Nd_2O_3 + 6\,B_2O_3 + 21\,Mg \rightarrow 2\,NdB_6 + 21\,MgO \quad (3.2)$$

$$Nd_2O_3 + 5\,B_2O_3 + 18\,Mg \rightarrow NdB_6 + NdB_4 + 18\,MgO \quad (3.3)$$

$$Nd_2O_3 + 4\,B_2O_3 + 15\,Mg \rightarrow 2\,NdB_4 + 15\,MgO \quad (3.4)$$

Er_2O_3, B_2O_3 and Mg powders were used as the starting materials for mechanical milling. Stoichiometry for the synthesis of ErB_4 using Er_2O_3, B_2O_3 and Mg powders was given by the reduction reaction in Eq. (3.5). The stoichiometric amounts of the initial reactants Er_2O_3 : B_2O_3 : Mg were 2.242 : 1.632 : 2.136 g for powders as per Eq. (3.5).

$$Er_2O_3 + 4\,B_2O_3 + 15\,Mg \rightarrow 2\,ErB_4 + 15\,MgO \quad (3.5)$$

For weighing of powders, KERN PLJ precision balance device was used that is shown as Figure 3.2 was used.

Figure 3.2 : KERN PLJ precision balance.

The total powder batches of 6 g were weighted for powders. Then, as-blended powders were mixed in as shown in Figure 3.3. WAB T2C Turbula at room temperature for 2 h.

Figure 3.3 : WAB Shaker-Mixer Type T2C Turbula.

For the mechanochemical synthesis (MCS) reactions, shaked/mixed powders and hardened steel balls (6 mm diameter) were put in hardened steel (50 ml) vials shown in Figure 3.4a with a ball-to-powder weight ratio of 10:1. Thus, the total powder batches of 6 g were weighed under Ar atmosphere (Linde, 99.999% pure) in a MBraun LABstar glove box that is shown as Figure 3.4b.

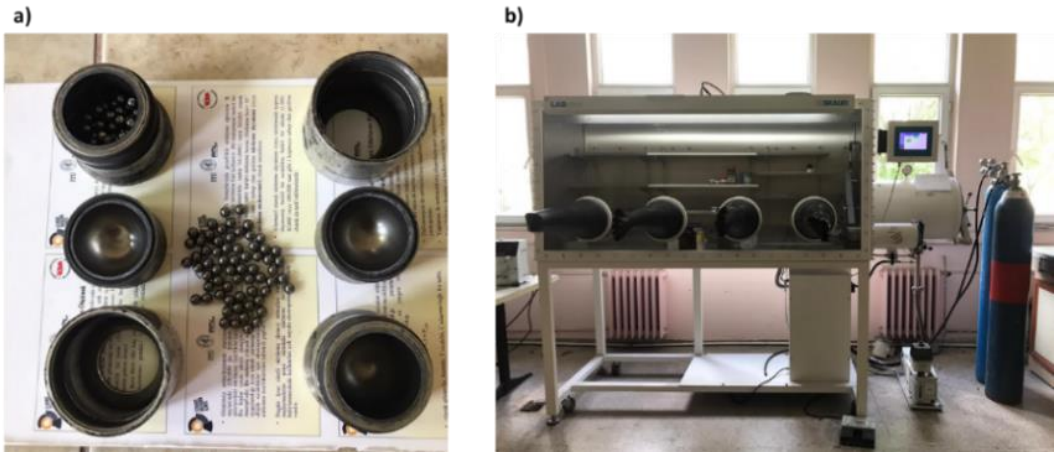

Figure 3.4 : a) Hardened steel vial and balls and b) Glove-box.

The boride powders were milled in a high energy Nano Multimix Mixer/Mill that is shown in Figure 3.5. The milling process for boride powders was carried out with 6 g powder batches for each vial. Milling speeds and milling durations were used as 1188 rpm (58 Hz), 920 rpm (45 Hz) and up to 8 h, respectively. Also, the vials were filled with ethanol and cleaned for 20 min after each milling batch.

Figure 3.5 : High-energy Nano Multimix Mixer/Mill.

After MCS, HCl acid (Merck, 37 %) leaching was applied in order to remove MgO by-product with 2, 4 and 6 M. The leaching treatment was conducted at 80 °C for 20 min with a solid-to-liquid ratio of 1 g/10 cm^3. The residue was then separated from the leaching solution with repeated centrifugation. Hettich Rotofix 32A that is shown in Figure 3.6 was used for repeated centrifugation at 4000 rpm for 20 min with decantation and rinsing steps.

Figure 3.6 : Hettich Rotofix 32A.

The residue was dried in GALLENKAMP Hotbox Oven that is shown in Figure 3.7 at 80 °C for 18 h in air. The residue was hereafter referred to as leached powders.

Figure 3.7 : GALLENKAMP Hotbox Oven.

3.3 Mechanical Alloying and Reinforcing of W1Ni Matrix

99 wt% W and 1 wt% Ni were mechanically alloyed for 6 h. WC vials and balls shown in Figure 3.8 were used with a ball-to-powder weight ratio of 10:1. Thus, the total powder batches of 15 g were weighed. After producing of W1Ni prealloy, laboratory synthesized 1, 2, 5 and 10 wt% of CeB_6, NdB_6 and ErB_4 boride powders were added into matrix.

Figure 3.8 : WC vials and balls.

The boride added W1Ni powders were milled in a high energy ball mill (Spex 8000D Mixer/Mill) which is shown in Figure 3.9. The milling process was conducted on the 15 g powder batches for each vial. Milling speed of 800 rpm (38 Hz) and milling durations of 6 h were carried out for the composite powders.

Figure 3.9 : Spex 8000D Mixer/Mill.

3.4 Consolidation of W1Ni Composites

After mechanical alloying of composite powders, they were compacted with hydraulic pressing system as shown in Figure 3.10. Capacity of hydraulic pressing was 10 tons, and pressure was applied at 480 MPa (480 x 10^6 N/m^2) for 1 min. Pressing mold diameter was 13 mm and height of the each samples were 5 mm.

Figure 3.10: MSETec MP-0710 hydraulic pressing equipment.

After hydraulic pressing, cold isostatic pressing (CIP) was applied to all samples for getting rid of from porosity. CIP device was shown in the Figure 3.11. The cold isostatic pressing process was at room temperature with a piston diameter of 70 mm and a force value of approximately 150 tons on pre-shaped samples. With the calculations made, it was decided to apply a pressure of approximately 390 MPa. Oil was used to transmit the force in this device, where stress was applied to all axes with the hydraulic system with the Pascal principle. It took about 3.40 min to reach 150 tons in this device. After waiting for 1 min at this value, the force applied in a controlled manner was reduced.

Figure 3.11 : Cold isostatic pressing equipment.

3.5 Activated Sintering of W1Ni Composites

3.5.1 Pressureless sintering

Linn high temperature hydrogen furnace was shown in Figure 3.12. This furnace type was used for sintering W1Ni samples. There were three parts of furnace that are chamber part, gase control and vacuum and software part. There were four resistances in furnace for changing temperature. LPG gas was given for burning H_2 from inside of chamber.

Figure 3.12 : Linn high temperature hydrogen furnace.

For sintering W1Ni composite materials, Linn high temperature hydrogen furnace was used. Samples were holded in vacuum atmosphere until 100 °C. Then, Ar gas was given into chamber between 100-750 °C. Hydrogen gas was used for getting rid of from oxide phases between 750-900 °C. After this period, Ar gas was continuously used. These samples were held at 1400 °C for 1 h. The cooling/heating rate was 10 °C/min.

3.5.2 Spark plasma sintering

For SPS samples, sintering regime was given with the curve in Figure 3.13. As shown in graph, cooling/heating rate was 100 °C/min until 600 °C. Samples were held 5 min at 600 °C. After that, temperature reached to 1410 °C for 1 min with 90 °C/min and cooled. In all this process, pressure was started with 4.4 kN and increased to 9.4 kN.

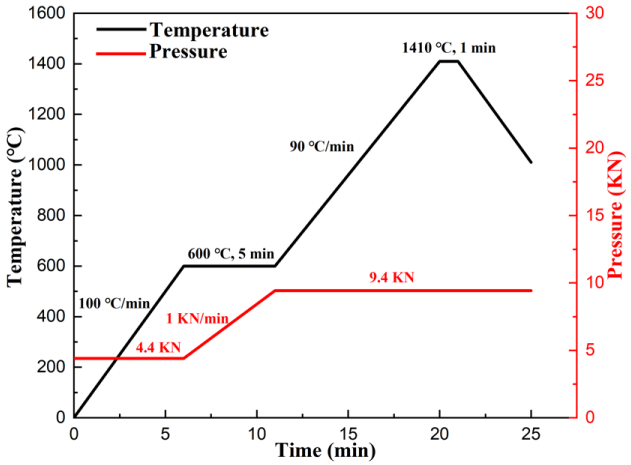

Figure 3.13 : SPS regime of the samples.

3.6 Phase and Microstructure Analyses

Bruker D8 Advanced Series XRD equipment which is shown in Figure 3.14 was used for phase analysis. XRD experiments were conducted with Ni filters at 35 kV, 40 mA and CuK_{α} (λ = 1.5406 Å) radiation to identify occurring phases. Powder and bulk samples were scanned between 10-90° at a scan rate of 2 °/min. Database of ICDD PDF -2 2016 was used in order to phase analysis. Also, crystallite sizes and lattice strains were calculated with DIFFRAC.TOPAS software supplied by Bruker^{TM}.

Figure 3.14 : Bruker D8 Advanced Series XRD equipment.

Particle size and distribution were measured with Microtrac Nano-Flex shown in Figure 3.15a. The analyses were done in alcohol media for boride and boride reinforced W1Ni powders. Multiple measurements were performed due to the

probability of particle agglomeration. The average particle sizes and distributions of the Nd_2O_3, Er_2O_3, B_2O_3 and Mg starting powders were measured by using a Malvern™ Mastersizer 2000 particle size analyzer shown in Figure 3.15b and determined as 5.069 µm, 7.271 µm, 385.994 µm and 107.619 µm, respectively. Also, Bandelin Sonopuls ultrasonic stirring which is shown in Fig. 3.8c was used against particle agglomeration. Solution with particulates was waited for 10 min after ultrasonic stirring in order to provide of Brownian behaviour for particles.

Figure 3.15 : a) Microtrac Nano-Flex particle size analysis device, b) Malvern Mastersizer 2000, and c) Bandelin Sonopuls.

Thermoscientific Quattro S scanning electron microscope (SEM) equipped with energy dispersive spectroscopy (EDS) shown in Figure 3.16 was used to analyze the microstructure of the samples. SEM analyses were performed under high-vacuum atmosphere and prior to SEM analyses. Colorful and point EDS analyses were performed using the EDS equipment to determine elemental distribution.

Figure 3.16 : Thermoscientific Quattro S SEM equipped with EDS.

Transmission electron microscopy (TEM) analysis was done in Sabancı University. TEM device was shown in Figure 3.17. Powder morphology and size were examined and calculated.

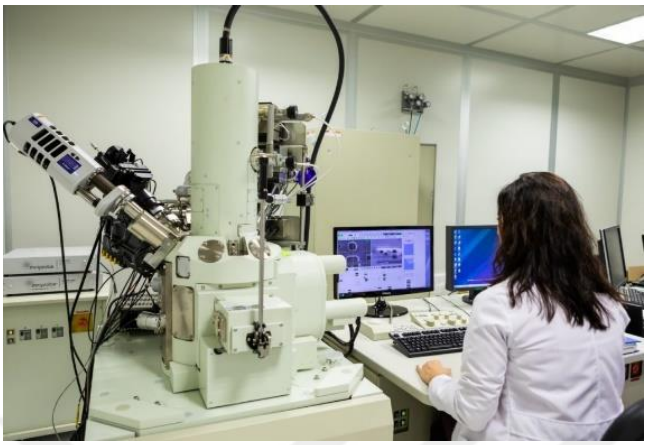

Figure 3.17 : JEOL JEM-ARM200CFEG UHR-TEM (equipped with STEM, Cs corrected STEM, EDS, Gatan Quantum GIF and Digital CCD Camera).

The densities of synthesized boride powders, W1Ni prealloy and boride reinforced W1Ni powders were measured with Micromeritics AccuPycII 1340 pycnometer as shown in Figure 3.18. In this system, the weight of the each samples were entered as input. Then, the chamber was filled with He gas. For an accurate measurement, 10 cycling measurements were performed, and the average of these were reported.

Figure 3.18 : Micromeritics AccuPycII 1340 pycnometer.

Densities of the sintered samples were measured with Archimedes' principle. Weights of the sintered samples in air (W_{air}) and water (W_{water}) were measured with Precisa XB 220A precision balance, and Archimedes' principle apparatus was shown in Figure 3.19. The density (ρ) equation is given Eq. (3.6).

$$\rho = \frac{W_{air}}{W_{air} - W_{water}} \tag{3.6}$$

Figure 3.19 : Schimadzu precision balance equipped with Archimedes' principle apparatus.

The sintered samples and the worn surfaces were examined with the Clemex optical microscope shown in Figure 3.20.

Figure 3.20 : Clemex optical microscope.

3.7 Mechanical Tests

The mechanical properties of the sintered samples were examined with several mechanical tests. Before mechanical tests, the sintered samples were prepared as metallographic. Firstly, the sintered samples were mounted with acrylic resin at Struers Labopress-1 mounting device that is shown in Figure 3.21a. After this process, the sintered samples were ground and polished with Struers Tegrapol-15 automatic grinding and polishing device. Three types of MD-Discs and solutions were used for

grinding and polishing. The mounting device, automatic grinding and polishing device and three types of MD-Discs and solutions were shown in Figure 3.21b.

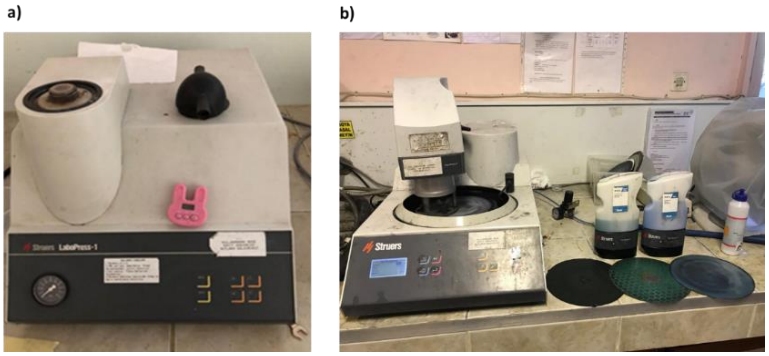

Figure 3.21 : (a) Struers Labopress-1 mounting device and (b) Struers Tegrapol-15 automatic grinding and polishing device and three types of MD-Discs and solutions.

The Vickers hardness measurements were conducted using a Shimadzu HMV microhardness tester given in Figure 3.22. The measurements were conducted with a load of 200 g (1.9604 N) with a dwell time of 10 s. At least 20 indentations were performed on the surfaces of the samples, and the Vickers hardness values were reported as an average of these indentations with standard deviations.

Figure 3.22 : Shimadzu HMV microhardness tester.

In order to examine the wear characteristics of the pressureless sintered and SPS'd samples, the samples were subjected to reciprocating ball-on-disc type wear tests by using Al_2O_3 ball (TRIBOtechnic, 6 mm diameter) as a counterface. Also, wear testing device was shown in Figure 3.23a. Wear testing conditions were selected as a sliding speed of 6 mm/s, sliding distance of 20 m and the wear track length of 2 mm. The tests were performed with a normal load of 4 N at room temperature. The wear depths and widths of the samples were measured with the wear track 2-D profiles screened by a surface profilometer (Veeco Dektak 6 M). Each sample was measured with at least

five different 2-D profiles. The surface profilometer is shown in Figure 3.23b. The average values of the depths and widths were reported as the wear values.

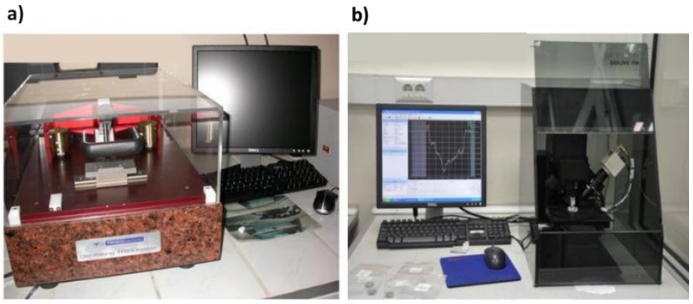

Figure 3.23 : (a) TRIBOtechnic Oscillating TRIBO tester device and (b) Veeco Dektak 6 M surface profilometer.

3.8 He^+ Irradiation Tests

After producing and analysing of the samples, He^+ irradiation tests were applied to samples in Hefei University of Technology (HFUT), China. The He^+ irradiation test was carried in the linear plasma in a plasma-surface interaction system under extreme conditions (PSIEC) device which is shown in Figure 3.24. All samples were arranged as nearly 10 mm diameter and 2 mm height bulk samples. All samples were exposed to 20-eV He^+ ion irradiation with a flux of 1.102×10^{21} ions/(m^2s). Irradiance fluence was set 1.32×10^{24} ions/m^2 with 20 min durations.

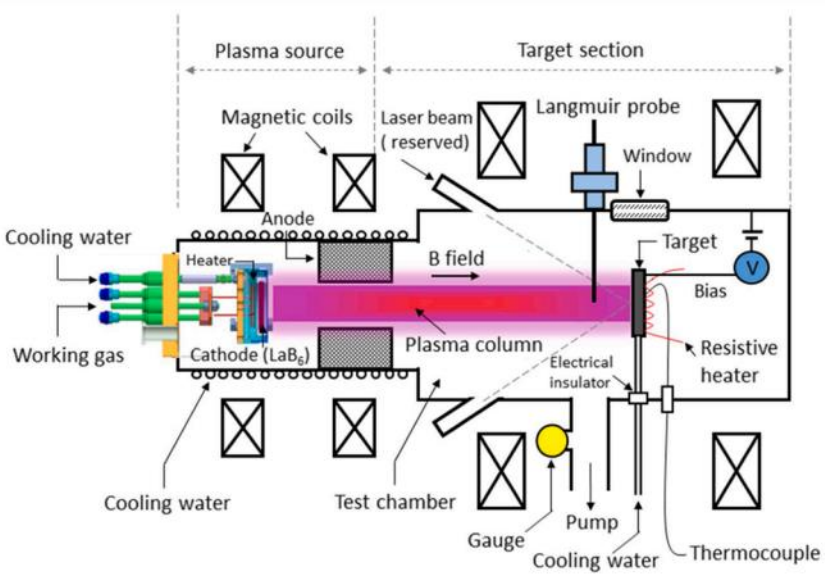

Figure 3.24 : Schematic of linear plasma device (PSIEC) [13].

4. RESULTS AND DISCUSSION

4.1 Powder Characterization of Borides

4.1.1 Cerium boride powders

CeO_2, B_2O_3 and Mg powders were mechanochemically synthesized at different milling time for finding optimum CeB_6 producing conditions. Stoichiometry for the synthesis of CeB_6 from the CeO_2, B_2O_3 and Mg powders was given by the reduction reaction in Eq. (3.1). This production method was tried previously by using a Spex 8000D Mixer/Mill that is shown in Figure **3.9** at 1200 rpm by Ağaoğulları et al [86]. In this thesis, a high energy Nano Multimix Mixer/Mill that is shown in Figure **3.5** was used at 920 rpm (45 Hz) in order to produce CeB_6 powders. Figure **4.1** shows the XRD patterns of the as-blended CeO_2, B_2O_3 and Mg powders and those mechanically milled for different durations up to 7 h. In the XRD pattern of CeB_6 (ICDD Card No: 01-079-1072, Bravais lattice: cubic, a = 0.413 nm), MgO (ICDD Card No: 01-079-0612, Bravais lattice: face centered cubic, a = 0.422 nm) were also detected.

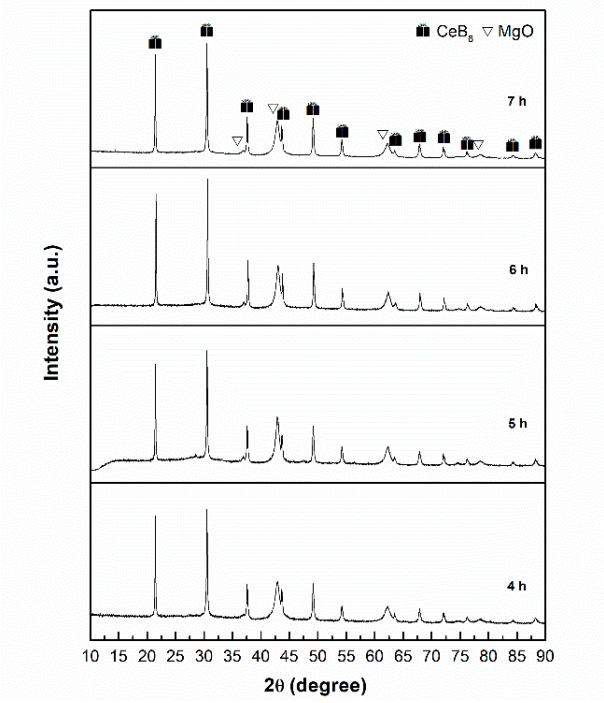

Figure 4.1 : XRD patterns of the CeO_2, B_2O_3 and Mg powders mechanochemically synthesized at 920 rpm for 4 h, 5 h, 6 h and 7 h.

Figure **4.2** illustrates the XRD pattern of the CeB_6 powders mechanochemically synthesized for 5 h and leached with 4 M HCl. As clearly seen, the acid concentration is sufficient to completely remove the MgO phase from the powders. On the other hand, no impurity phases were observed in the XRD pattern within the detection limit of the used diffractometer (≥ 2 wt%). Moreover, based on the XRD pattern, the average crystallite size and lattice parameter of the leached powders was determined as 116.9 nm and 0.508% as shown in Figure **4.2**.

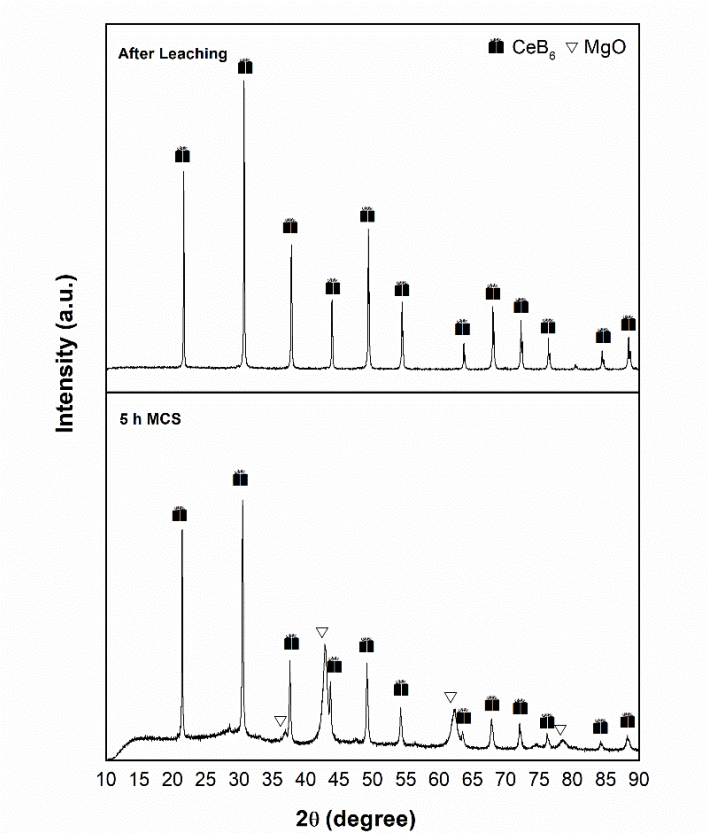

Figure 4.2 : XRD patterns of the CeO_2, B_2O_3 and Mg powders mechanochemically synthesized at 920 rpm for 5 h and subsequently leached with 4 M HCl.

Figure 4.3 shows the scanning electron microscope (SEM) images with different magnifications (15000, 50000 and 100000X). When particles were examined, particle shape nearly showed a mixed morphology [43]. Higher magnification of SEM image given in Figure 4.3c showed that CeB_6 particles ranged between 80 and 120 nm. The general EDS analysis for Figure 4.3b taken from the area in this image reveals the presence of Ce, B, Au and Pd (from the coating) elements. EDS detects the amounts of Ce and B elements as 74.4 wt% and 25.6 wt%.

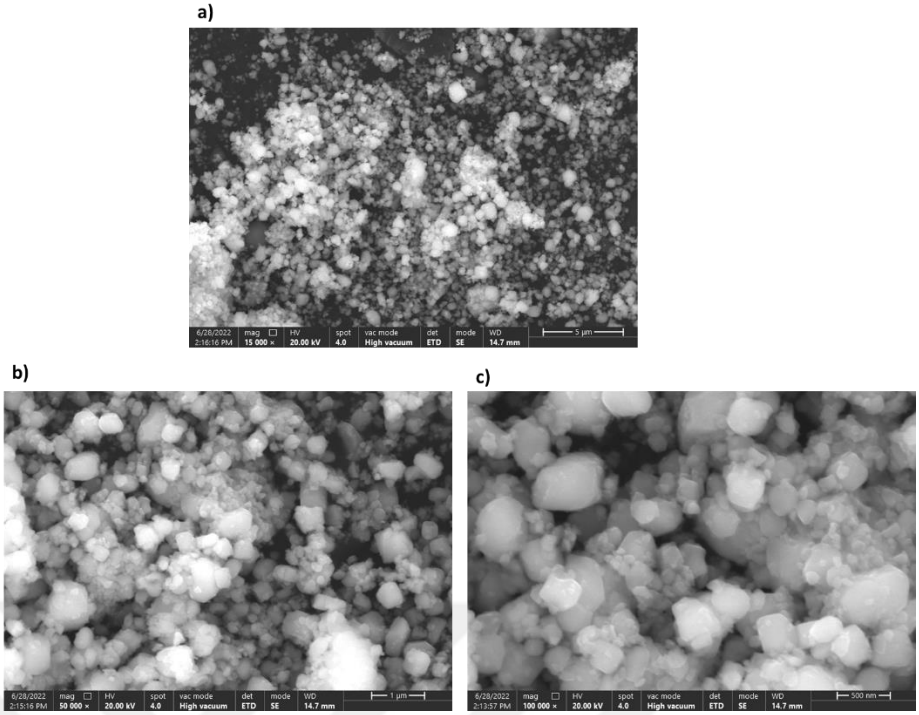

Figure 4.3 : SEM images of CeB_6 powders at different magnifications a) 15000, b) 50000 and c) 100000X.

In addition, the PSA graph as given in Figure 4.4 illustrates that the average particle size of the CeB_6 was about 109 nm which is compatible with the range observed in the SEM image in Figure 4.3c. Lognormal distribution type was observed for this graph. Also, density of pure CeB_6 powders were measured as 4.0882±0.007 g/cm^3.

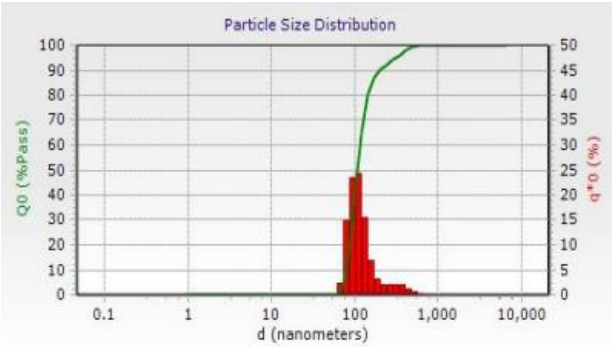

Figure 4.4 : Particle size analysis of CeB_6 powders.

4.1.2 Neodymium boride powders

Prior to the actual simulations, first adiabatic condition was considered assuming no heat loss to the environment and the temperature of the system was found to increase up to 2834 °C with increasing B_2O_3 content. Under this condition, the products were mainly gaseous species (Mg, B_2O_3 and BO) with some Nd_2O_3 and MgO solids remaining. This shows the exothermic nature of the reaction 1 whose ΔH and ΔG

values were calculated to be -3904.9 kJ/mol and -3751.3 kJ/mol at 25 °C, respectively. However, the temperature of our experimental set up is known to be around 600 °C due to the heat loss to the environment. Therefore, the simulations were assumed to take place at lower temperature range to prevent gasification of Mg and B_2O_3 for realistic calculations. Figure **4.5** plots the simulation of the reaction for the stoichiometric reactant mixture (reaction 1, A=6 mole) at varying temperatures under 1 atm atmospheric pressure. It was found that between 25 °C and 400 °C two boride phases were found to form, mainly NdB_4 together with $Mg(B_6)_2$. Also, the reduction product MgO forms small amount of $Mg_3B_2O_6$ with retained excess B_2O_3. This suggests that the fully reduction of B_2O_3 phase may not be completed at lower temperature range. Above this critical temperature (400 °C), the aimed NdB_6 phase is obtained as the sole product of the reaction.

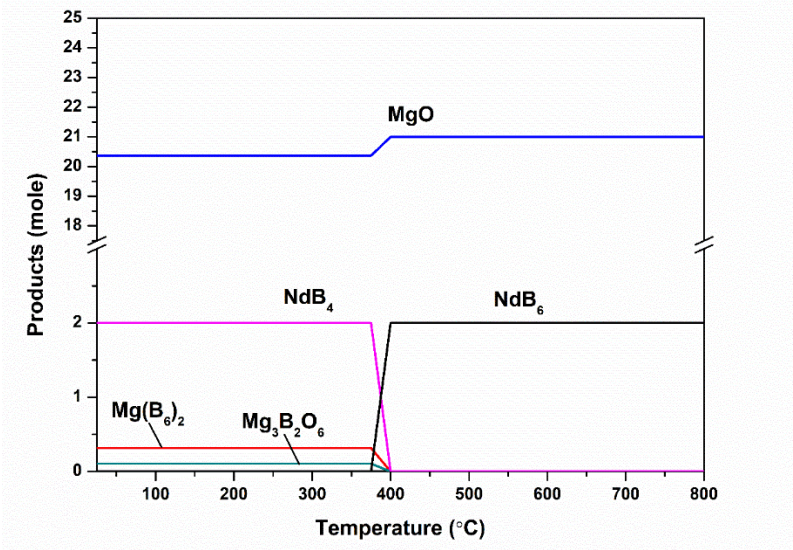

Figure 4.5 : Simulation of the reaction for the stoichiometric reactant mixture.

Figure 4.6 plots the effect of varying B_2O_3 content at fixed 600 °C. Without B_2O_3 addition (A=0), Mg reduces the Nd_2O_3 resulting in the formation of a BCC-A2 (Nd-Mg) solid solution with minor $Mg_{41}Nd_5$ due to the excess metallic Mg in the system. Introduction of the B_2O_3 leads to the formation of NdB_4 and the dissolution of the B into the BCC-A2 phase which eventually transform into an HCP-A3 (Nd-Mg-B) solid solution. Increased B_2O_3 content induces the formation of the NdB_4 which peaks at A=5 and MgB_2 in expense of the HCP-A3 solid solution. Beyond this point NdB_6 becomes the main product, stabilizing after the stoichiometric B_2O_3 amount (A=6).

Excess B_2O_3, has no effect on the boride formation, but starts to react with the MgO slag, forming the $Mg_3B_2O_6$ phase.

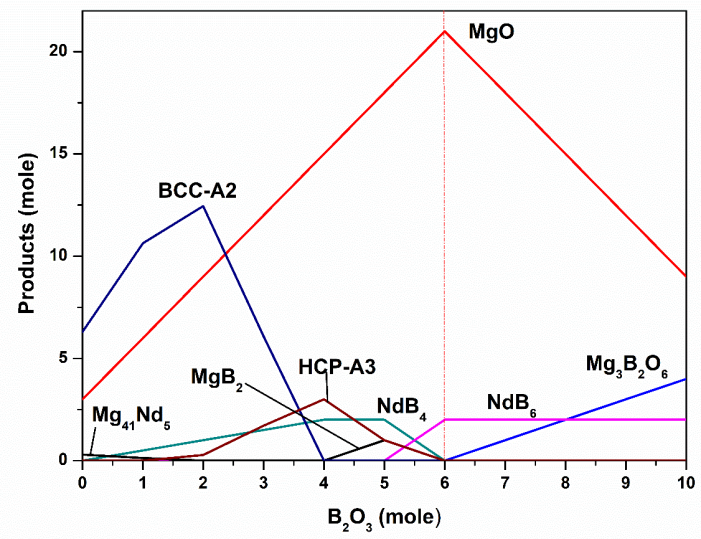

Figure 4.6 : The effect of varying B_2O_3 content at fixed 600 °C.

Figure 4.7a shows the XRD patterns of the as-blended Nd_2O_3, B_2O_3 and Mg powders and those mechanically milled for different durations up to 4 h. In the XRD pattern of the as-blended (non-milled) powders as shown in Figure 4.7a, Nd_2O_3 (ICDD Card No: 00-043-1023, Bravais lattice: hexagonal, a = 0.382 nm and c = 0.599 nm), Mg (ICDD Card No: 00-004-0770, Bravais lattice: primitive hexagonal, a = 0.321 nm and c = 0.521 nm) and $Nd(OH)_3$ (ICDD Card No: 01-083-2035, Bravais lattice: primitive hexagonal, a = 0.329 nm and c = 0.521 nm) phases were detected. The characteristic peaks of B_2O_3 were not observed in the XRD pattern of the as-blended powders because of its amorphous nature. In the XRD patterns of powders milled for 1 h as shown in Figure 4.7a, only Nd_2O_3, Mg and $Nd(OH)_3$ phases are present. Furthermore, the intensities of the Nd_2O_3 and Mg phases decreased with increasing milling time as shown in Figure 4.7a. This indicates a reduction in the average crystallite sizes of the Nd_2O_3 and Mg powders and hence an increase in their reactivity for the forthcoming reduction reaction. Also, $Nd(OH)_3$ phase is not observed with milling. As seen from Figure 4.7a, the powders milled for 1 h contain Nd_2O_3, MgO (ICDD Card No: 01-079-0612, Bravais lattice: face centered cubic, a = 0.422 nm), NdB_6 (ICDD Card No: 03-065-1828, Bravais lattice: primitive cubic, a = 0.413 nm) and NdB_4 (ICDD Card No: 00-024-1458, Bravais lattice: tetragonal, a = 0.722 nm and c = 0.410 nm) phases. Therefore, 1 h milling duration can be considered as the initial point for the formation of the borate and boride phases. At the end of 3 h milling, the only detected phases

were NdB_6 and MgO as shown in Figure 4.7a. XRD graph about 5 and 8 h milling is shown in Figure 4.7b. Therefore, the reaction in Eq. (3.2) completely took place after mechanochemical synthesis conducted by milling for 5 h. Extending the milling duration to 5 h did not change the nature of the resulting products: NdB_6 and MgO phases were still present in the 5 h milled powders and no new phases have formed. Also, after 5 h, new phases and any changing were not observed. XRD patterns of the NdB_6 phase contained twelve peaks (21.507, 30.599, 37.709, 43.821, 49.317, 54.391, 63.704, 68.076, 72.317, 76.46, 84.556, 89.553) which were consistent with the standard NdB_6 pattern as shown in Figure 4.7b. The peak intensities of the NdB_6 and MgO phases gradually decreased from 5 to 8 h milling as seen from Figure 4.7b. When literature was examined, NdB_6 phases without impurities can be produced at 1500 ºC for 4 h holding time [74]. Also, after combustion synthesis at 20 MPa, products that are NdB_6, MgO and a few $Mg_3B_2O_6$ and $Nd_2B_2O_6$ were leached with 20 wt% H_2SO_4 for obtaining single NdB_6 whose purity is 98.6 % [77]. Boron-rich rare-earth boride NdB_6 was synthesized at 1600 °C and 4.0 GPa pressure at a duration of 1.5 min [81]. These methods require more time to reach the synthesis temperature and hence more energy for obtaining NdB_6. However, these rare-earth borides can be produced in shorter time and with less energy via mechanochemical synthesis.

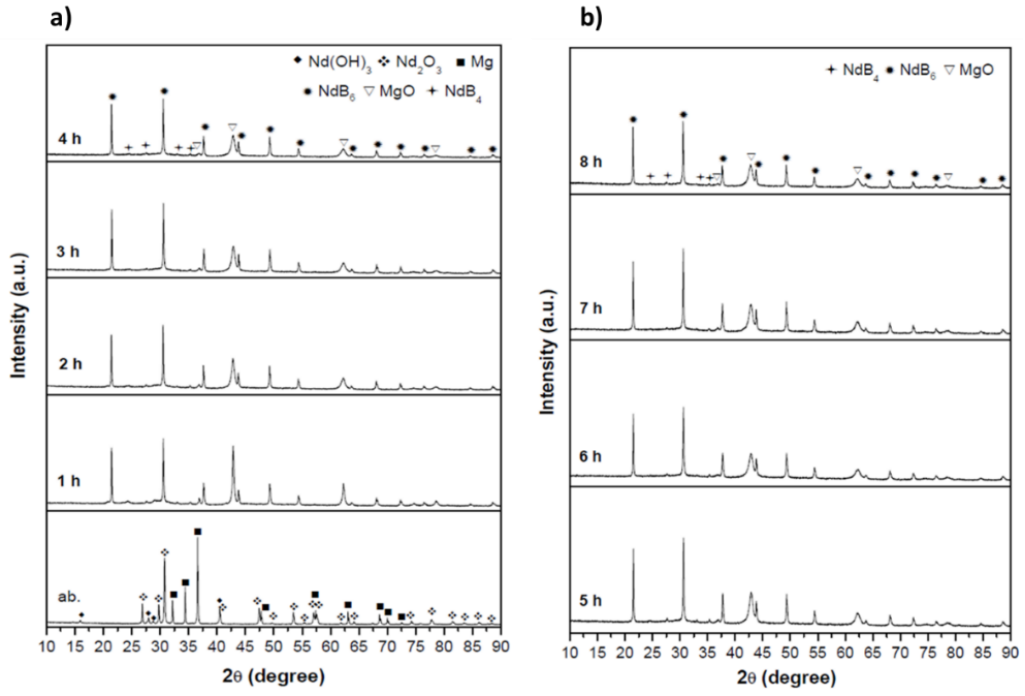

Figure 4.7 : XRD patterns of the a) Nd_2O_3, B_2O_3 and Mg powders and mechanochemically synthesized at 920 rpm for 1 h, 2 h, 3 h and 4 h and b) 5 h, 6 h ,7 h and 8 h.

Figure 4.8 shows XRD patterns of the Nd_2O_3, B_2O_3 and Mg powders: as-blended, 2 h, 4 h, 5 h, 6 h, 7 h and 8 h mechanochemically synthesized at 1188 rpm. After 2 h, only NdB_6, NdB_4 and MgO were observed.

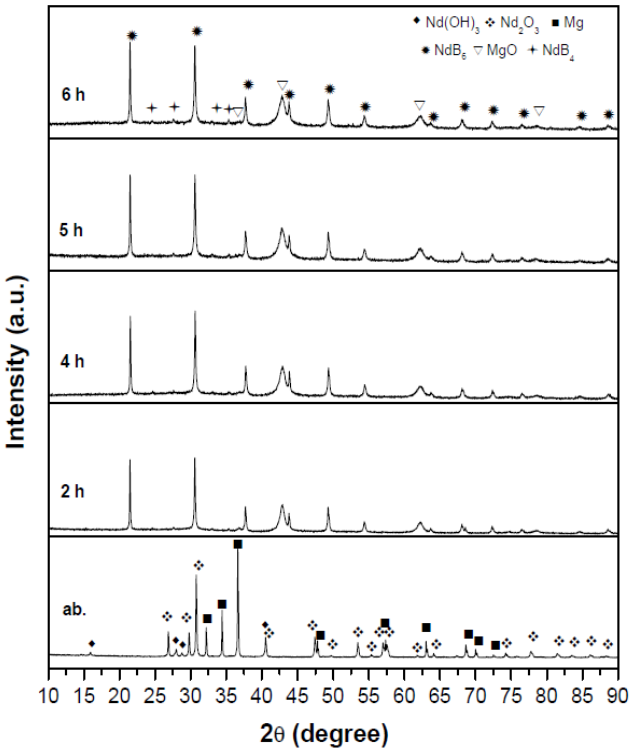

Figure 4.8 : XRD patterns of the Nd_2O_3, B_2O_3 and Mg powders as-blended, 2 h, 4 h, 5 h, 6 h, 7 h and 8 h mechanochemically synthesized at 1188 rpm.

Figure 4.9a illustrates average crystallite size and lattice strain of the milled powders up to 8 h. On the basis of the related XRD patterns, the average crystallite sizes of the NdB_6 phase in the powders milled for between 2 and 8 h were calculated as 92.6, 91.86, 89.08, 85.52, 83.32, 80.62 and 76.68 nm, respectively. Lattice strains of the NdB_6 phase in the powders milled for between 2 and 8 h were calculated as 0.344, 0.319, 0.311, 0.322, 0.339, 0.367, 0.355 and 0.375 %, respectively. Figure 4.9b shows average crystallite size and lattice strain of the milled powders up to 6 h. On the basis of the related XRD patterns, the average crystallite sizes of the NdB_6 phase in the powders milled for between 2 and 6 h were calculated as 121.93, 80.13, 71.3 and 71.67 nm, respectively. Lattice strains of the NdB_6 phase in the powders milled for between 2 and 6 h were calculated as 0.330, 0.456, 0.511 and 0.512 %.

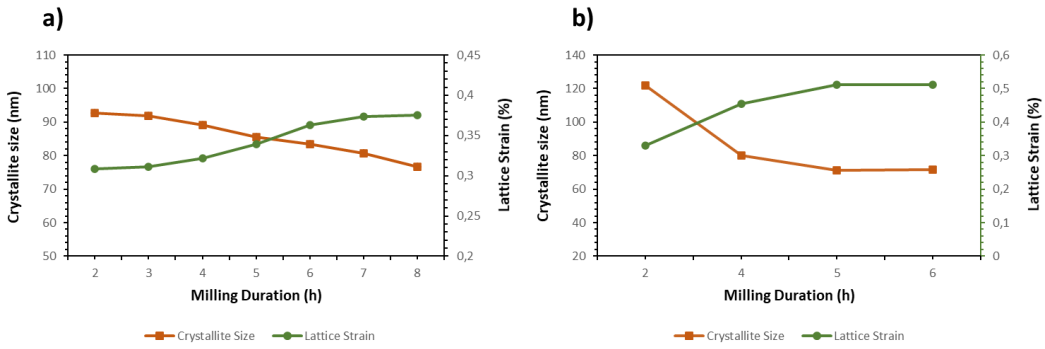

Figure 4.9 : Average crystallite sizes and lattice strains of NdB_6 versus milling duration curves: a) MCS at 920 rpm and b) MCS at 1188 rpm.

Figure **4.10** illustrates the XRD pattern of the NdB_6 powders mechanochemically synthesized at different milling speed for 5 h and leached with 6 M HCl. As clearly seen, the acid concentration is sufficient to completely remove the MgO phase from the powders. On the other hand, no impurity phases were observed in the XRD pattern within the detection limit of the used diffractometer (≥ 2 wt.%). Moreover, based on the XRD pattern, the average crystallite size and lattice parameter of the leached powders were determined as 117.3 nm and 0.166064 % (MCS at 920 rpm) as shown in Figure **4.10**a, and 53.45 nm and 0.348149 % (MCS at 1188 rpm) as shown in Figure **4.10**b.

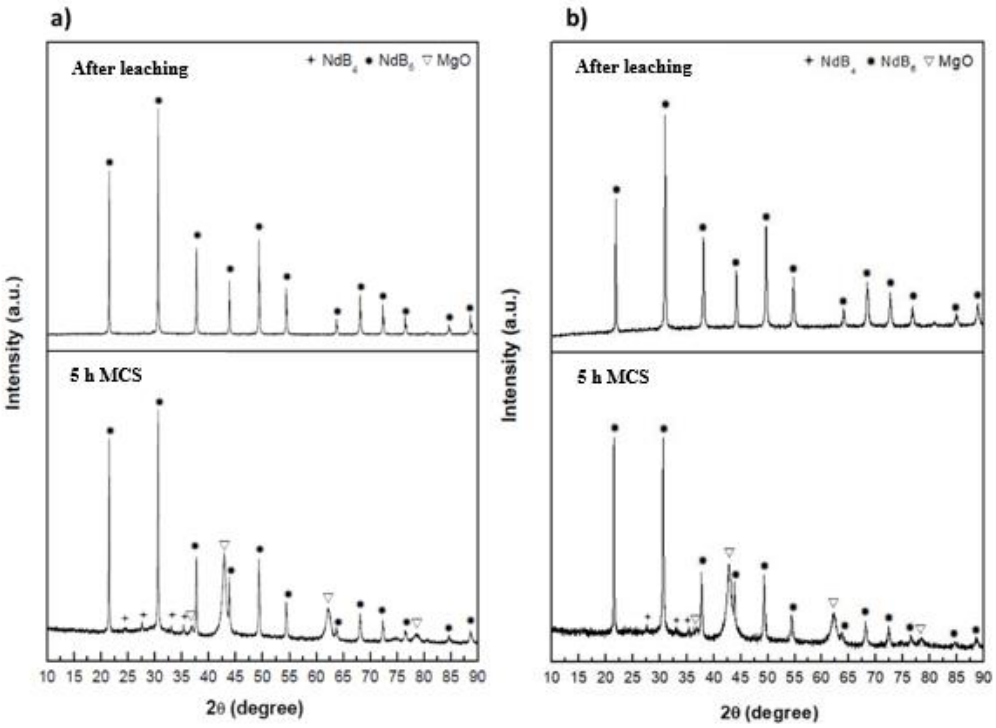

Figure 4.10 : XRD patterns of the Nd_2O_3, B_2O_3 and Mg a) MCS at 920 rpm for 5 h and b) MCS at 1188 rpm for 5 h with leaching 6 M HCl.

Different molarities of HCl acid were also tried for leaching. XRD results were given in Figure 4.11. MgO phase was observed in 2 M leached powders. However, any impurity was not observed in 4 M leached powders. So that, 4 M HCl acid solution was chosen for further leaching treatments.

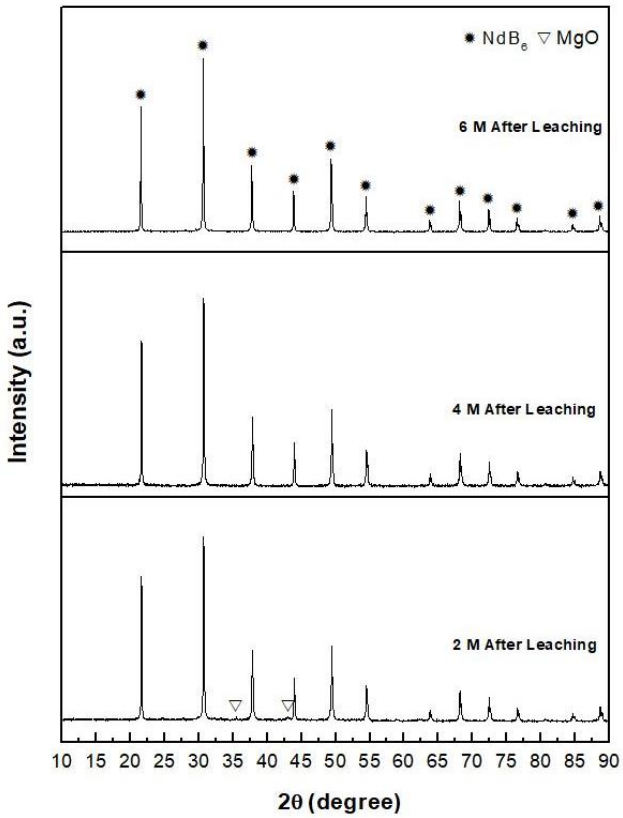

Figure 4.11 : XRD results of NdB_6 powders after 2, 4 and 6 M HCl leaching.

Figure 4.12 shows SEM images with different magnifications (13000, 50000 and 100000X). Particle shape was mixed morphology as seen in SEM images. Higher magnification of SEM image as given in Figure 4.12c for NdB_6 particle size were between 80 and 120 nm. Figure 4.12b shows that the general EDS analysis was taken from the area in this image reveals the presence of Nd, B, Au and Pd (from the coating) elements. Also, amount of Nd and B was measured 35.83% and 64.17% as atomic percentage.

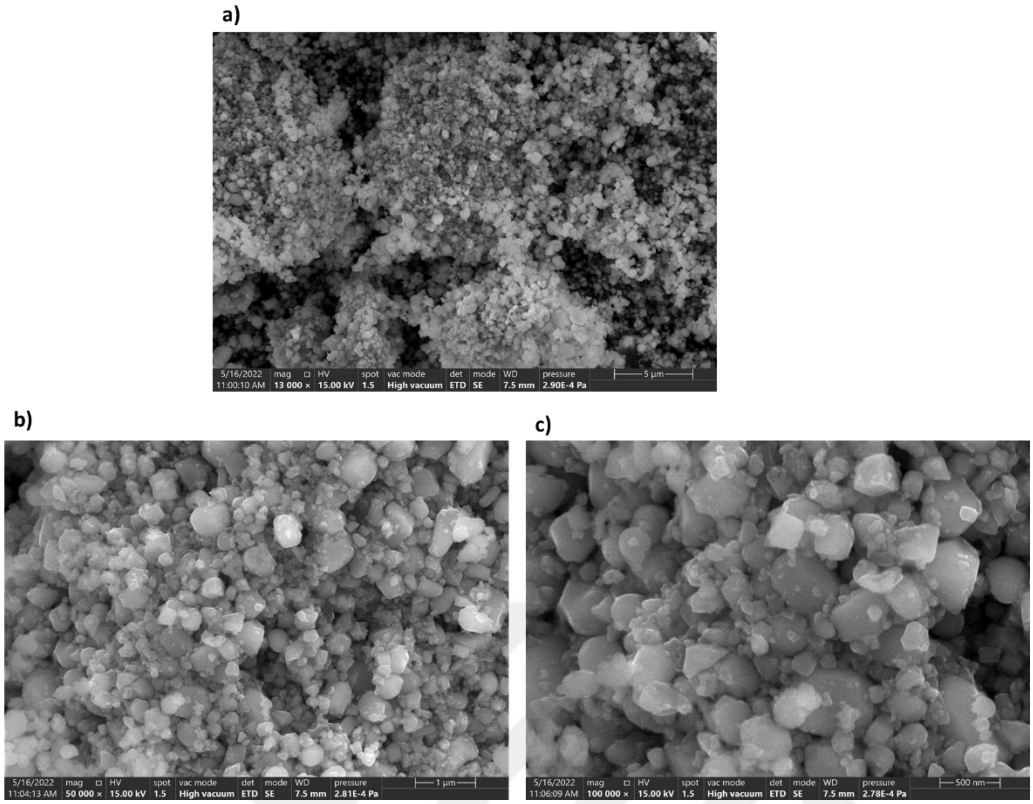

Figure 4.12 : SEM images of NdB_6 powders for different magnifications a) 13000, b) 50000 and c) 100000X.

In addition, the PSA graph as given in Figure 4.13 illustrates that the average particle size of the NdB_6 was about 118.9 nm which is in the similar range observed in the SEM image in Figure 4.12c. Lognormal distribution type was observed for this graph. Also, density of pure NdB_6 powders were measured as 4.0304±0.015 g/cm^3.

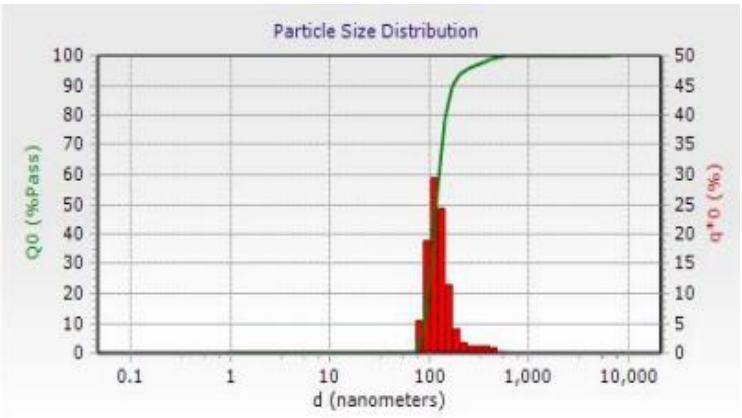

Figure 4.13 : Particle size analysis of NdB_6 powder.

Transmission electron microscopy images were given in the Figure 4.14, average powder particle sizes were nearly 150-180 nm. Also, particle shape was in the mixed morphology.

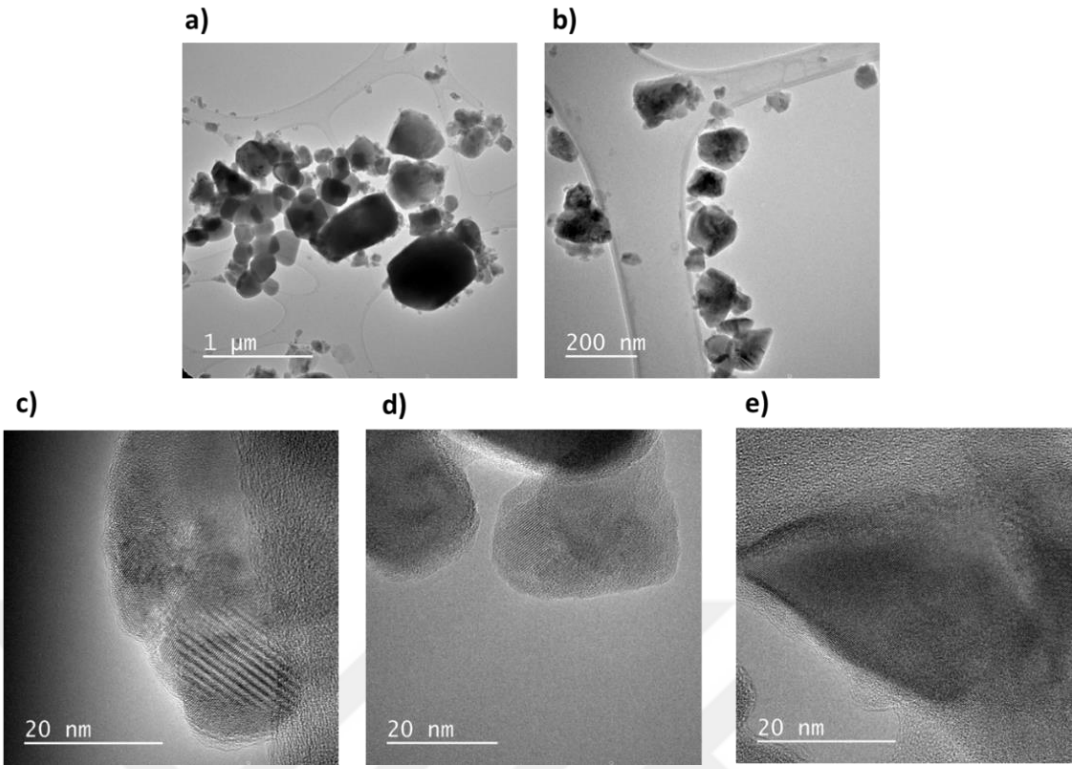

Figure 4.14 : TEM analysis images for NdB_6 which is leached with 6 M HCl acid.

As a stoichiometric reactant mixture calculation Figure 4.15, NdB_4 phases started to observe with decreasing B_2O_3. Different loss amount of B_2O_3 was tried with 5 h MCS. XRD results of this study is given in Figure 4.15. Stoichiometric (0 % excess B_2O_3) shows Eq. (3.2). When B_2O_3 was decreased about 5 and 15% amount in the stoichiometric powder batch, it equals to Eq. (3.3) and Eq. (3.4), respectively. Production of NdB_4 did not happened in the stoichiometric ratio, so that B_2O_3 continued to be reduced. Finally, NdB_4 was obtained with 30% B_2O_3 deficiency. NdB_6 and NdB_4 phases were produced together with loss of 20% B_2O_3.

After MCS, obtained NdB_4 powders were leached with 4 M HCl. XRD patterns were given in Figure **4.16**. As results, NdB_4 powders could be produced. XRD patterns of NdB_4 phase had 21 peaks with these values of 21.819º, 24.850º, 27.769º, 33.203º, 35.538º, 39.618º, 41.825º, 44.277º, 45.618º, 51.376º, 52.389º, 53.01º, 54.024º, 57.361º, 58.887º, 70.844º, 72.222º, 74.267º, 75.583º, 77.175º and 81.253º.

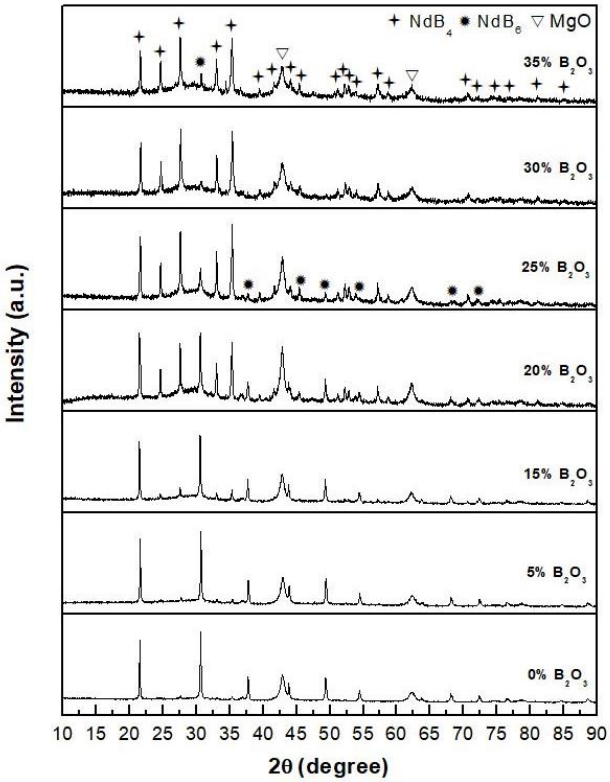

Figure 4.15 : XRD patterns of the Nd_2O_3, B_2O_3 and Mg MCS mechanochemically synthesized at 920 rpm for 5 h with leaching 4 M HCl.

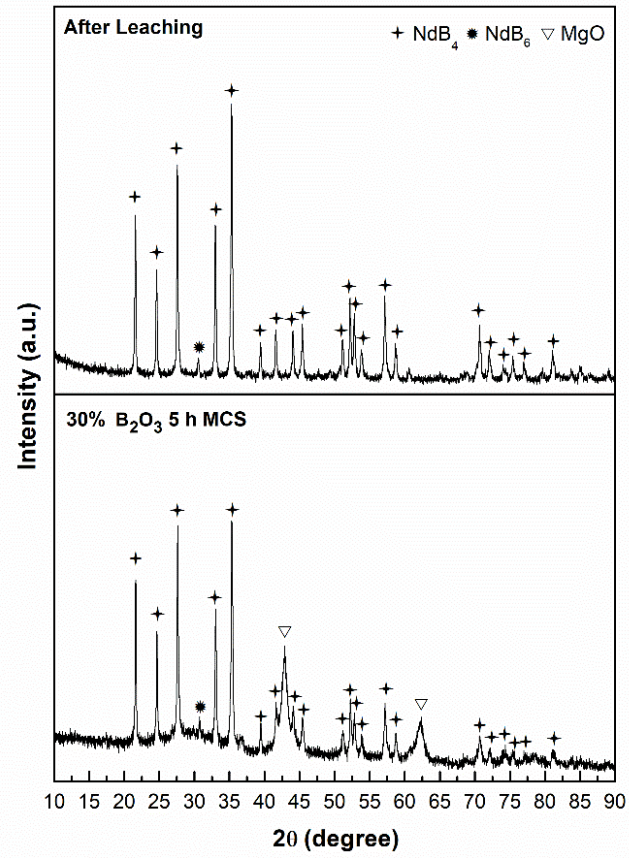

Figure 4.16 : XRD patterns of the Nd_2O_3, loss of 30% B_2O_3 and Mg mechanochemically synthesized at 920 rpm for 5 h and after leaching with 4 M.

Rietveld analysis of NdB_4 was given in Figure 4.17. While amount of NdB_6 was nearly 0.4%, it was 99.6% for NdB_4 based on the Rietveld analysis. Lattice parameter of NdB_4 were calculated as a : 0.721 nm, c : 0.410 nm. These values were nearly same with taken lattice parameter from PDF cards.

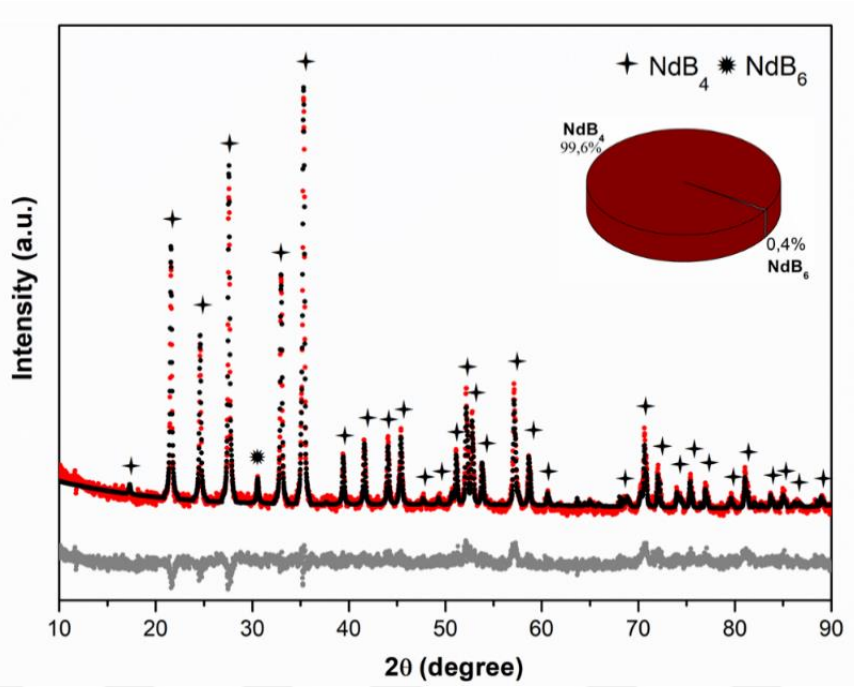

Figure 4.17 : Rietveld analysis of NdB_4 powders; R_p : 4.94, R_{wp} : 6.17, GoF : 1.68, R_{Bragg} of NdB_4 : 4.62 and R_{Bragg} of NdB_6 : 3.69.

Figure 4.18 shows SEM images with different magnifications (15000, 60000 and 120000X). When particles were examined, particle shape was nearly mix morphology. Higher magnification of SEM image as shown in Figure 4.18c for NdB_6 particles ranging was between 80 and 120 nm. The general EDS analysis for Figure 4.18b was taken from the area in this image reveals the presence of Nd, B, Au and Pd (from the coating) elements were observed. Also, amount of Nd and B was measured 29.1% and 70.9% as atomic percentage.

In addition, the PSA graph given in Figure 4.19 illustrates that the average particle size of the NdB_6 was about 85.6 nm which is in the same range observed in the SEM image in Figure 4.18c. Lognormal distribution type was observed for this graph. Also, density of pure NdB_4 powders were measured as 5.0240±0.011 g/cm^3.

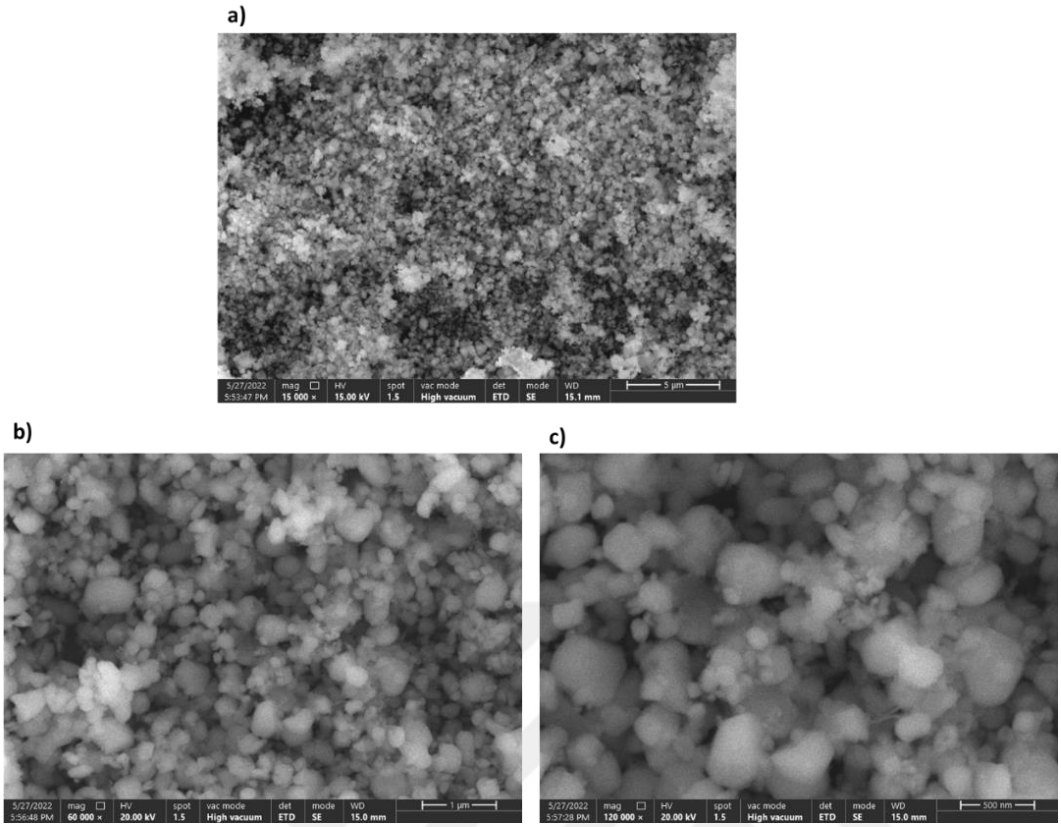

Figure 4.18 : SEM images of NdB_6 powders for different magnifications a) 15000, b) 60000 and c) 120000X.

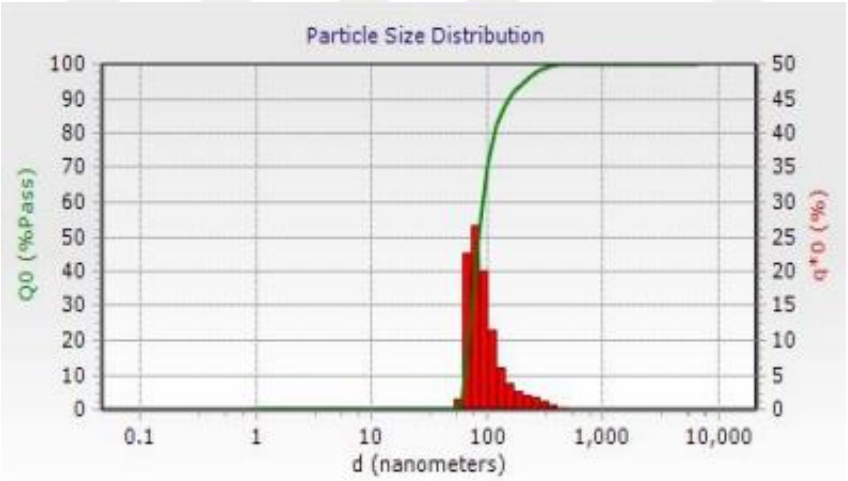

Figure 4.19 : Particle size analysis of NdB_4 powder.

After MCS, simultaneously obtained NdB_6 and NdB_4 powders were leached with 4 M HCl. XRD analysis was given in Figure **4.20**. As results, NdB_6 and NdB_4 powders were produced properly.

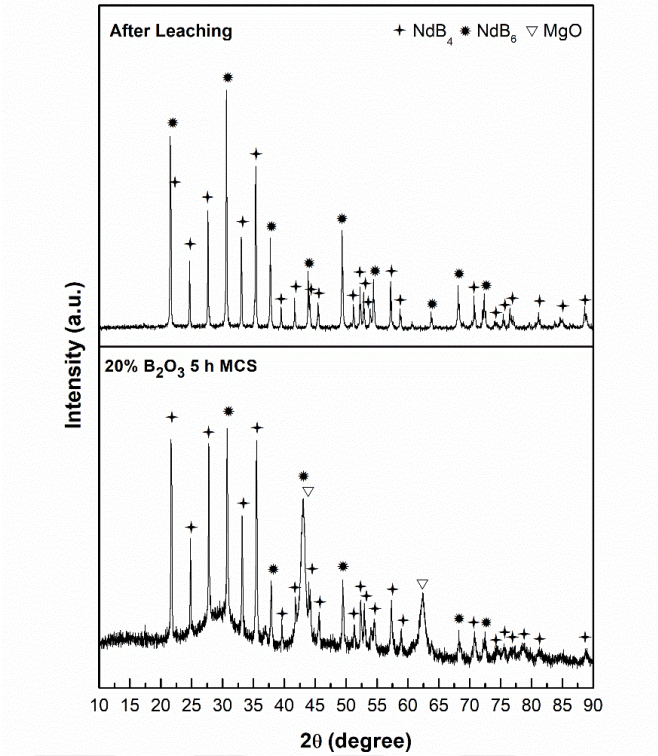

Figure 4.20 : XRD patterns of the Nd_2O_3, loss of 20% B_2O_3 and Mg mechanochemically synthesized at 920 rpm for 5 h and after leaching with 4 M.

Rietveld analysis of simultaneously producing of NdB_6 and NdB_4 powders were given in Figure 4.21. As, amount of NdB_6 and NdB_4 was approximately calculated 49% and 51%, respectively. Lattice parameter of NdB_6 and NdB_4 were calculated as a : 0.413 nm (cubic) and a : 0.721 nm, c : 0.410 nm (tetragonal), respectively. These values were nearly same with taken lattice parameter from PDF cards.

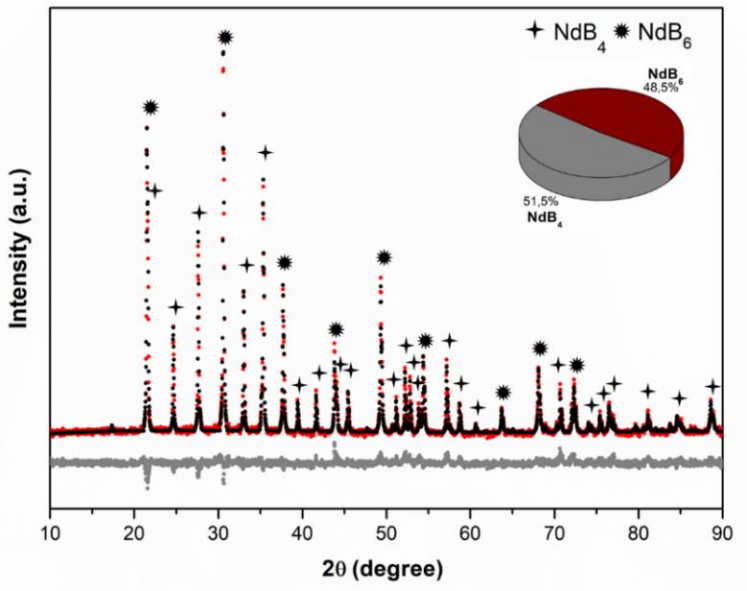

Figure 4.21 : Rietveld analysis of NdB_4 and NdB_6 powders; R_p : 4.5, R_{wp} : 5.79, GoF : 1.41, R_{Bragg} of NdB_4 : 4.86 and R_{Bragg} of NdB_6 : 3.02.

Figure 4.22 shows SEM images with different magnifications (15000, 60000 and 120000X). When particles were examined, particle shape was nearly mix morphology. Higher magnification of SEM image as shown in Figure 4.22c for NdB_6 and NdB_4 powders with together ranging was between 80 and 150 nm. The general EDS analysis for Figure 4.22b was taken from the area in this image reveals the presence of Nd, B, Au and Pd (from the coating) elements were observed. Also, amount of Nd and B was measured 29.1% and 70.9% as atomic percentage.

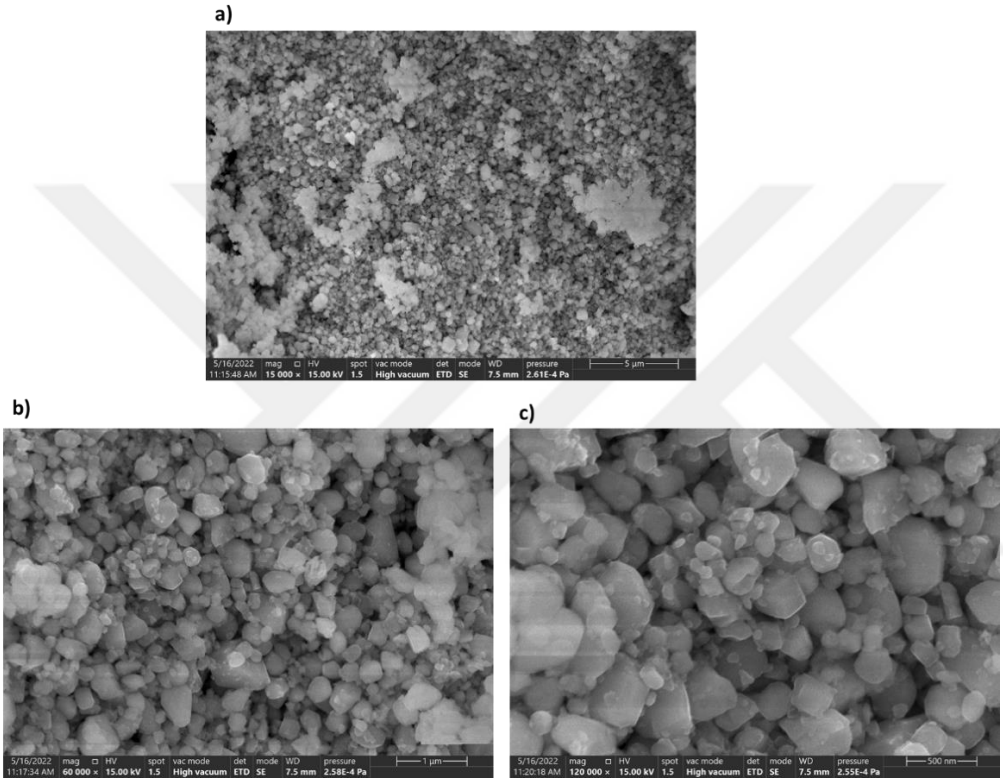

Figure 4.22 : SEM images of NdB_6 and NdB_4 powders with together for different magnifications a) 15000, b) 60000 and c) 120000X.

In addition, the PSA graph as given in Figure 4.23 illustrates that the average particle size of the pure NdB_6 and NdB_4 powder was about 136.6 nm which is in the range observed in the SEM image in Figure 4.22c. Lognormal distribution type was observed for this graph. Also, density of pure NdB_6 and NdB_4 powders with together were measured as 4.0911±0.003 g/cm^3.

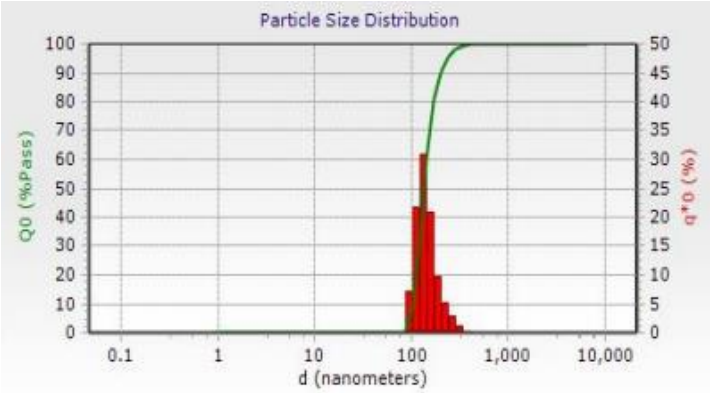

Figure 4.23 : Particle size analysis simuntenuosly producing NdB_6 and NdB_4 powders.

4.1.3 Erbium boride powders

Er_2O_3, B_2O_3 and Mg powders were mechanochemically syntesized up to 8 h for producing ErB_4 powders. Figure **4.24**a shows the XRD patterns of the as-blended Er_2O_3, B_2O_3 and Mg powders and those mechanically milled for different durations up to 4 h. In the XRD pattern of the as-blended (non-milled) powders as shown in Figure **4.24**, E_2O_3 (ICDD Card No: 03-065-3175, Bravais lattice: cubic, a = 1.053 nm), Mg (ICDD Card No: 00-035-0821, Bravais lattice: primitive hexagonal, a = 0.321 nm and c = 0.521 nm) phases were detected. The characteristic peaks of B_2O_3 were not observed in the XRD pattern of the as-blended powders because of its amorphous nature. As seen from Figure **4.24**, the powders milled for 1 h contain Er_2O_3, MgO (ICDD Card No: 00-045-0946, Bravais lattice: face centered cubic, a = 0.422 nm), ErB_4 (ICDD Card No: 01-089-3552, Bravais lattice: tetragonal, a = 0.4 nm) phases. Therefore, 1 h milling duration can be considered as the initial point for the formation of the borate and boride phases. At the end of 4 h milling, the only detected phases were ErB_4 and MgO as shown in Figure **4.24**. Also, XRD patterns of mechanically alloyed between 5 and 8 h are given in Figure **4.24**b. XRD graph about 5 and 8 h milling is shown in Figure **4.24**b. Therefore, the reaction in Eq. (3.5) completely took place after mechanochemical synthesis conducted by milling for 5 h. Extending the milling duration to 5 h did not change the nature of the resulting products: ErB_4 and MgO phases were still present in the 5 h milled powders and no new phases have formed. Also, after 5 h, new phases and any changing were not observed. Optimum time was choosen as 5 h for leaching. XRD patterns of the ErB_4 phase contained twentyseven peaks which were consistent with the standard ErB_4 pattern as shown in Figure **4.24**b. The peak intensities of the ErB_4 and MgO phases gradually decreased

from 5 to 8 h milling as seen from Figure **4.24**b. ErB_4 peaks had 22 peaks (17.726, 22.206, 25.17, 28.199, 33.810, 36.182, 40.303, 42.614, 45.305, 46.492, 53.382, 54.221, 55.059, 58.513, 60.095, 62.227, 70.585, 72.554, 73.974, 76.258, 77.653, 78.876º). In literature, there is no too much information about producing ErB_4. In one study, the polycrystal of ErB_4 was produced with the borothermal reduction of metal from its oxide in a vacuum (5 10-5 Torr, 1750 ºC, and 2.5 h) [85]. These rare-earth borides can be produced shorter time and less energy with mechanochemical synthesis.

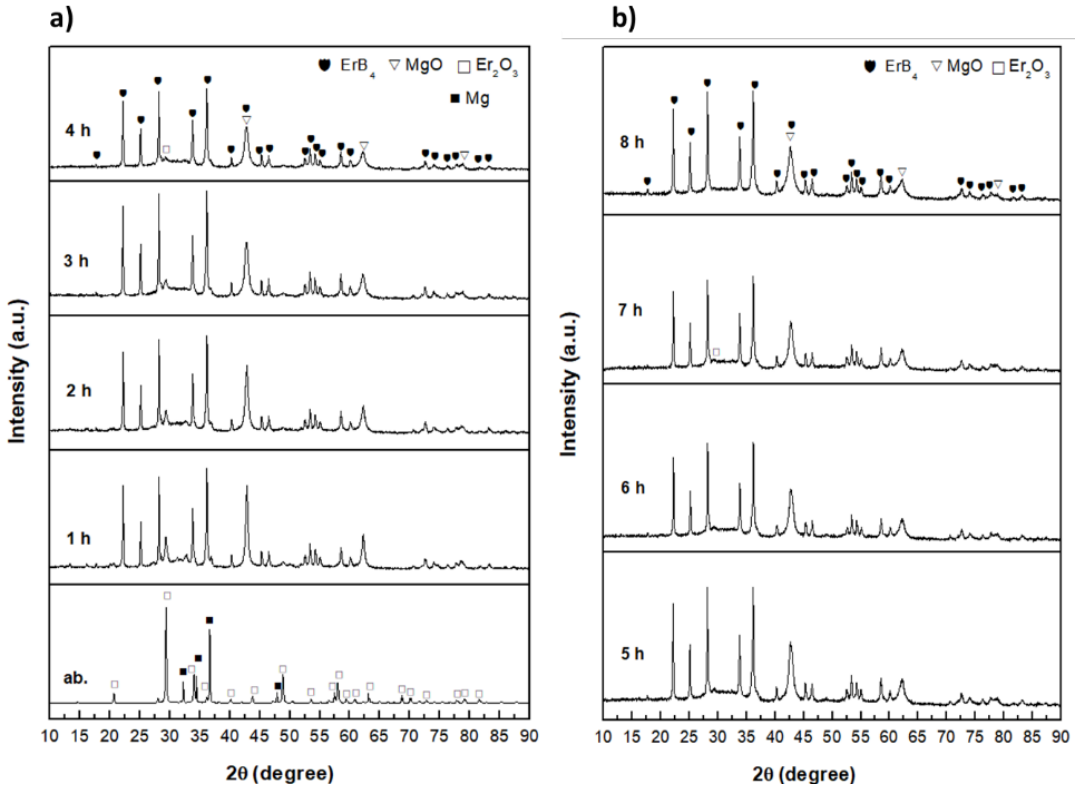

Figure 4.24 : XRD patterns of the Er_2O_3, B_2O_3 and Mg powders a) as-blended, 1 h, 2 h, 3 h and 4 h and b) 5 h, 6 h ,7 h and 8 h mechanochemically synthesized at 920 rpm.

Figure 4.25 shows XRD patterns of the Er_2O_3, B_2O_3 and Mg powders as-blended, 2 h, 4 h, 5 h, 6 h, 7 h and 8 h with mechanochemically synthesized at 1188 rpm. After 2 h, only ErB_4 and MgO were observed.

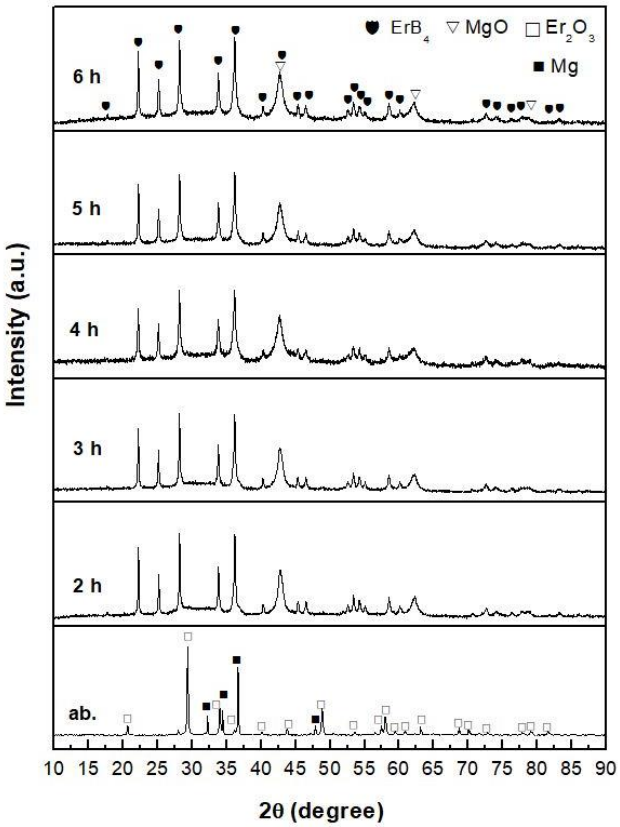

Figure 4.25 : XRD patterns of the Er_2O_3, B_2O_3 and Mg powders as-blended and 2 h, 4 h, 5 h, 6 h, 7 h and 8 h with mechanochemically synthesized at 1188 rpm.

Figure **4.26**a illustrates average crystallite size and lattice strain of mechanochemically synthesized at 920 rpm powders up to 8 h. On the basis of the related XRD patterns, the average crystallite sizes of the ErB_4 phase in the powders milled for between 2 and 8 h were calculated as 89.8, 96.67, 89.83, 78.9, 78.33, 74.4 and 71.6 nm, respectively. Lattice strains of the ErB_4 phase in the powders milled for between 2 and 8 h were calculated as 0.431, 0.441, 0.436, 0.453, 0.556, 0.546, 0.569 and 0.588%. Figure **4.26**b shows average crystallite size and lattice strain of mechanochemically synthesized at 1188 rpm powders up to 6 h. On the basis of the related XRD patterns, the average crystallite sizes of the ErB_4 phase in the powders milled for between 2 and 6 h were calculated as 131.6, 118.03, 108.07, 104.5 and 80.7 nm respectively. Lattice strains of the ErB_4 phase in the powders milled for between 2 and 6 h were calculated as 0.357, 0.384, 0.396 and 0.503%.

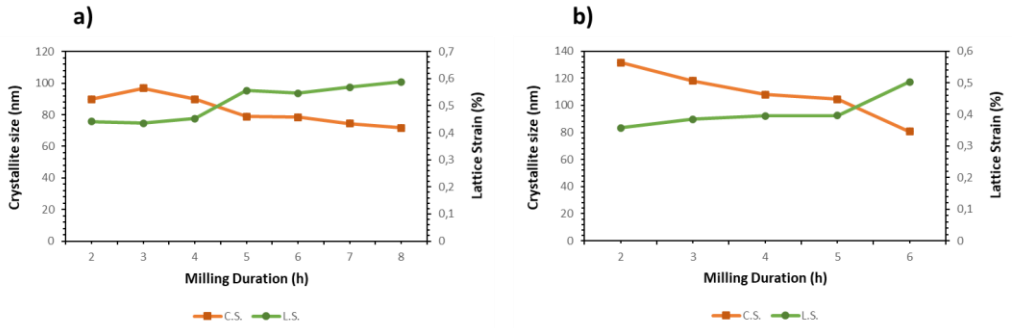

Figure 4.26 : Average crystallite sizes and lattice strains of ErB_4 versus milling duration curves as MCS with a) 920 rpm and b) 1188 rpm.

Figure **4.27** illustrates the XRD pattern of the ErB_4 powders with different milling speed (920 and 1188 rpm) and milling time (5 and 3 h) and leached with 6 M HCl. As clearly seen, the acid concentration was sufficient to completely remove the MgO phase from the powders. On the other hand, no impurity phases were observed in the XRD pattern within the detection limit of the used diffractometer (≥2 wt.%). Moreover, based on the XRD pattern, the average crystallite size and lattice parameter of the leached powders was determined as 94.64 nm and 0.2275% as shown in Figure **4.27**a and 57.02 nm and 0.4099% as shown in Figure **4.27**b.

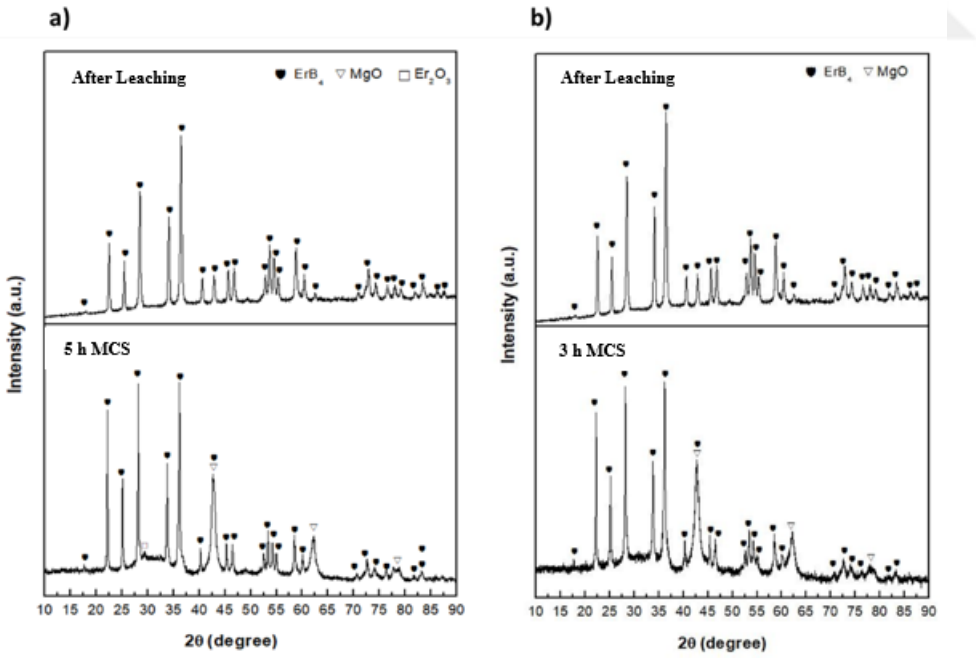

Figure 4.27 : XRD patterns of the Er_2O_3, B_2O_3 and Mg mechanochemically synthesized at a) 920 rpm for 5 h and b) 1188 rpm for 3 h and after leaching with 6 M.

Different molarities of HCl acid were tried for leaching. XRD results were given in Figure 4.28. As results, MgO phases were observed in 4 M leaching. However, any impurity was not observed in 6 M leaching. So that, 6 M HCl acid was chosen for leaching.

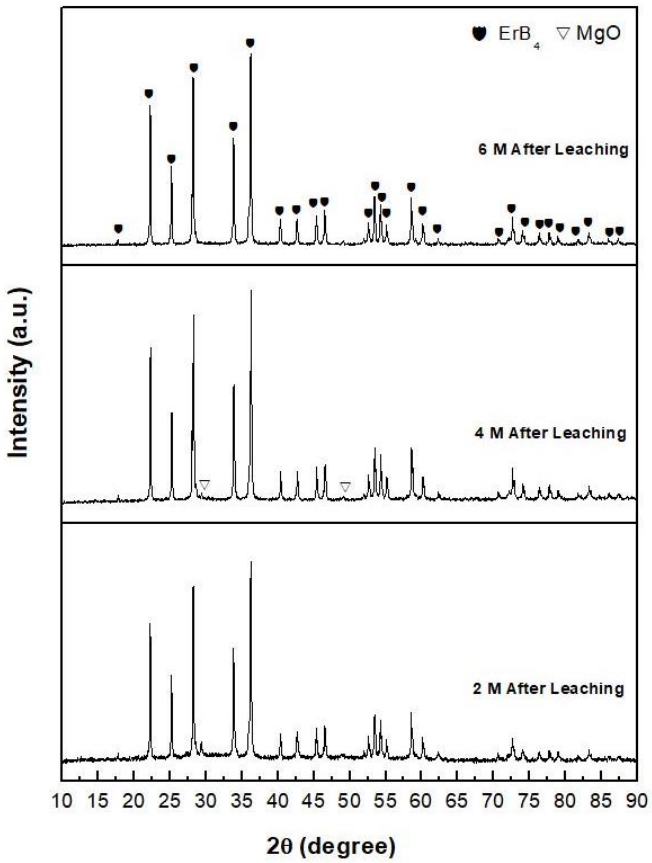

Figure 4.28 : XRD results of ErB_4 powders after 2, 4 and 6 M leaching.

Figure 4.29 shows SEM images with different magnifications (15000, 50000, and 100000X). When particles were examined, particle shape was nearly mix morphology. Higher magnification of SEM image as shown in Figure 4.29c for ErB_4 particles ranging was between 80 and 120 nm. The general EDS analysis for Figure 4.29b was taken from the area in this image reveals the presence of Er, B, Au and Pd (from the coating) elements were observed. Also, amount of Er and B was measured 70.8% and 29.2% as atomic percentage.

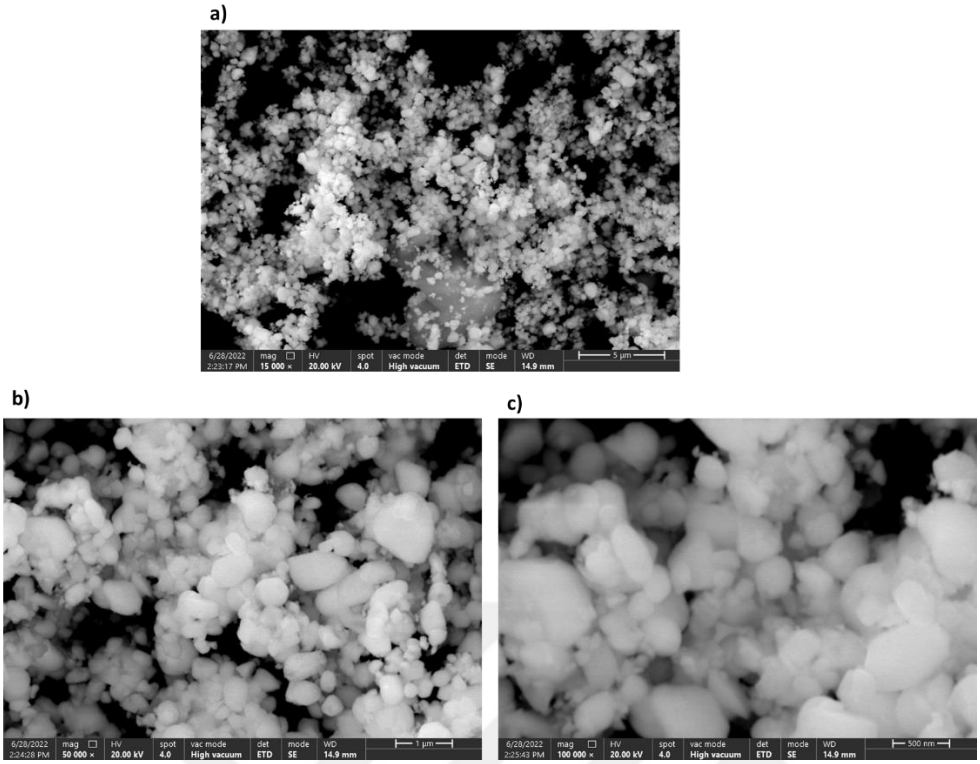

Figure 4.29 : SEM images of ErB_4 powders for different magnifications a) 15000, b) 50000 and c) 100000X.

In addition, the PSA graph as given in Figure 4.30 illustrates that the average particle size of the ErB_4 was about 100.4 nm which is in the range observed in the SEM image in Figure 4.29c. Lognormal distribution type was observed for this graph. Also, density of pure ErB_4 powders were measured as 6.1546±0.015 g/cm^3.

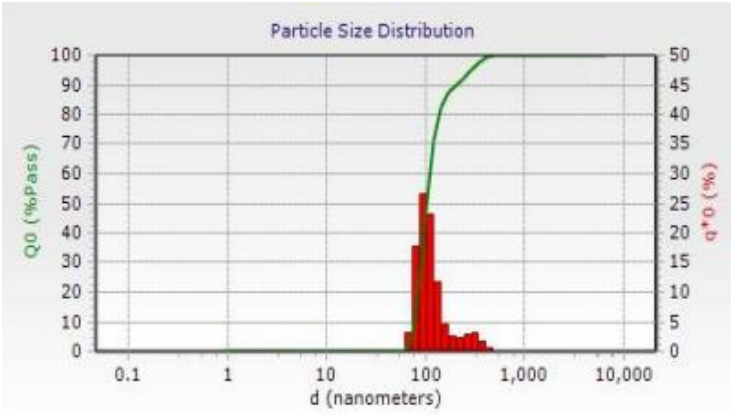

Figure 4.30 : Particle size analysis of ErB_4 powder.

Transmission electron microscopy images were given in the Figure 4.31, average powder particle sizes were nearly between 150 and 180 nm. Also, particle shape was at a mixed morphology.

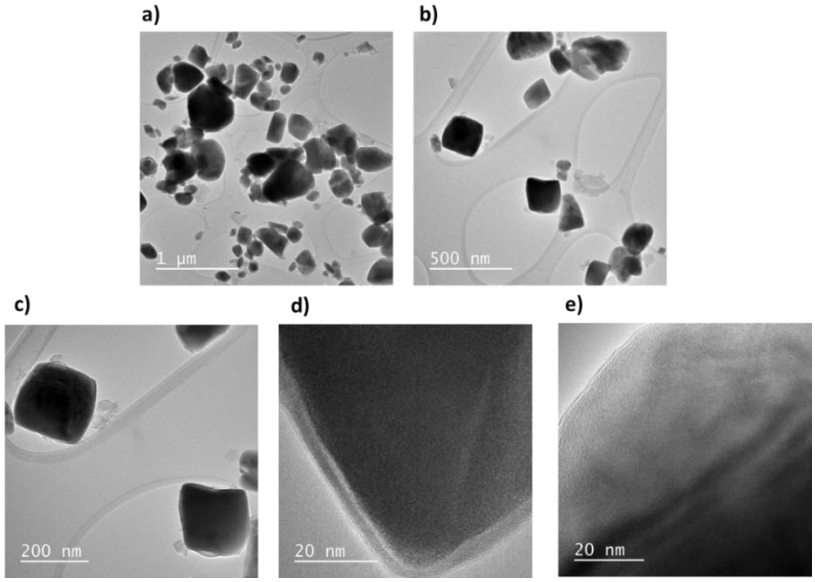

Figure 4.31 : TEM analyses images for ErB_4 which is leached with 6 mole HCl acid.

4.2 Characterization of Particulate Reinforced W1Ni Composite Materials

4.2.1 Powder characterization

99 wt% W and 1 wt% Ni was mechanically alloyed for 6 h. Also, crystallite size and lattice strain was measured as 7.725 nm and 2.2%, respectively. Figure 4.32 shows scanning electron microscope (SEM) images with different magnifications (20000, 40000, and 80000X). When particles were examined, particle shape was nearly mixed morphology. Higher magnification of SEM image as shown in Figure 4.32c for W1Ni particles ranging was between 200 and 300 nm.

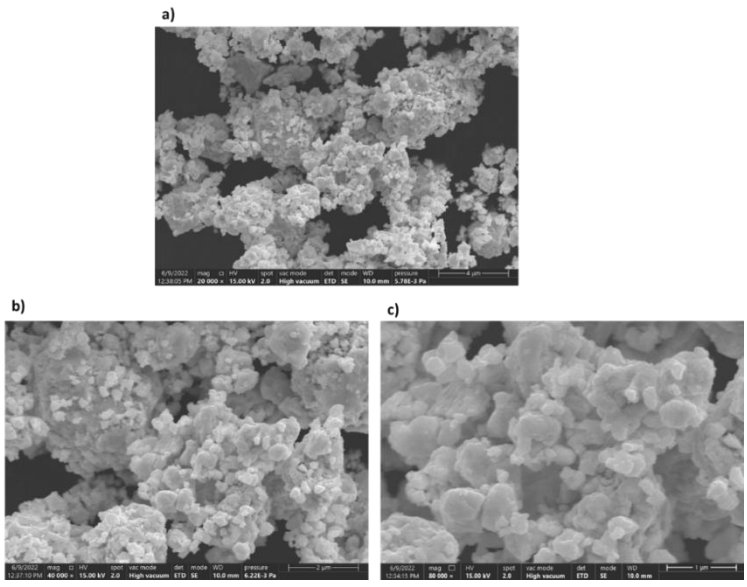

Figure 4.32 : SEM images of W1Ni powders at different magnifications a) 20000, b) 40000 and c) 80000X.

The general EDS analysis for Figure 4.33 was taken from the area in this image reveals the presence of W and Ni elements. Also, amount of W and Ni was measured 97% and 3% as atomic percentage.

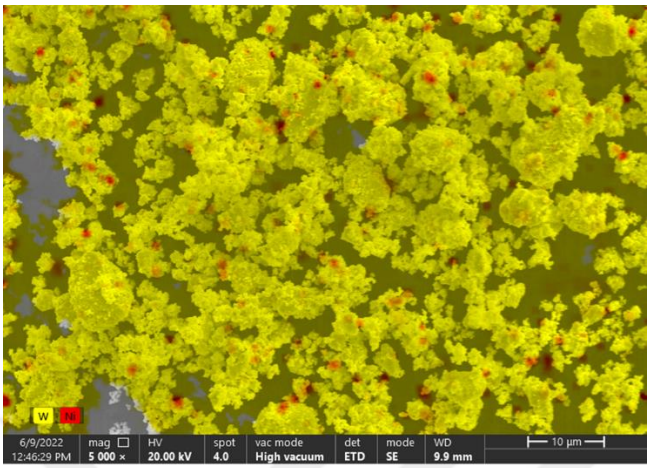

Points	W	Ni
Area	97	3

Figure 4.33 : SEM image and EDS result of W1Ni powders at 5000X magnification.

In addition, PSA graph as given in Figure 4.34 illustrates that the average particle size of the W1Ni was about 233.3 nm which is in the range observed in the SEM image in Figure 4.32c. Lognormal distribution type was observed for this graph. Also, density of pure W1Ni powders were measured as 16.8119±0.05 g/cm^3.

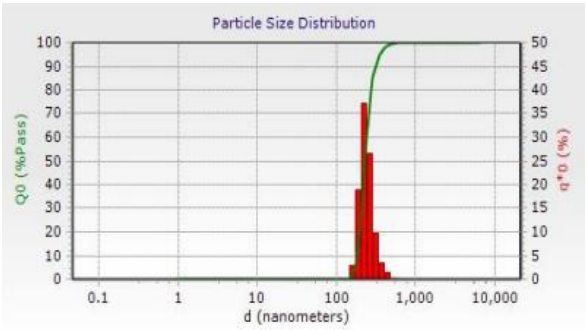

Figure 4.34 : Particle size analysis of W1Ni powder.

Producing of CeB_6 with mechanochemical synthesis powders [86] were added into W1Ni by using 6 h milling. After adding CeB_6 with different amounts (1, 2, 5 and 10 wt%), XRD analysis was done to powders 10-90º with 2 º. As XRD results, four main peaks were obtained as W (ICDD Card No: 00-004-0806, Bravais lattice: cubic, a = 0.316 nm). There was impurity as WC (ICDD Card No: 00-051-0939, Bravais lattice:

hexagonal, a = 0.291 nm and c = 0.284 nm). These results were shown in Figure 4.35. When amount of CeB_6 was increased, intensity of main peaks decreased.

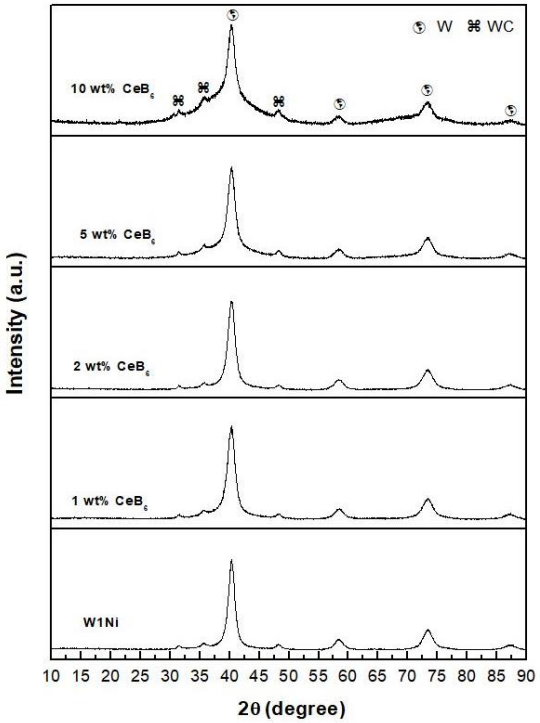

Figure 4.35 : XRD patterns of W1Ni composite powders reinforced with 1, 2, 5 and 10 wt% CeB_6.

Figure 4.36 shows the Rietveld analysis of powders. Amount of W and WC phases were nearly calculated as 88.2% and 11.8%, respectively. Lattice parameter of W and WC were calculated as a : 0.316 nm (cubic) and a : 0.291 nm, c : 0.284 (hexagonal), respectively. These values were matching with lattice parameter in PDF cards.

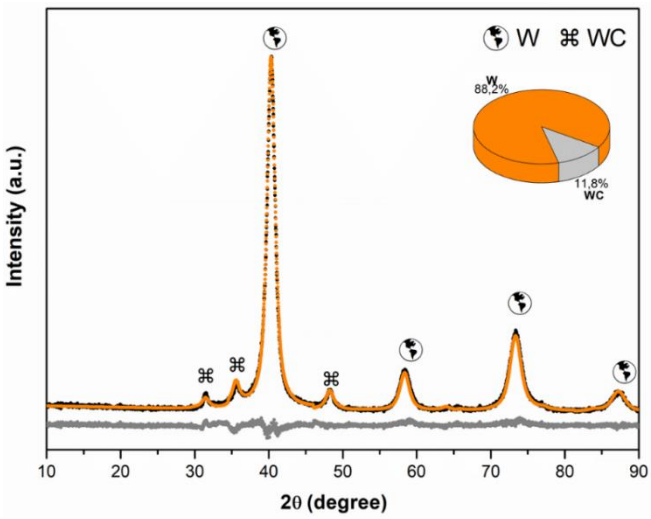

Figure 4.36 : Rietveld analysis of W1Ni powders; R_p : 4.27, R_{wp} : 5.53, GoF : 1.82, R_{Bragg} of W1Ni : 2.4.

Crystallite size and lattice strain of W1Ni with CeB_6 were measured by using TOPAS. Graph was given in Figure 4.37. While crystallite sizes were increasing, lattice strains were decreasing. The highest crystallite size and lowest lattice strain were obtained from W1Ni-2 wt% CeB_6.

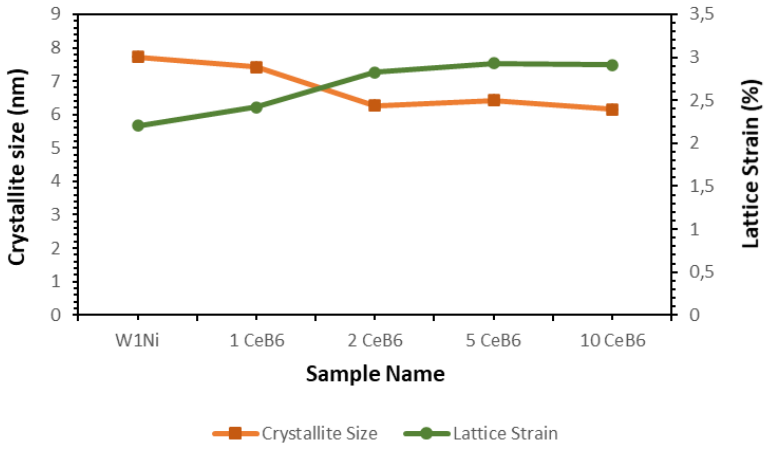

Figure 4.37 : Crystallite size and lattice strain of W1Ni composite powders reinforced with 1, 2, 5 and 10 wt% CeB_6.

Figure 4.38 shows scanning electron microscope images with different magnifications (20000, 40000 and 80000X). When particles were examined, particle shape was nearly mixed morphology. Higher magnification of SEM image as shown in Figure 4.38c for W1Ni-5 wt% CeB_6 particles ranging was between 80 and 120 nm.

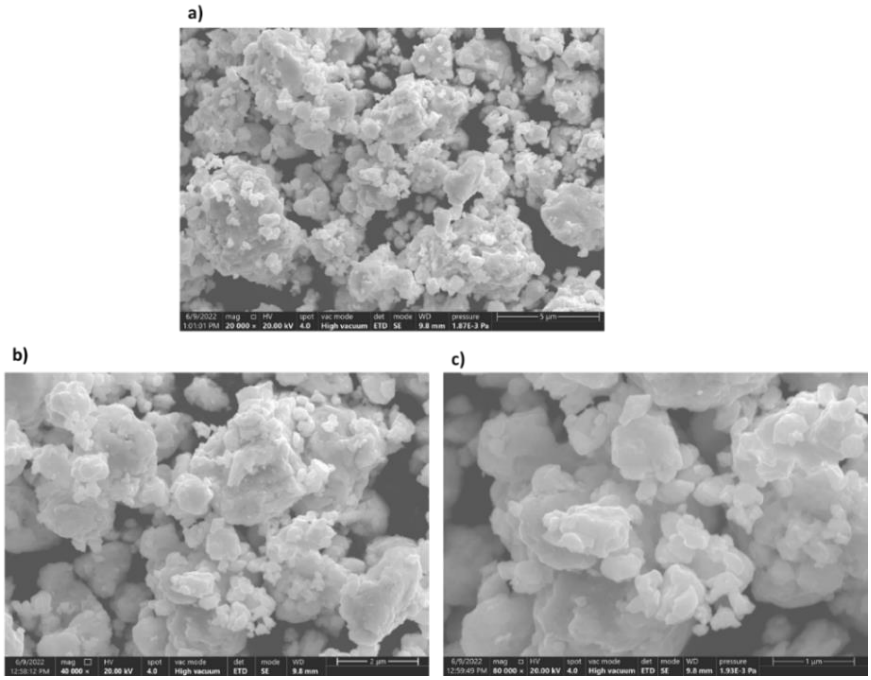

Figure 4.38 : SEM images of W1Ni-5 wt% CeB_6 powders for different magnifications a) 20000, b) 40000 and c) 80000X.

The general EDS analysis for Figure 4.39 was taken from the area in this image reveals the presence of W, Ni, Ce and B elements. Also, amount of W, Ni, Ce and B was measured 82.1, 3.6, 2.4 and 11.9% as atomic percentage, respectively.

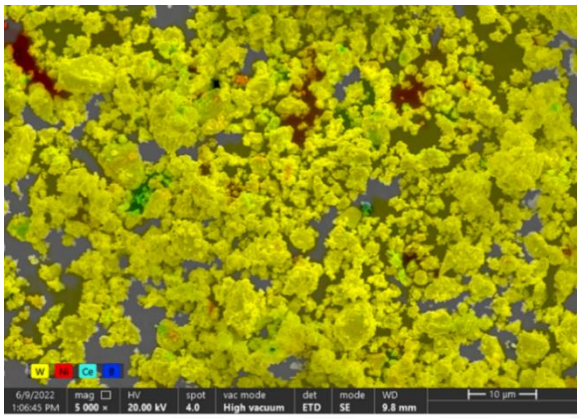

Points	W	Ni	B	Ce
Area	82.1	3.6	11.9	2.4

Figure 4.39 : SEM image and EDS result of W1Ni-5 wt% CeB_6 powders at x5000 magnification.

In addition, the PSA graphs that is given in Figure 4.40 illustrates that the average particle sizes of the W1Ni-1, 2, 5 and 10 wt% CeB_6 were nearly 119.9, 110, 106 and 76.1 nm, respectively. Particle size of W1Ni-5 wt% CeB_6 is in the range observed in the SEM image in Figure 4.38c. Lognormal distribution type was observed for this graph. Also, density of W1Ni-1, 2, 5 and 10 wt% CeB_6 powders were measured as 15.6884±0.009, 15.8724±0.007, 14.7592±0.005 and 13.1881±0.006 g/cm^3. Density of powders were decreasing with increasing amount of CeB_6.

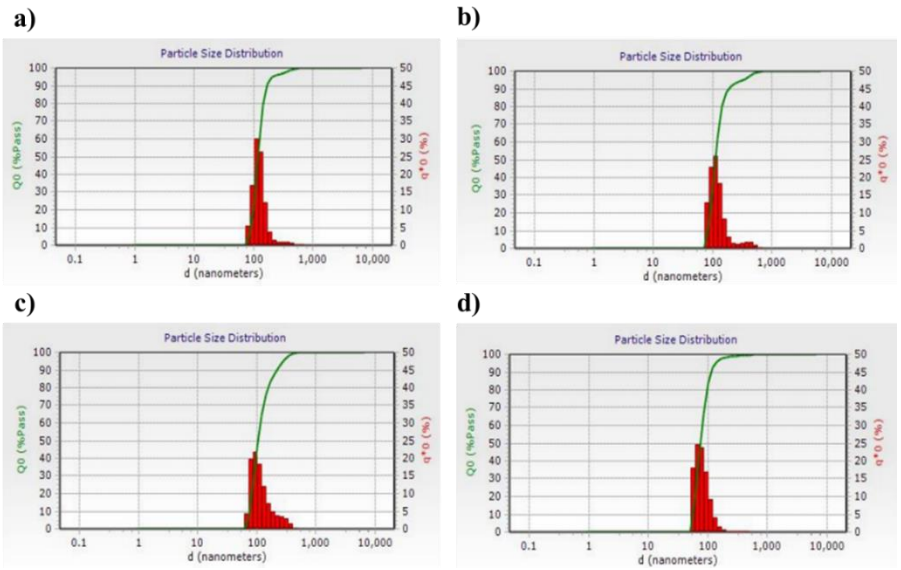

Figure 4.40 : Particle sizes of W1Ni-a) 1, b) 2, c) 5 and d) 10 wt% CeB_6 powders.

NdB_6 powders were produced with mechanochemical synthesis with 5 h and HCl leaching, and powders were added into W1Ni matrix. After adding NdB_6 with different amounts, XRD analysis was done to powders 10-90º with 2 º. As XRD results, four main peaks were obtained as W (ICDD Card No: 00-004-0806, Bravais lattice: cubic, a = 0.316 nm). There was impurity as WC (ICDD Card No: 00-051-0939, Bravais lattice: hexagonal, a = 0.291 nm and c = 0.284 nm). These results were shown in Figure 4.41. When amount of NdB_6 increased, intensity of main peaks decreased.

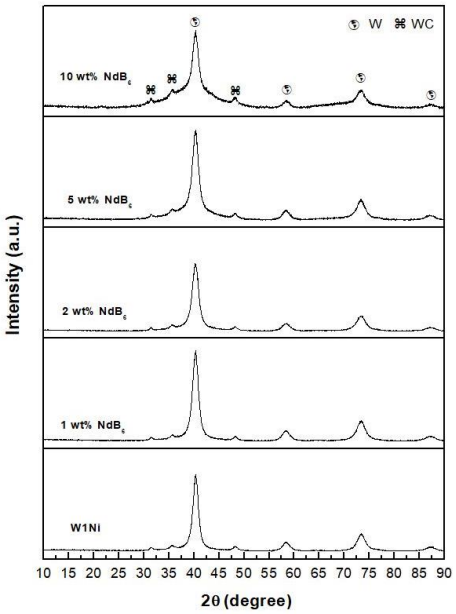

Figure 4.41 : XRD patterns of W1Ni composite powders reinforced with 1, 2, 5 and 10 wt% NdB_6.

Figure 4.42 shows that crystallite size and lattice strain of W1Ni with NdB_6 that were measured by using TOPAS. While crystallite sizes were increasing, lattice strains were decreasing. The highest crystallite size and lowest lattice strain were obtained from W1Ni-2 wt% NdB_6.

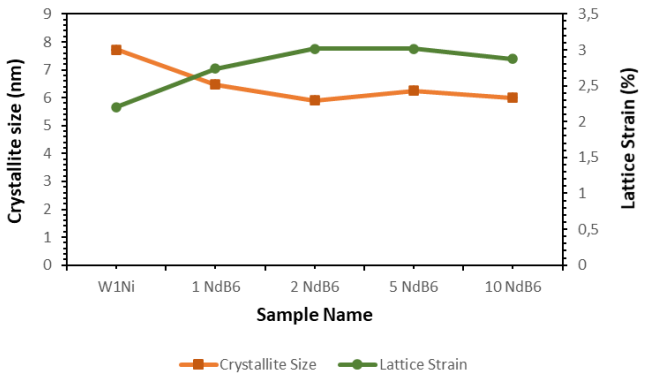

Figure 4.42 : Crystallite size and lattice strain of W1Ni composite powders reinforced with 1, 2, 5 and 10 wt% NdB_6.

Figure 4.43 shows scanning electron microscope images with different magnifications (20000, 40000 and 80000X). When particles were examined, particle shape was mixed morphology. Higher magnification of SEM image as shown in Figure 4.43c for W1Ni-5 wt% NdB_6 particles ranging was between 80 and 120 nm.

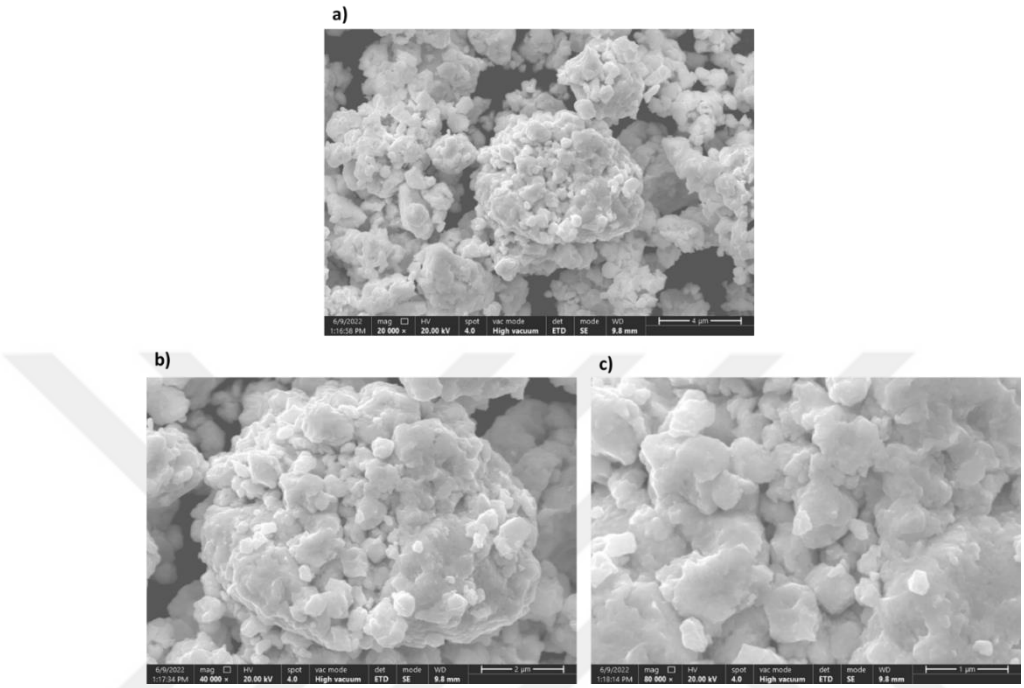

Figure 4.43 : SEM images of W1Ni-5 wt% NdB_6 powders for different magnifications a) 20000, b) 40000 and c) 80000X.

The general EDS analysis for Figure 4.44 was taken from the area in this image shows W, Ni, Nd and B elements. Also, amount of W, Ni, Nd and B was measured 83.9, 3.8, 2.3 and 10.0% as atomic percentage, respectively.

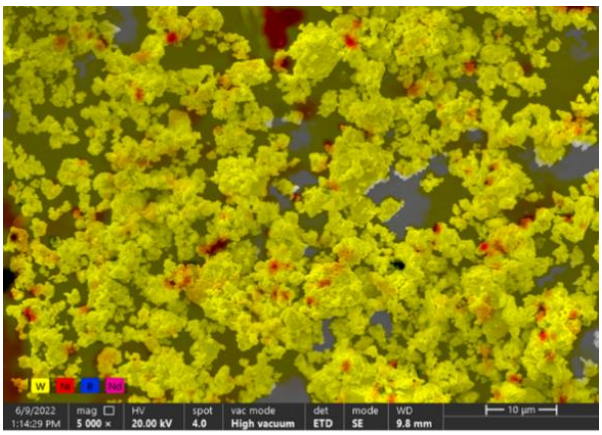

Points	W	Ni	B	Nd
Area	83.9	3.8	10.0	2.3

Figure 4.44 : SEM image and EDS result of W1Ni-5 wt% NdB_6 powders at 5000X magnification.

In addition, the PSA graphs for W1Ni-1, 2, 5 and 10 wt% NdB_6 as given in Figure 4.45 illustrate that the average particle sizes of the W1Ni-1, 2, 5 and 10 wt% NdB_6 were nearly 120.8, 111.9, 109.9 and 65.2 nm, respectively. Particle size of W1Ni-5 wt% NdB_6 is in the range observed in the SEM image in Figure 4.43c. Lognormal distribution type was observed for this graph. Also, density of W1Ni-1, 2, 5 and 10 wt% NdB_6 powders were measured as 16.1257±0.01, 15.6650±0.01, 14.7436±0.005 and 13.2312±0.006 g/cm^3. Density of powders were decreasing with increasing amount of NdB_6.

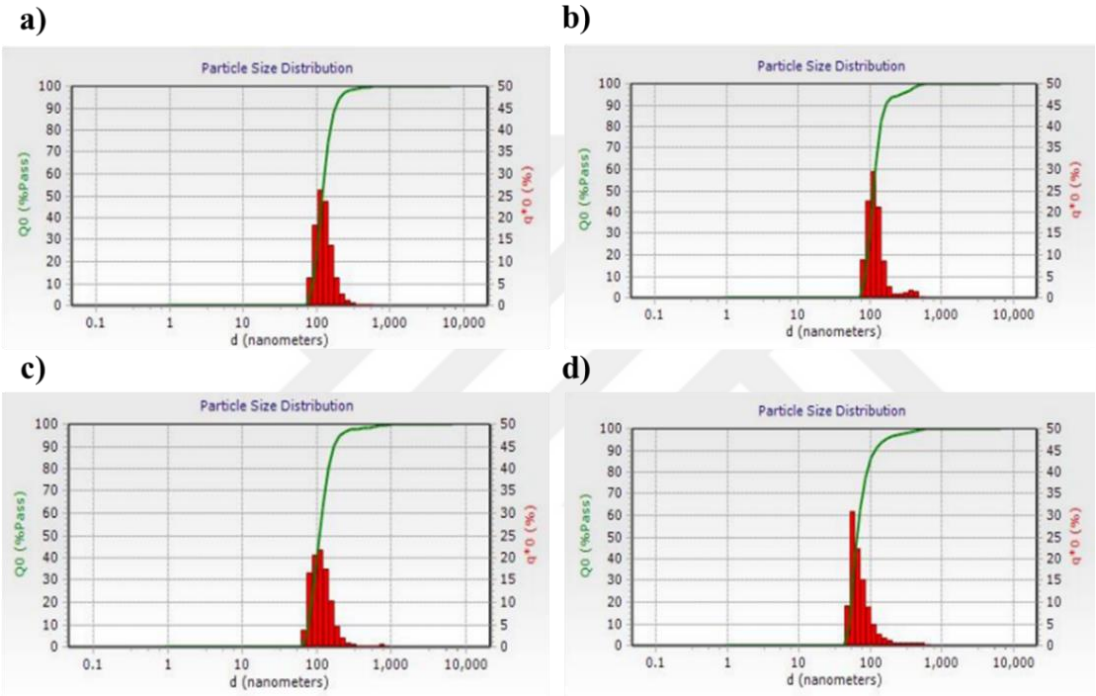

Figure 4.45 : Particle sizes of W1Ni-1, 2, 5 and 10 wt% NdB_6 powders.

ErB_4 powders were produced with mechanochemical synthesis with 5 h and 6 M HCl leaching. After adding ErB_4 with different amounts, XRD analysis was done to powders at 10-90º range with 2 º. As XRD results, four main peaks were obtained as W (ICDD Card No: 00-004-0806, Bravais lattice: cubic, a = 0.316 nm). There was impurity as WC (ICDD Card No: 00-051-0939, Bravais lattice: hexagonal, a = 0.291 nm and c = 0.284 nm). These results were shown in Figure 4.46. When amount of ErB_4 was increased, intensity of main peaks decreased.

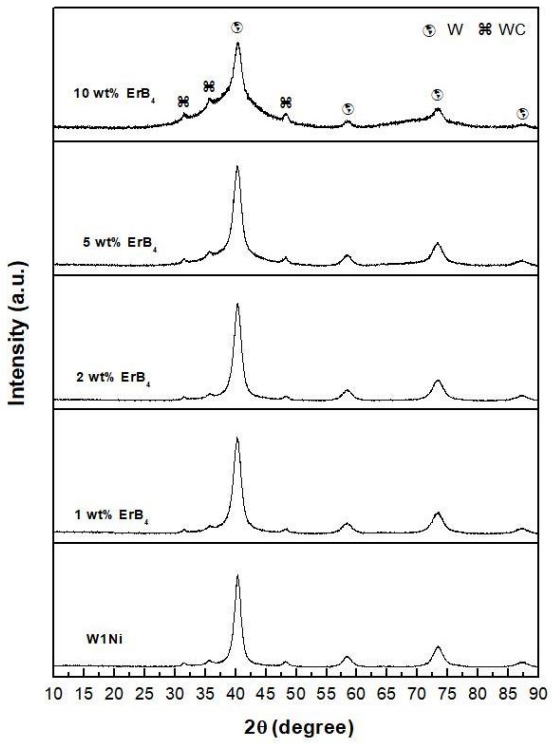

Figure 4.46 : XRD patterns of W1Ni composites reinforced with 1, 2, 5 and 10 wt% ErB_4 with pressureless sintering.

Crystallite size and lattice strain of W1Ni with ErB_4 were measured by using TOPAS. Graph was given in Figure 4.47. While crystallite sizes were increasing, lattice strains were decreasing. The highest crystallite size and lowest lattice strain were obtained from W1Ni-2 wt% ErB_4.

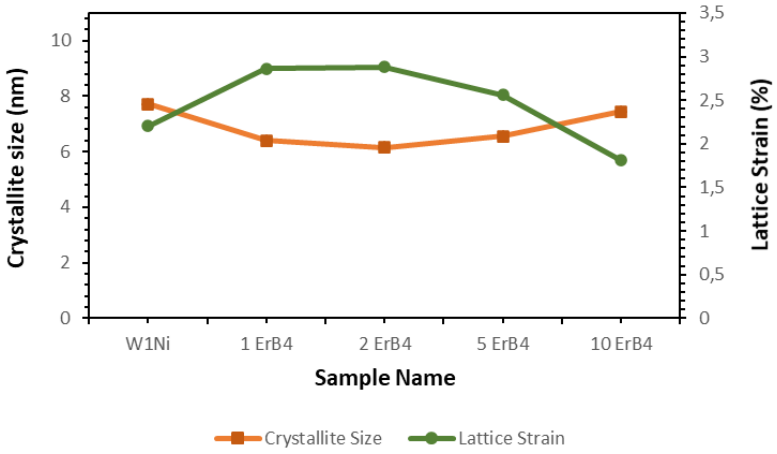

Figure 4.47 : Crystallite size and lattice strain of W1Ni composite powders reinforced with 1, 2, 5 and 10 wt% ErB_4.

Figure 4.48 shows scanning electron microscope images with different magnifications (20000, 40000 and 80000X). When particles were examined, particle shape was mixed

morphology. Higher magnification of SEM image as shown in Figure 4.48c for W1Ni-5 wt% ErB_4 particles ranging was between 80 and 120 nm.

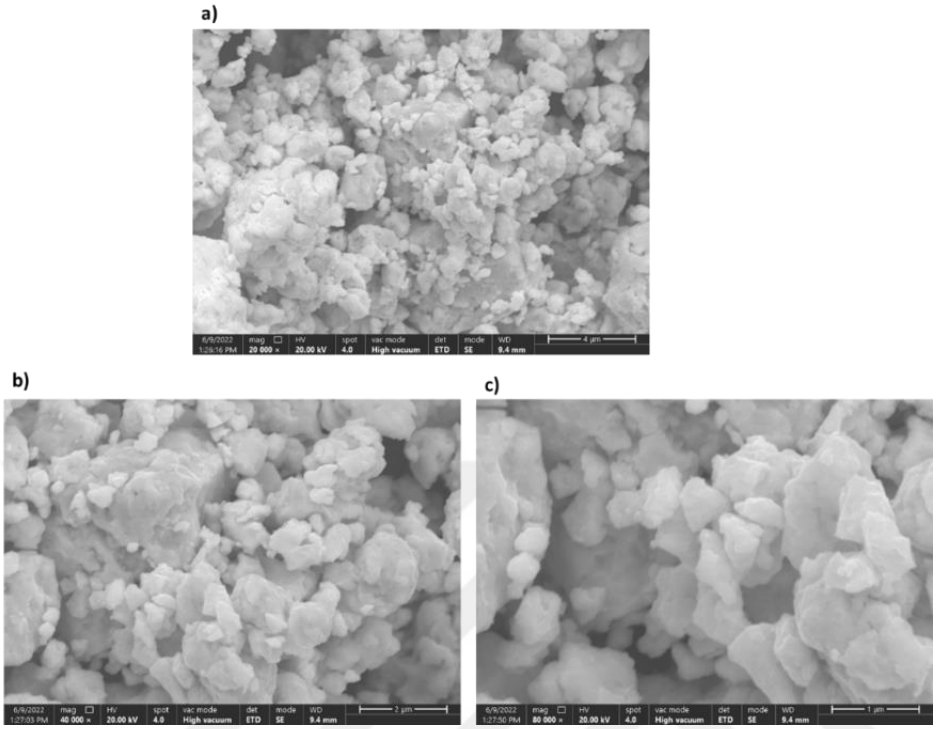

Figure 4.48 : SEM images of W1Ni-5 wt% ErB_4 powders for different magnifications a) 20000, b) 40000 and c) 80000X.

W, Ni, Er and B elements were observed at the general EDS analysis for Figure 4.49 was taken from the area in this image. Also, amount of W, Ni, Er, and B was measured 85.2, 4.0, 5.1 and 5.7% as atomic percentage, respectively.

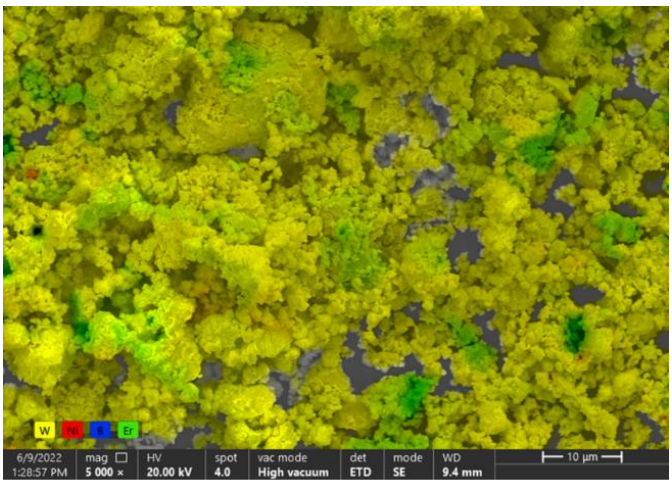

Points	W	Ni	B	Er
Area	85.2	4.0	5.7	5.1

Figure 4.49 : SEM image and EDS result of W1Ni-5 wt% ErB_4 powders at 5000X magnification.

In addition, the PSA graphs for W1Ni-1, 2, 5 and 10 ErB_4 as given in Figure 4.50 illustrate that the average particle size of the W1Ni-1, 2, 5 and 10 wt% ErB_4 were 121, 113,2 104.7 and 76 nm, respectively. Particle size of W1Ni-5 wt% ErB_4 is in the range observed in the SEM image in Figure 4.48c. Lognormal distribution type was observed for this graph. Also, density of W1Ni-1, 2, 5 and 10 wt% ErB_4 powders were measured as 16.0133±0.008, 16.0530±0.02, 15.4666±0.01 and 14.5964±0.01 g/cm^3. Density of powders were decreasing with increasing amount of ErB_4.

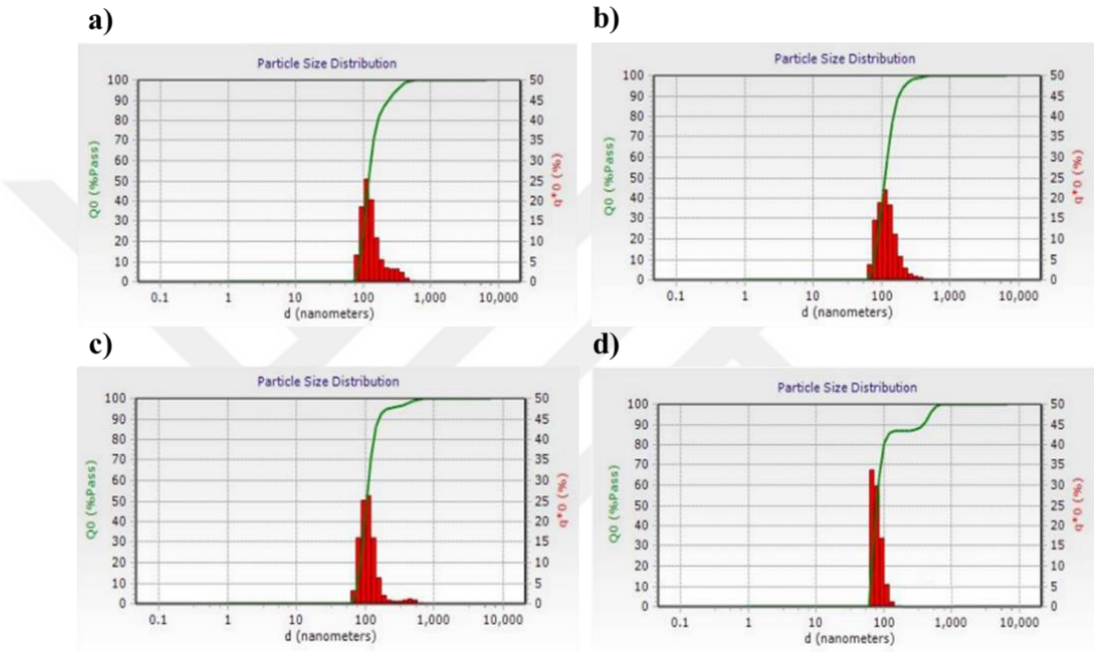

Figure 4.50 : Particle sizes of W1Ni-1, 2, 5 and 10 wt% ErB_4 powders.

4.2.2 Characterization of Activated Sintered Samples

4.2.2.1 Characterization of pressureless sintered W1Ni composites

Firstly, CeB_6 powders were produced with mechanochemical synthesis with 5 h and HCl leaching. Then, 99 wt% W and 1 wt% Ni were mechanically alloyed for 6 h milling. After adding CeB_6 powders with different amounts (1, 2, 5 and 10 wt%) to W1Ni with 6 h milling, hydraulic pressing was applied to powder for 480 MPa (480×10^6 N/m^2) and 1 min. Then, CIP was applied to bulk samples for 390 MPa and 1 min. Finally, pressureless sintered was used for all samples at 1400°C for 1 h. XRD analysis was done to pressureless sintered samples 10-90º with 2º. As XRD results, four main peaks were obtained as W (ICDD Card No: 00-004-0806, Bravais lattice cubic, a = 0.316 nm). There was one phase which is small intensity to as WO_3 (ICDD Card No: 00-005-0364, Bravais lattice: monoclinic, a = 0.729 nm, b= 0.752 and c =

0.384 nm). When amount of CeB_6 was increased, intensity of main peaks decreased. After 5 wt% CeB_6 adding, W_2B (ICDD Card No: 00-025-0990, Bravais lattice: tetragonal, a = 0.557 nm and c = 0.474 nm) phase was observed in structure. While main phase was W, W_2B started to be main phase because of high amount of boron. These results were shown in Figure 4.51.

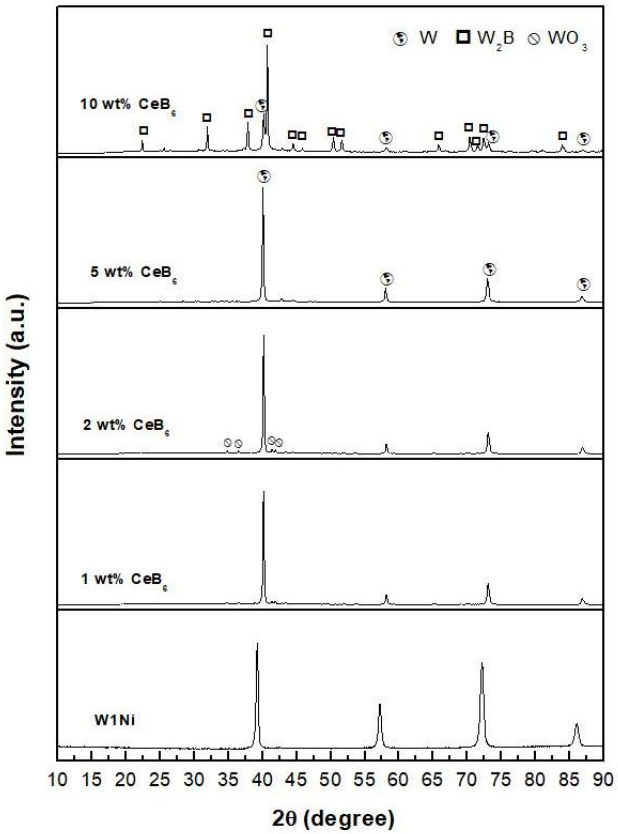

Figure 4.51 : XRD patterns of W1Ni composites reinforced with 1, 2, 5 and 10 wt% CeB_6 with pressureless sintering.

SEM images of W1Ni and reinforced with 1, 2, 5 and 10 wt% CeB_6 particulates were given in Figure 4.52. In the images, dark areas were observed after adding CeB_6 particulates. These dark areas were increasing with increasing amount of CeB_6. W was observed as main phase. W1Ni-10 wt% CeB_6 sample had different structure as other samples because of W_2B phases.

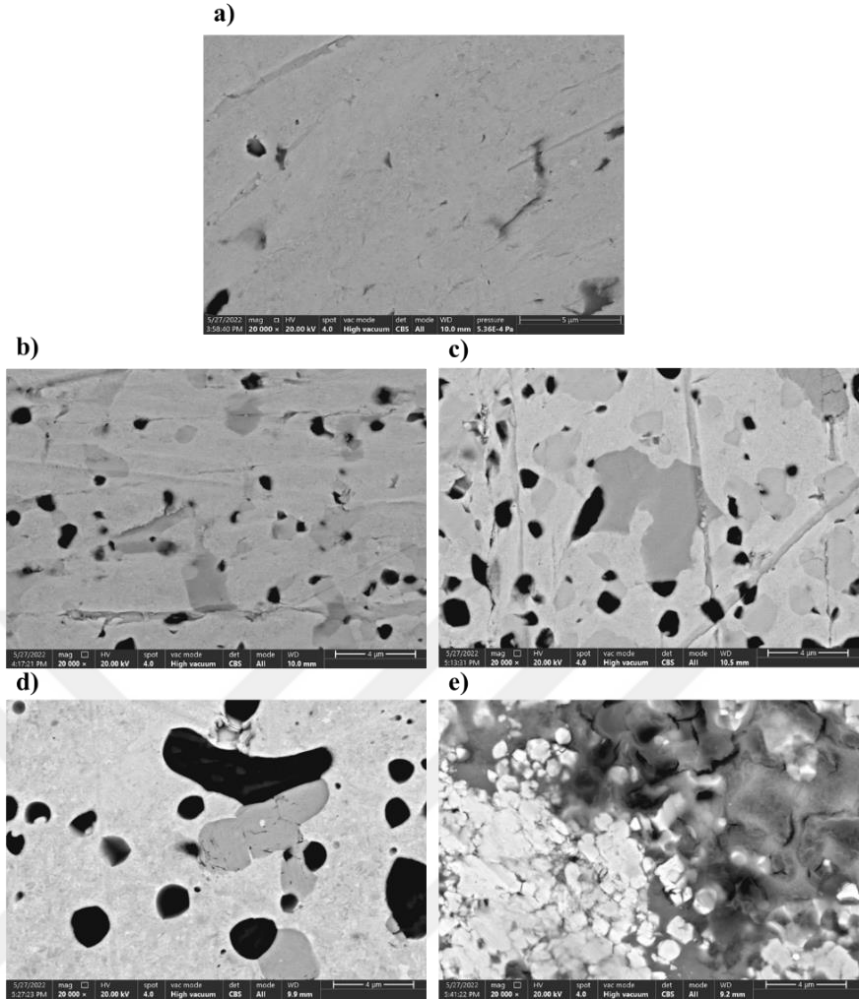

Figure 4.52 : SEM images of a) W1Ni, W1Ni-b) 1, c) 2, c) 5 and d) 10 wt% CeB_6 at 20000X magnification.

General EDS results for W1Ni and W1Ni-1, 2, 5 and 10 wt% CeB_6 samples were given in Table 4.1. As results of EDS, amount of Ce was increasing and other elements were nearly stable.

Table 4.1 : General EDS for W1Ni and W1Ni-1, 2, 5 and 10 wt% CeB_6 sintered samples.

Samples	W	Ni	Ce	B
W1Ni	97.3	2.7	-	-
W1Ni - 1 CeB_6	86.4	5.2	0.5	7.9
W1Ni - 2 CeB_6	84.3	7.3	1.7	6.6
W1Ni - 5 CeB_6	85.1	5.8	1.8	7.2
W1Ni - 10 CeB_6	74.3	4.3	13.1	8.3

Colorful EDS image and point EDS results for W1Ni were given in Figure 4.53. In this picture, dark areas contained high amount of Ni. When EDS results were

examined, amount of W and Ni was observed as 96.7%, 3.3% and 53.1%, 46.9% for point 1 and 2, respectively.

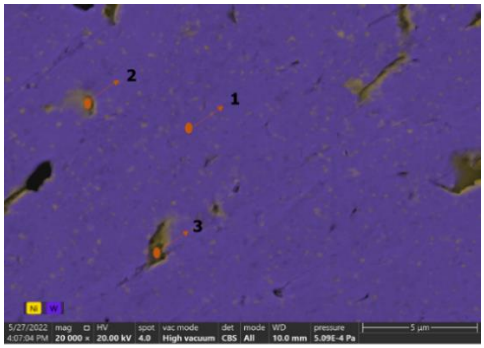

Points	W	Ni
1	96.7	3.3
2	53.1	46.9
3	38.8	61.2

Figure 4.53 : Colorful EDS image and point EDS results for W1Ni.

Figure 4.54 shows that colorful EDS image and point EDS results for W1Ni-1, 2, 5 and 10 wt% CeB_6 samples. All grey areas include high nickel amount with W and a small amount of B. Cerium was not observed for this area. For white area, W was main phases nearly 90% with small amounts of B and Ni. Ce was main element for all dark areas. These dark areas were growing with increasing amount of Ce.

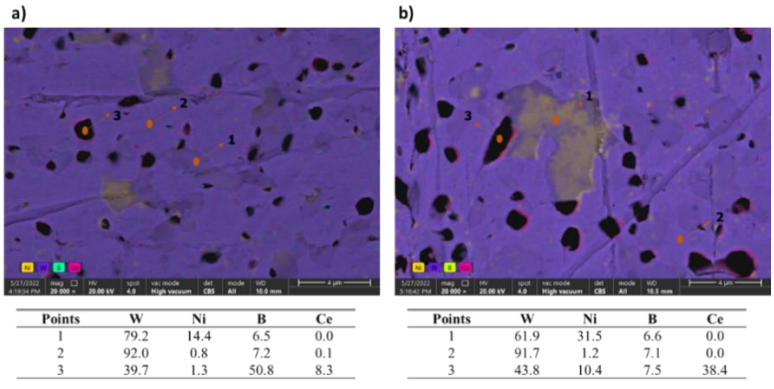

Points	W	Ni	B	Ce
1	79.2	14.4	6.5	0.0
2	92.0	0.8	7.2	0.1
3	39.7	1.3	50.8	8.3

Points	W	Ni	B	Ce
1	61.9	31.5	6.6	0.0
2	91.7	1.2	7.1	0.0
3	43.8	10.4	7.5	38.4

Points	W	Ni	B	Ce
1	74.0	18.0	8.0	0.0
2	92.0	0.8	7.2	0.0
3	29.0	4.1	8.0	58.9

Points	W	Ni	B	Ce
1	87.5	3.4	7.9	1.2
2	96.3	2.8	0.0	0.9
3	81.3	3.3	0.0	15.4

Figure 4.54 : Colorful EDS image and point EDS results for W1Ni-a) 1, b) 2, c) 5 and d) 10 wt% CeB_6.

NdB_6 powders were produced with mechanochemical synthesis with 5 h and HCl leaching. Then, W1Ni which is mechanically alloyed for 6 h was mixed with NdB_6 powders with different amounts (1, 2, 5 and 10 wt%) 6 h milling. Hydraulic pressing was applied to powder for 480 MPa (480×10^6 N/m^2) and 1 min. Then, CIP was applied to bulk samples for 390 MPa and 1 min. Finally, pressureless sintered was used for all samples at 1400°C for 1 h. Also, XRD analysis was done to pressureless sintered samples at 10-90º range with 2 º increment. As XRD results, four main peaks were obtained as W (ICDD Card No: 00-004-0806, Bravais lattice cubic, a = 0.316 nm). There was one phase which is small intensity to as WO_3 (ICDD Card No: 00-005-0364, Bravais lattice: monoclinic, a = 0.729 nm, b= 0.752 and c = 0.384 nm). When amount of NdB_6 was increased, intensity of main peaks decreased. After 5 wt% NdB_6 adding, W_2B (ICDD Card No: 00-025-0990, Bravais lattice: tetragonal, a = 0.557 nm and c = 0.474 nm) phase was observed in structure. While main phase was W, W_2B started to be main phase because of more boron. These results were shown in Figure 4.55.

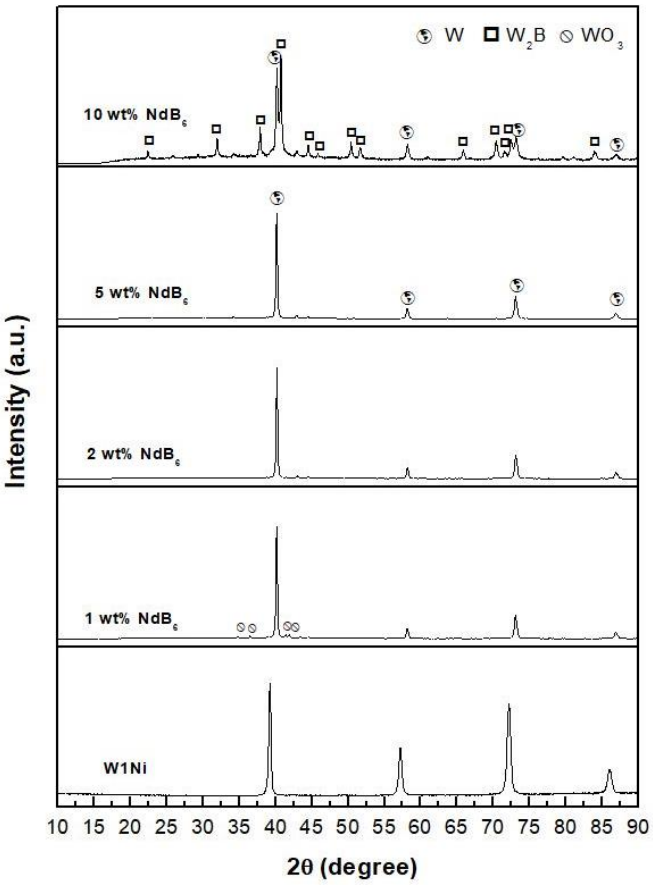

Figure 4.55 : XRD patterns of W1Ni composites reinforced with 1, 2, 5 and 10 wt% NdB_6 with pressureless sintering.

SEM images of W1Ni and reinforced with 1, 2, 5 and 10 wt% NdB_6 particulates were given in Figure 4.56. As images, dark areas were observed after adding NdB_6 particulates. Also, W was observed as main phase. W1Ni-10 wt% NdB_6 sample had different structure as other samples because of W_2B phases.

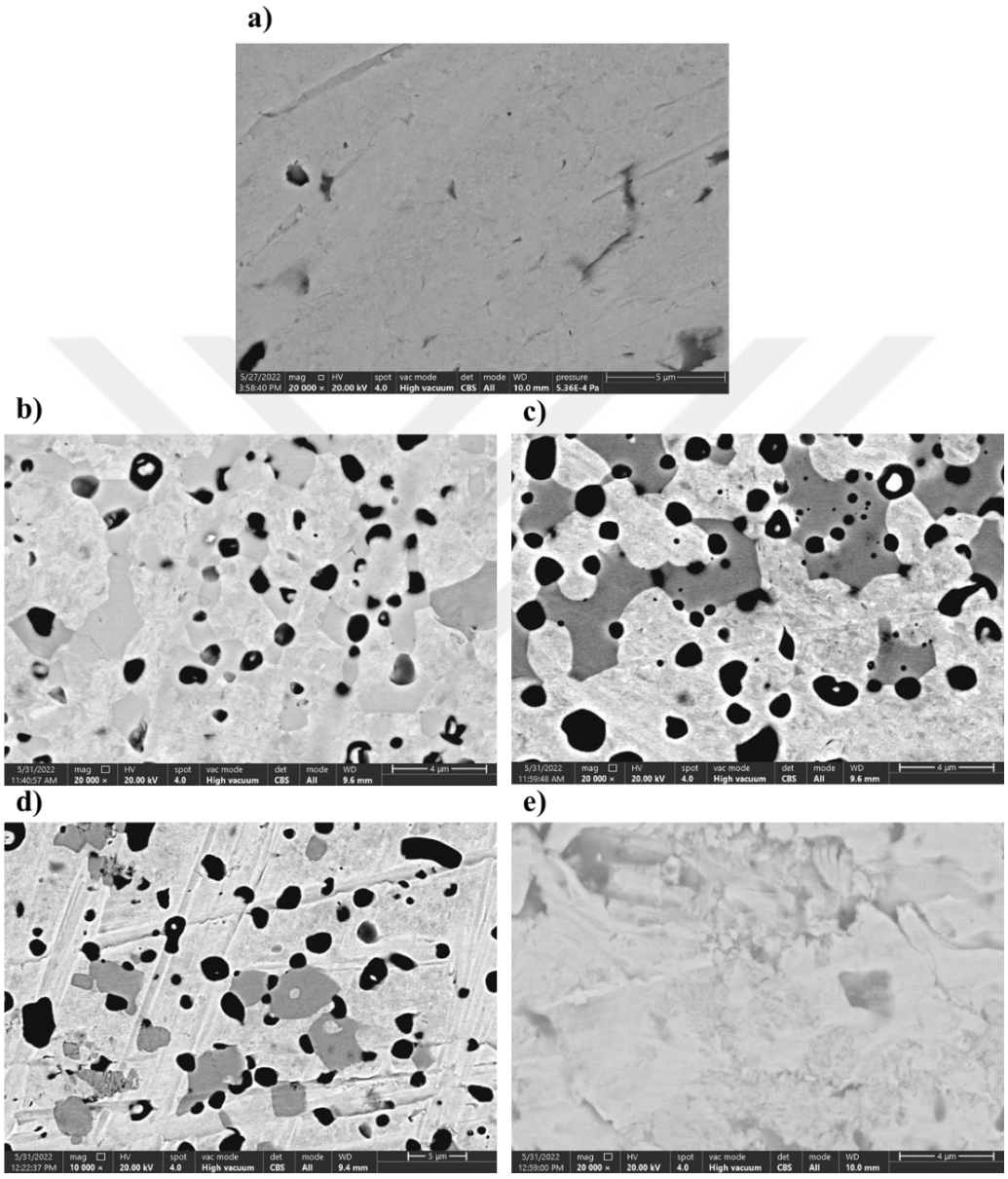

Figure 4.56 : SEM images of a) W1Ni, W1Ni-b) 1, c) 2, d) 5 and e) 10 wt% NdB_6 at 20000X magnification.

General EDS results for W1Ni and 1, 2, 5 and 10 wt% NdB_6 samples were given in Table 4.2. As results of EDS, amount of Nd was increasing and other elements were nearly stable.

Table 4.2 : General EDS for W1Ni and W1Ni-1, 2, 5 and 10 wt% NdB_6 sintered samples.

Samples	W	Ni	Nd	B
W1Ni	97.3	2.7	-	-
W1Ni - 1 NdB_6	89.6	3.4	0.8	6.1
W1Ni - 2 NdB_6	80.5	12.1	1.3	6.0
W1Ni - 5 NdB_6	83.6	7.3	2.7	6.4
W1Ni - 10 NdB_6	77.3	4.3	3.0	15.4

Figure 4.57 illustrates colorful EDS image and point EDS results for W1Ni-1, 2, 5 and 10 wt% NdB_6 samples. All grey areas include high nickel amount with W and a little B. Neodymium was not almost observed for this area. For white area, W was main phases nearly 90% with small amount B and Ni. Nd was main element for all dark areas. These dark areas were growing with increasing amount of Nd.

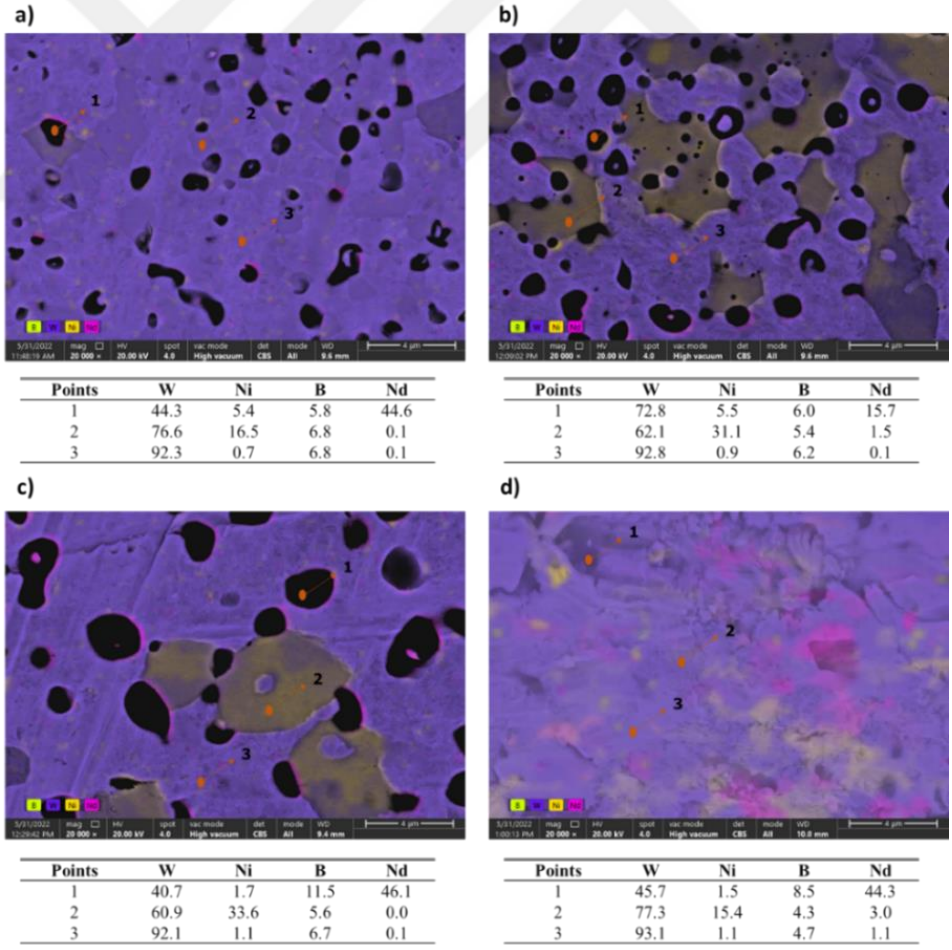

Points	W	Ni	B	Nd
1	44.3	5.4	5.8	44.6
2	76.6	16.5	6.8	0.1
3	92.3	0.7	6.8	0.1

Points	W	Ni	B	Nd
1	72.8	5.5	6.0	15.7
2	62.1	31.1	5.4	1.5
3	92.8	0.9	6.2	0.1

Points	W	Ni	B	Nd
1	40.7	1.7	11.5	46.1
2	60.9	33.6	5.6	0.0
3	92.1	1.1	6.7	0.1

Points	W	Ni	B	Nd
1	45.7	1.5	8.5	44.3
2	77.3	15.4	4.3	3.0
3	93.1	1.1	4.7	1.1

Figure 4.57 : Colorful EDS image and point EDS results for W1Ni-a) 1, b) 2 c) 5 and c) 10 wt% NdB_6.

ErB_4 powders were produced with mechanochemical synthesis with 5 h and 6 M HCl leaching. Then, W1Ni which is mechanically alloyed for 6 h was mixed with ErB_4 powders with different amounts (1, 2, 5 and 10 wt%) 6 h milling. Hydraulic pressing was applied to powder for 480 MPa (480×10^6 N/m^2) and 1 min. Then, CIP was applied to bulk samples for 390 MPa and 1 min. Finally, pressureless sintered was used for all samples at 1400°C for 1 h. Also, XRD analysis was done to powders pressureless sintered samples 10-90º with 2 º. As XRD results, four main peaks were obtained as W (ICDD Card No: 00-004-0806, Bravais lattice cubic, a = 0.316 nm). There was one phase, WO_3 (ICDD Card No: 00-005-0364, Bravais lattice: monoclinic, a = 0.729 nm, b= 0.752 and c = 0.384 nm), which is in small intensity. When amount of ErB_4 was increased, intensity of main peaks decreased. These results were shown in Figure 4.58.

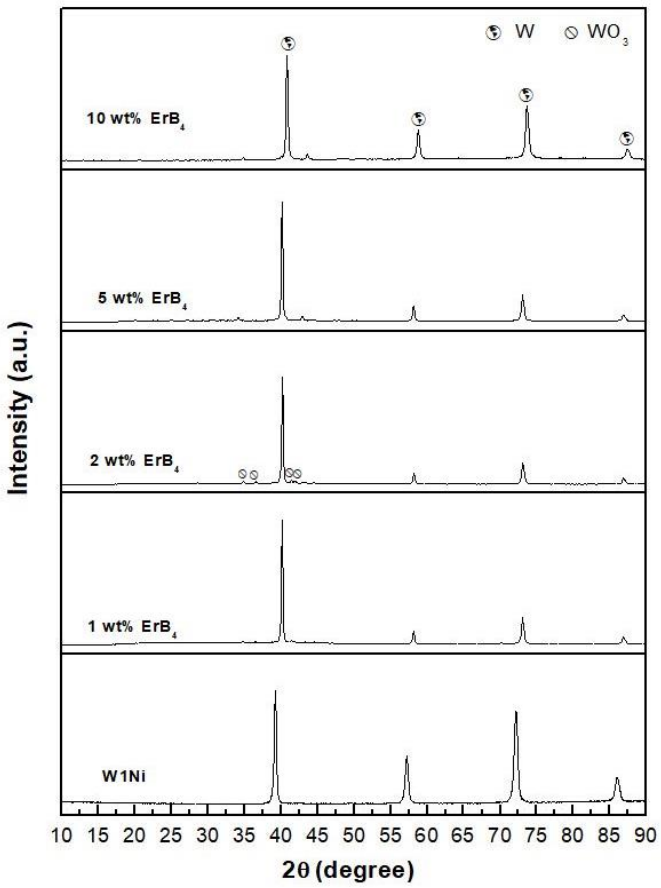

Figure 4.58 : XRD patterns of W1Ni composites reinforced with 1, 2, 5 and 10 wt% ErB_4 with pressureless sintering.

SEM images of W1Ni and reinforced with 1, 2, 5 and 10 wt% ErB_4 particulates were given in Figure 4.59. As images, dark areas were observed after adding ErB_4 particulates. Also, W was observed as main phase.

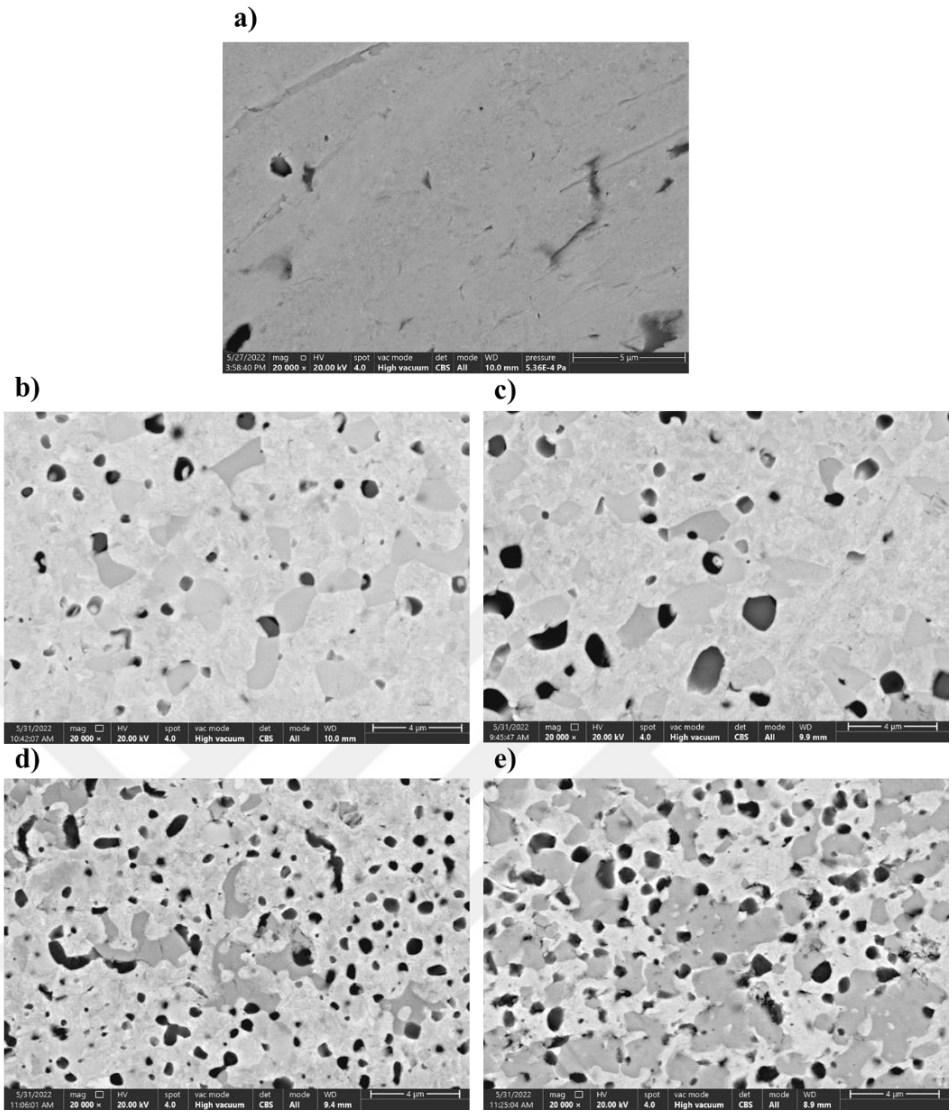

Figure 4.59 : SEM images of a) W1Ni, W1Ni-b) 1, c) 2, d) 5 and e) 10 wt% ErB_4 at 20000X magnification.

General EDS results for W1Ni and W1Ni-1, 2, 5 and 10 wt% ErB_4 samples were given in Table 4.3. As results of EDS, amount of Er was increasing and other elements were nearly stable.

Table 4.3 : General EDS for W1Ni and W1Ni-1, 2, 5 and 10 wt% ErB_4 sintered samples.

Samples	W	Ni	Er	B
W1Ni	97.3	2.7	-	-
W1Ni - 1 ErB_4	86.2	3.3	3.6	6.9
W1Ni - 2 ErB_4	88.3	2.6	3.3	5.8
W1Ni - 5 ErB_4	86.2	1.6	4.5	7.6
W1Ni - 10 ErB_4	76.0	8.1	8.3	7.6

Colorful EDS image and point EDS results for W1Ni-1, 2, 5 and 10 wt% ErB_4 samples were given in Figure 4.60. Generally, W was high amount for all areas. All grey areas include high nickel amount with W, Er and B. For white area, W was main phases nearly 90% with small amount B and Ni. Er was main element for all dark areas. These dark areas were getting higher with increasing amount of Er.

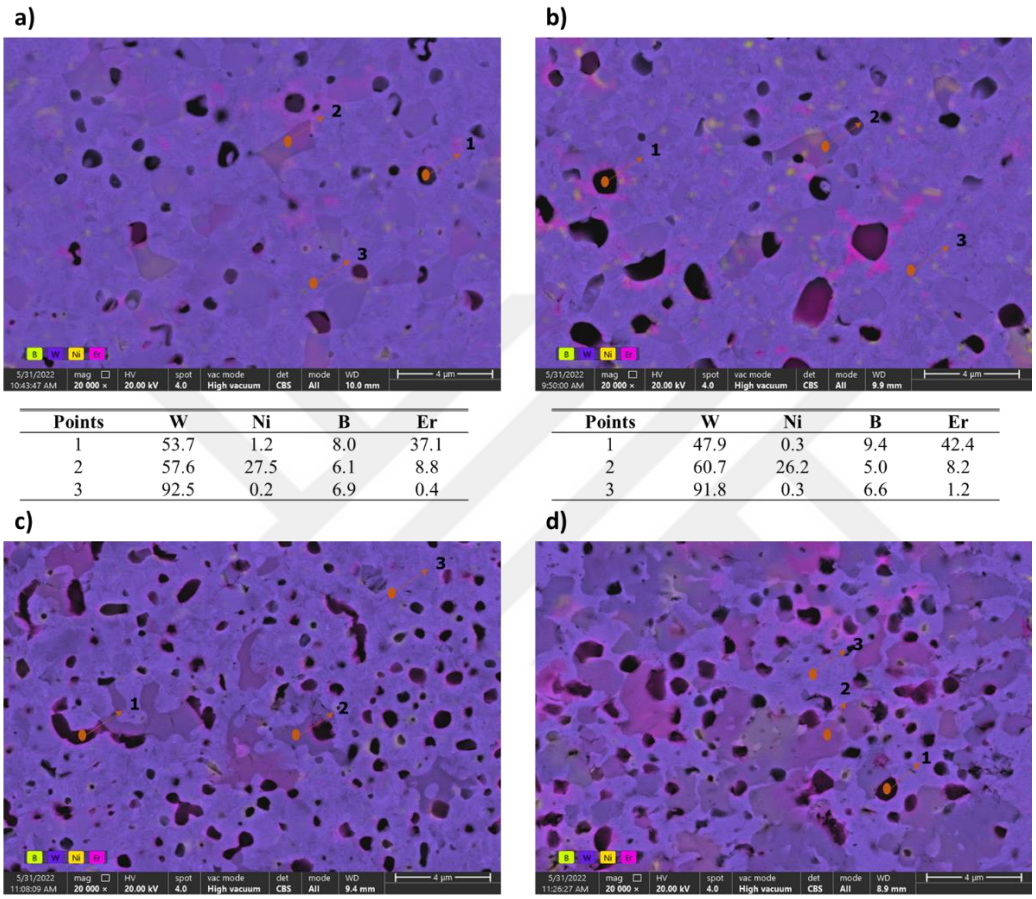

Points	W	Ni	B	Er
1	53.7	1.2	8.0	37.1
2	57.6	27.5	6.1	8.8
3	92.5	0.2	6.9	0.4

Points	W	Ni	B	Er
1	47.9	0.3	9.4	42.4
2	60.7	26.2	5.0	8.2
3	91.8	0.3	6.6	1.2

Points	W	Ni	B	Er
1	54.2	0.0	7.4	38.4
2	71.1	13.8	7.6	7.5
3	93.2	0.2	6.1	0.5

Points	W	Ni	B	Er
1	39.7	3.1	6.8	50.4
2	68.1	18.4	7.1	6.5
3	92.3	1.1	5.8	0.7

Figure 4.60 : Colorful EDS image and point EDS results for W1Ni-a) 1, b) 2, c) 5 and d) 10 wt% ErB_4.

Theoretical, Archimedes' and relative densities of samples were given in the Table 4.4. As given results, when boride particulates added into W1Ni based composite, relative densities for all samples were decreased. W with 1 wt% Ni mechanically alloyed for 6 h, had the highest relative density as 95.47%. Then, with adding 1 wt% CeB_6 gave higher relative density (92.64%) than 2, 5 and 10 wt% CeB_6. Also, density of 1 wt% NdB_6 sample was measured higher density (97.75%) than 2, 5 and 10 wt%

NdB_6. Finally, 1 wt% ErB_4 had higher relative density (92.12%) than other adding ErB_4 particulates.

Table 4.4 : Density results of pressureless sintered samples.

Samples	Theoretical Density (g/cm^3)	Archimedes' Density (g/cm^3)	Relative Density (%)
W1Ni	19.23	18.36	95.47
W1Ni - 1 CeB_6	18.52	17.15	92.64
W1Ni - 2 CeB_6	17.86	16.45	92.11
W1Ni - 5 CeB_6	16.16	14.74	91.22
W1Ni - 10 CeB_6	13.99	12.38	88.47
W1Ni - 1 NdB_6	18.52	18.10	97.75
W1Ni - 2 NdB_6	17.86	16.89	94.59
W1Ni - 5 NdB_6	16.16	14.85	91.91
W1Ni - 10 NdB_6	13.99	11.83	84.55
W1Ni - 1 ErB_4	18.79	17.31	92.12
W1Ni - 2 ErB_4	18.37	16.79	91.38
W1Ni - 5 ErB_4	17.23	15.47	89.80
W1Ni - 10 ErB_4	15.66	13.08	83.52

Microhardness value of pressureless sintered samples were given in Figure 4.61. Also, microhardness of W1Ni-10 wt% CeB_6, NdB_6 were not measured because of occuring different phases so that, microhardness values were shown variation. For all the samples, 2 wt% particulate reinforced W1Ni base composites were given the highest microhardness value. For 2 wt% CeB_6, NdB_6 and ErB_4 particulate reinforced W1Ni composites, microhardness values were measured as 6.79, 6.36 and 6.53 GPa, relatively. After adding 2 wt% reinforcing particulates, all microhardness values decreased.

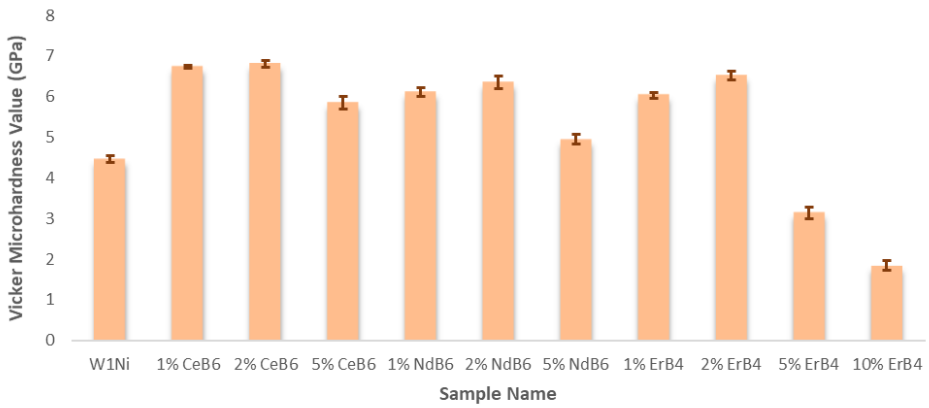

Figure 4.61 : Microhardness values of pressureless sintered samples.

Microhardness traces for W1Ni and W1Ni-1 wt% CeB_6, 2 wt% NdB_6 and 2 wt% ErB_4 were given in Figure 4.62. W1Ni showed lower hardness value than others, so that microhardness indentation was bigger than others.

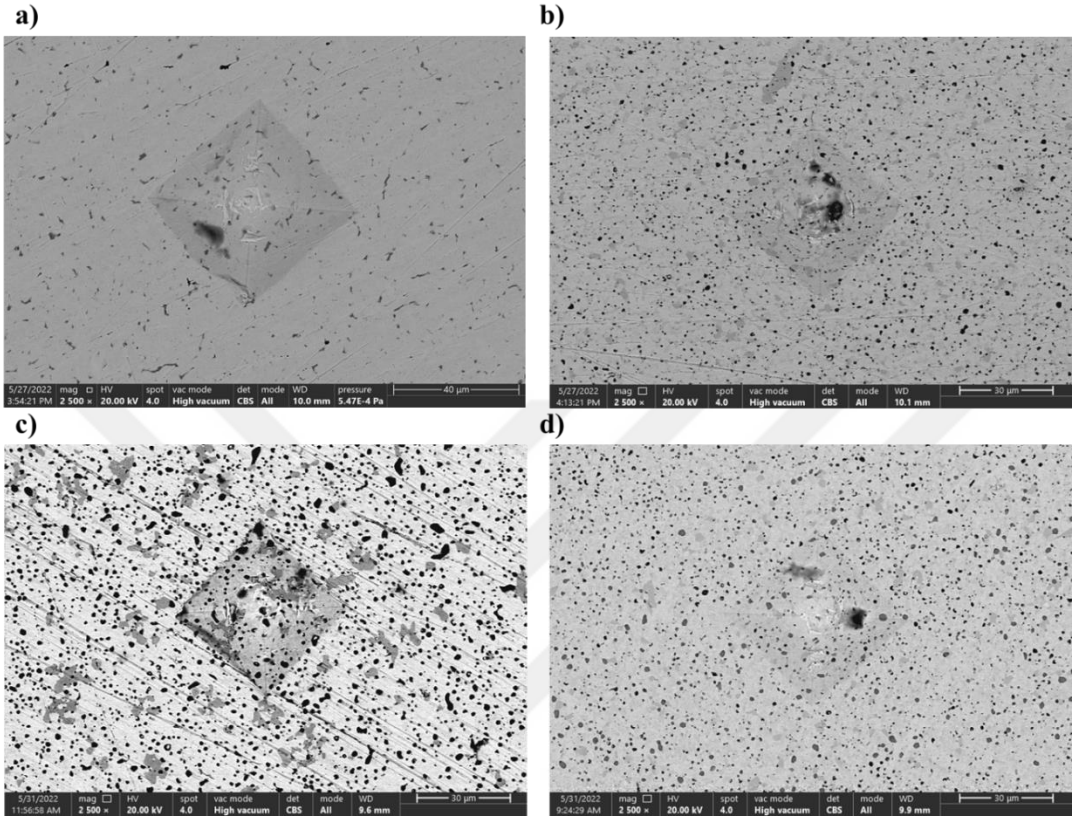

Figure 4.62 : Microhardness indentations for a) W1Ni, W1Ni-b) 1 wt% CeB_6, c) 2 wt% NdB_6 and d) 2 wt% ErB_4 at 2500X magnification.

Wear resistance test results were given in Table 4.5. As results, W1Ni composites had 9.49×10^{-4} mm^3 wear volume loss. After adding of boride particulates, wear resistance of all samples increased. For W1Ni-1, 2 and 5 wt% CeB_6 particulate reinforcing, wear volume loss was 2.51, 0.99, and 1.3×10^{-4} mm^3, respectively. In addition, for W1Ni-1, 2 and 5 wt% NdB_6 particulate reinforcing, wear volume loss was 1.96, 1.68 and 1.45×10^{-4} mm^3, respectively. Also, wear volume loss was 4.36, 3.17, 1.14 and 3.89×10^{-4} mm^3 for W1Ni-1, 2, 5 and 10 wt% ErB_4 particulate reinforcing, respectively. Finally, wear resistance of W1Ni-10 wt% CeB_6 and NdB_6 were not measured because of occuring different phases so that, wear traces were not visible.

Table 4.5 : Wear resistance results of pressureless sintered samples.

Samples	Wear Volume Loss (mm^3)×10^{-4}	Wear Rate (mm^3 N^{-1} m^{-1}) ×10^{-5}	Wear Friction	Relative Wear Volume Loss
W1Ni	9.49	1,187	0.453	1
W1Ni - 1 CeB_6	2.51	0,314	0.415	0,26
W1Ni - 2 CeB_6	0.99	0,124	0.316	0,10
W1Ni - 5 CeB_6	1.3	0,163	0.413	0,14
W1Ni – 10 CeB_6	-	-	-	-
W1Ni – 1 NdB_6	1.96	0,245	0.408	0,21
W1Ni – 2 NdB_6	1.68	0,211	0.385	0,18
W1Ni – 5 NdB_6	1.45	0,181	0.413	0,15
W1Ni – 10 NdB_6	-	-	-	-
W1Ni – 1 ErB_4	4.36	0,545	0.439	0,50
W1Ni – 2 ErB_4	3.17	0,396	0.404	0,33
W1Ni – 5 ErB_4	1.14	0,142	0.412	0,12
W1Ni – 10 ErB_4	3.89	0,486	0.496	0,41

When relative wear volume loss was calculated, W1Ni-1 wt% ErB_4 pressureless sintered sample had the highest value, and W1Ni-2 wt% CeB_6 pressureless sintered sample had the lowest value. It was shown in Figure 4.63

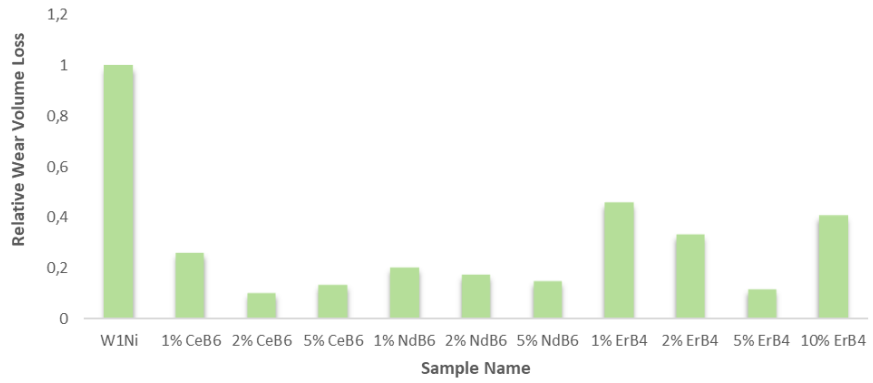

Figure 4.63 : Relative wear volume loss results for pressureless sintered samples.

Wear trace images acquired from optical microscope of W1Ni, W1Ni-1 wt% CeB_6, 2 wt% CeB_6, 5 wt% CeB_6, 1 wt% NdB_6, 2 wt% NdB_6, 5 wt% NdB_6, 1 wt% ErB_4, 2 wt% ErB_4, 5 wt% ErB_4 and 10 wt% ErB_4 at 500 µm was shown in Figure 4.64. When images were compared with wear volume loss results that is shown in Table 4.5, W1Ni-2 wt% CeB_6 sample showed the lowest wear volume loss (0.99×10^{-4} mm^3). Also, wear traces of W1Ni, W1Ni-1 wt% CeB_6, 2 wt% CeB_6, 5 wt% CeB_6, 1 wt% NdB_6, 2 wt% NdB_6, 5 wt% NdB_6, 1 wt% ErB_4, 2 wt% ErB_4, 5 wt% ErB_4 and 10 wt% ErB_4 at 500 µm was shown in Figure 4.65.

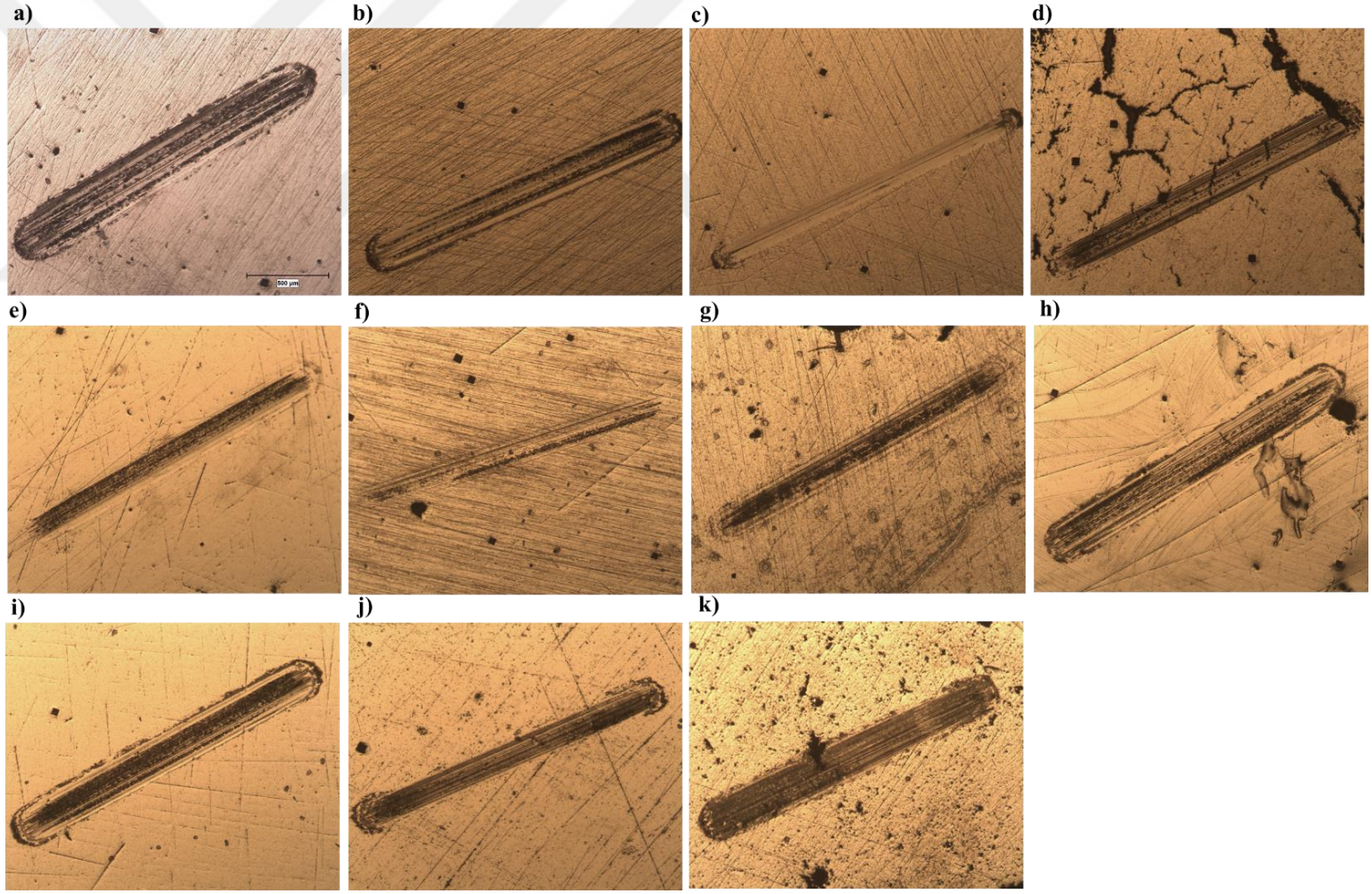

Figure 4.64 : Wear traces of a) W1Ni and W1Ni-b) 1 wt% CeB_6, c) 2 wt% CeB_6, d) 5 wt% CeB_6 e) 1 wt% NdB_6, f) 2 wt% NdB_6, g) 5 wt% NdB_6, h) 1 wt% ErB_4, i) 2 wt% ErB_4, j) 5 wt% ErB_4 and k) 10 wt% ErB_4 at 500 µm.

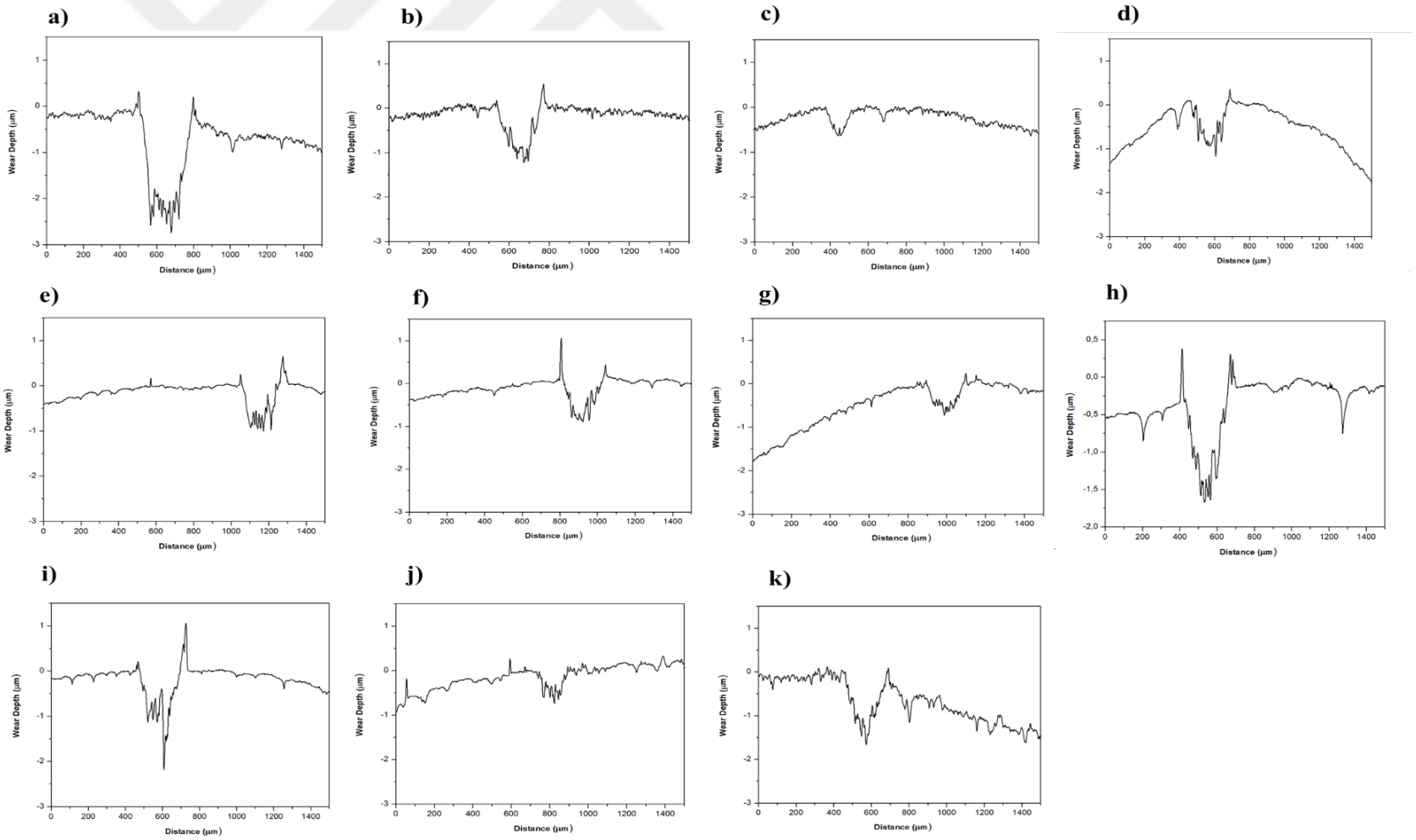

Figure 4.65 : Wear traces of a) W1Ni and W1Ni-b) 1 wt% CeB_6, c) 2 wt% CeB_6, d) 5 wt% CeB_6 e) 1 wt% NdB_6, f) 2 wt% NdB_6, g) 5 wt% NdB_6, h) 1 wt% ErB_4, i) 2 wt% ErB_4, j) 5 wt% ErB_4 and k) 10 wt% ErB_4.

Wear traces at high magnification (3000X) images for W1Ni-1 wt% NdB_6, 2 wt% NdB_6, 5 wt% NdB_6 were shown in Figure 4.66. Abrassive wear behaviour was observed in these structures.

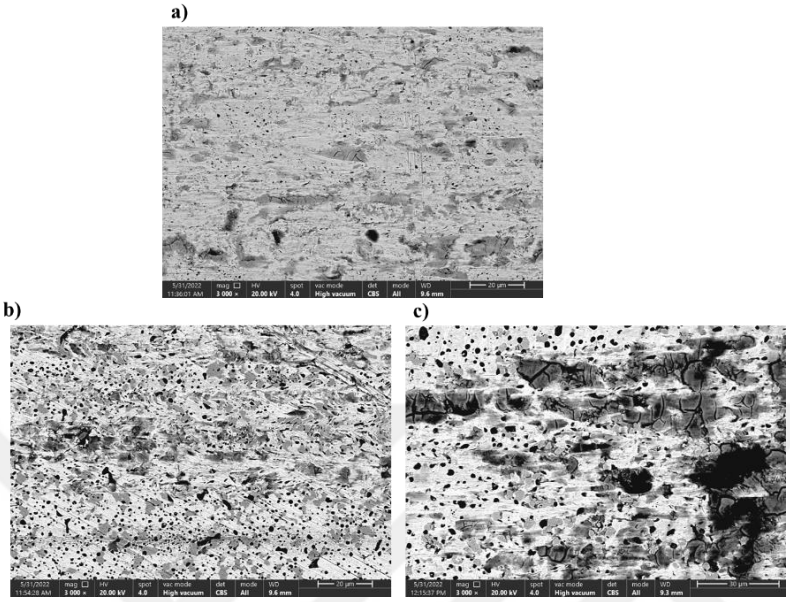

Figure 4.66 : Wear traces of W1Ni-a) 1 wt% NdB_6, b) 2 wt% NdB_6 and c) 5 wt% NdB_6 at 3000X magnification.

Wear traces at high magnification (3000X) images for W1Ni-1 wt% ErB_4, 2 wt% ErB_4, 5 wt% ErB_4 and 10 wt% ErB_4 were shown in Figure 4.67. Abrassive wear behaviour was observed in these structures.

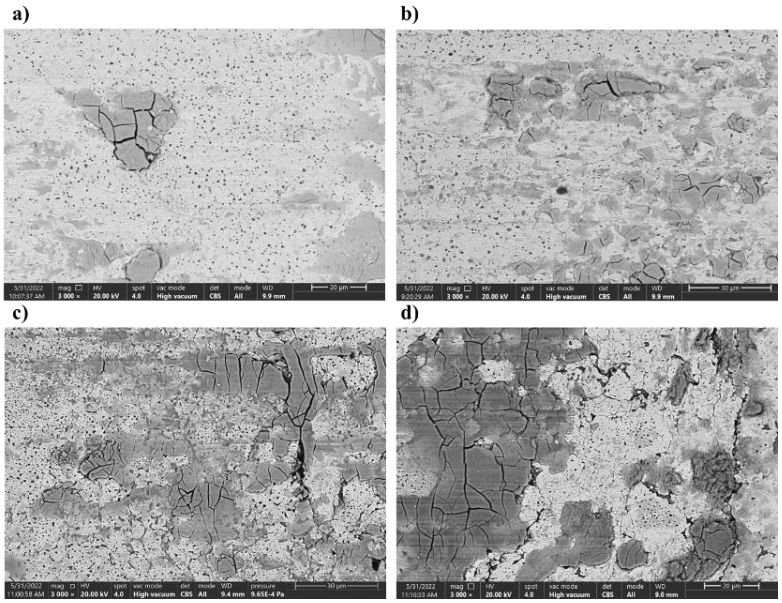

Figure 4.67 : Wear traces of W1Ni-a) 1 wt% ErB_4, b) 2 wt% ErB_4 c) 5 wt% ErB_4 and d) 10 wt% ErB_4 at 3000X magnification.

As point EDS results which is shown in Figure 4.68, W is the highest element for all points.

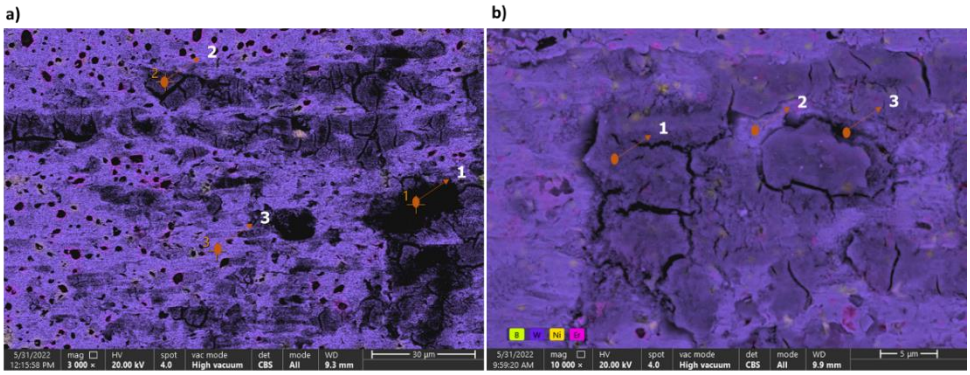

Points	W	Ni	B	Nd
1	90.7	0.5	8.7	0.2
2	86.3	2.2	9.8	1.7
3	94.1	0.0	5.9	0.0

Points	W	Ni	B	Er
1	85.4	4.0	7.5	3.1
2	85.3	6.3	7.9	2.5
3	92.4	0.6	5.1	2.0

Figure 4.68 : Point EDS results for W1Ni-a) 5 wt% NdB_6 and b) 2 wt% ErB_4.

All samples were arranged as nearly 10 mm diameter and 2 mm height bulk samples. All samples were exposed to 20-eV He^+ ion irradiation with a flux of 1.102×10^{21} ions/(m^2s). Irradiance fluence was set 1.32×10^{24} ions/m^2 with 20 min durations. After radiation test, XRD was done for all samples. XRD results of W1Ni, W1Ni-1, 2 and 5 wt% CeB_6 pressureless sintered samples after He^+ irradiation did not change especially. It was shown in Figure 4.69.

W1Ni peaks were shifting to right after He^+ irradiation test. It was given in Fig. 4.70a. Different magnification (40000, 80000 and 100000X) of SEM images were shown in Figure 4.70b/c/d. Fuzz structure was observed on surface after He^+ irradiation test. In literature, same structure was examined [33,35]. W1Ni-1 wt% CeB_6 and 2 wt% CeB_6 pressureless sintered sample peaks that is shown in Figure 4.71a and Figure 4.72a were shifting to left after He^+ irradiation test. Different magnification (40000, 80000 and 160000X) of SEM images were shown in Figure 4.71b/c/d and Figure 4.72b/c/d. Fuzz structure was observed on surface after He^+ irradiation test. Also, some pores were examined on surface that is given in Figure 4.71b. W1Ni- pressureless sintered sample peaks that is shown in were shifting to right after He^+ irradiation test. Fuzz structure was observed on surface after He^+ irradiation test. Also, pores were examined on surface that is given in Figure 4.72c.

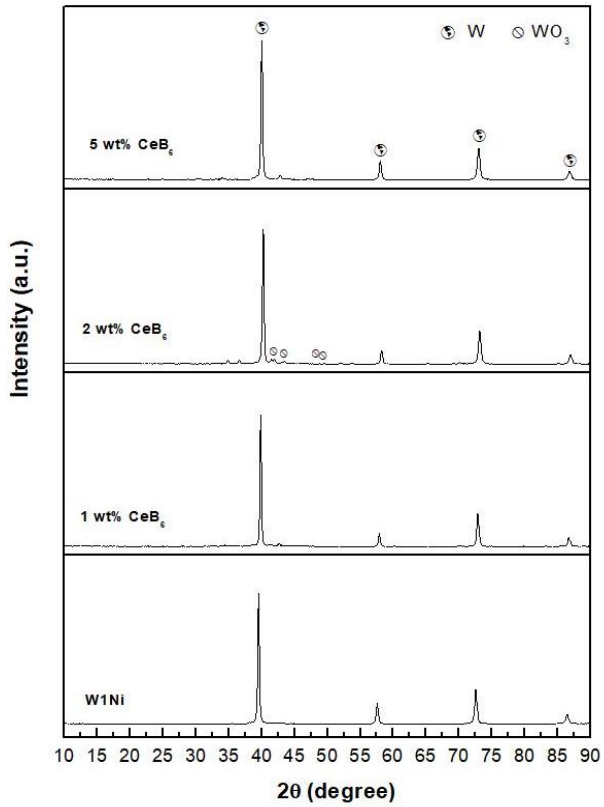

Figure 4.69 : XRD patterns of W1Ni, W1Ni-1, 2 and 5 wt% CeB_6 pressureless sintered samples after He^+ irradiation.

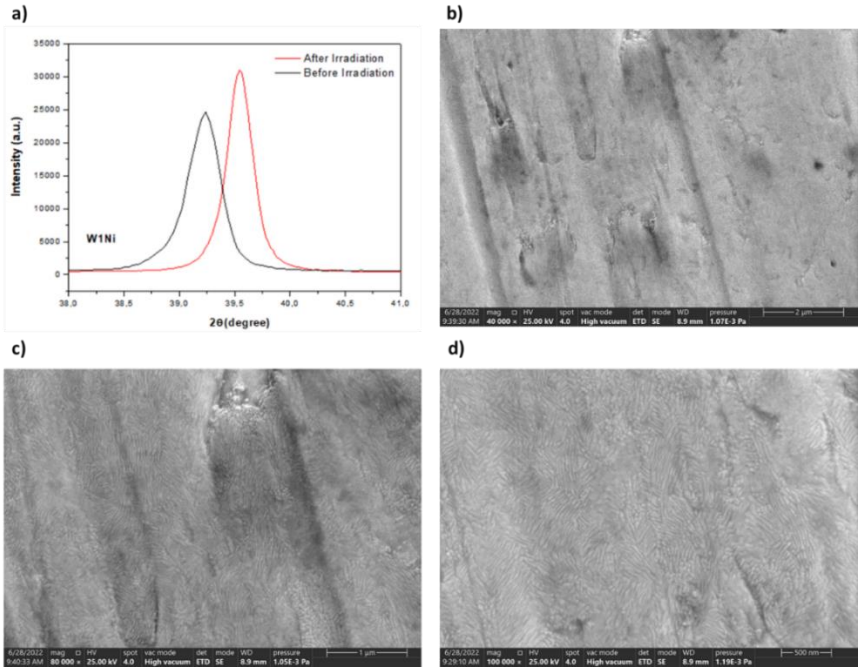

Figure 4.70 : a) XRD peak shifting of W1Ni, and SEM images at b) 40000, c) 80000, d) 100000X.

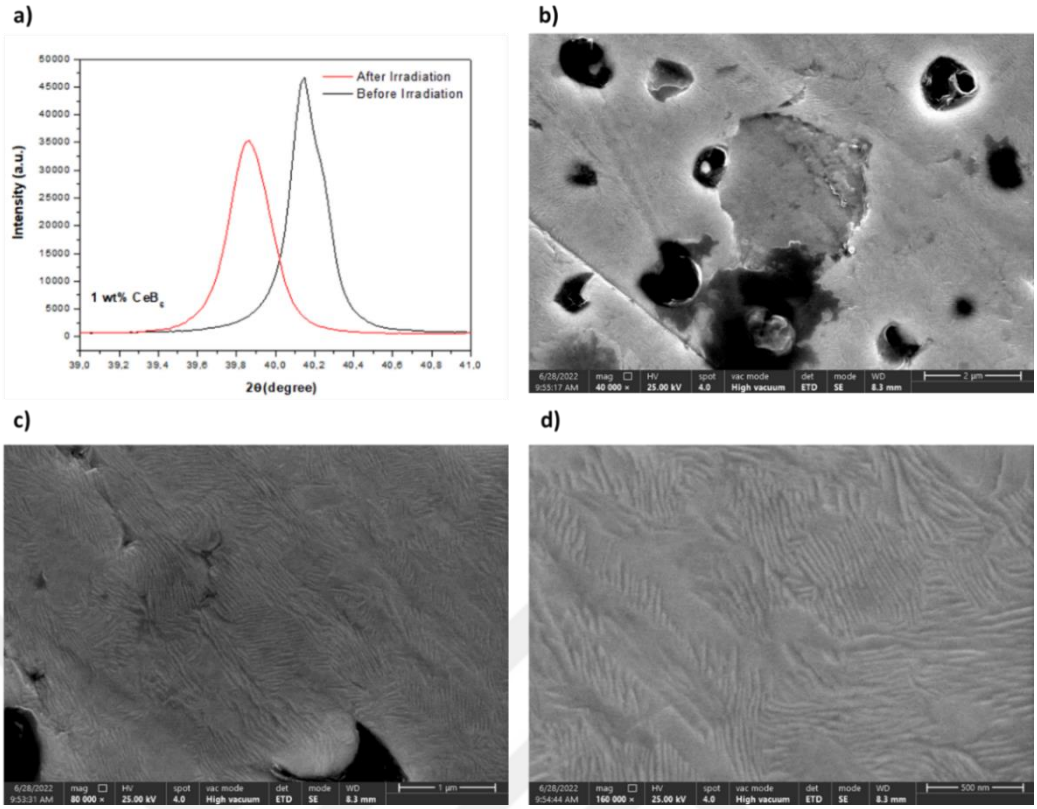

Figure 4.71 : a) XRD peak shifting of W1Ni-1 wt% CeB_6, and SEM images at b) 40000, c) 80000, d) 160000X.

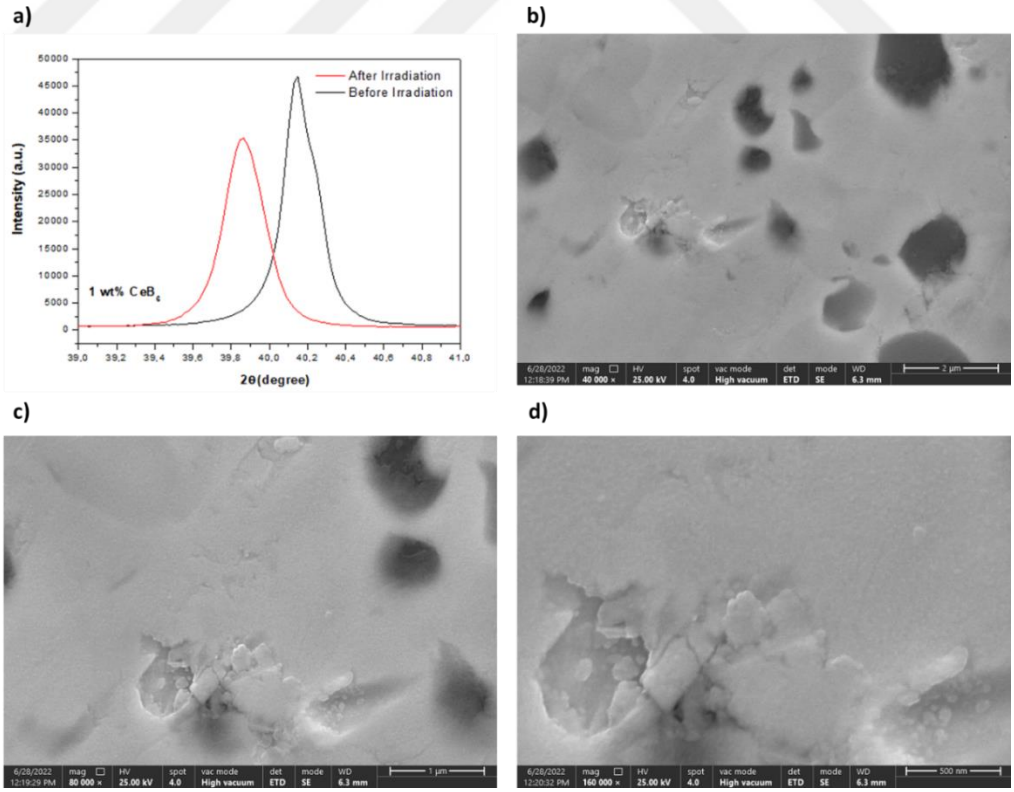

Figure 4.72 : a) XRD peak shifting of W1Ni-2 wt% CeB_6, and SEM images at b) 40000, c) 80000, d) 160000X.

W1Ni-5 wt% CeB_6 pressureless sintered sample peaks that is shown in Figure 4.73a were shifting to left after He^+ irradiation test. Different magnification (40000, 80000 and 160000X) of SEM images were shown in Figure 4.73b/c/d. Fuzz structure and cracks were observed on surface after He^+ irradiation test. Also, some pores were examined on surface that is given in Figure 4.73c.

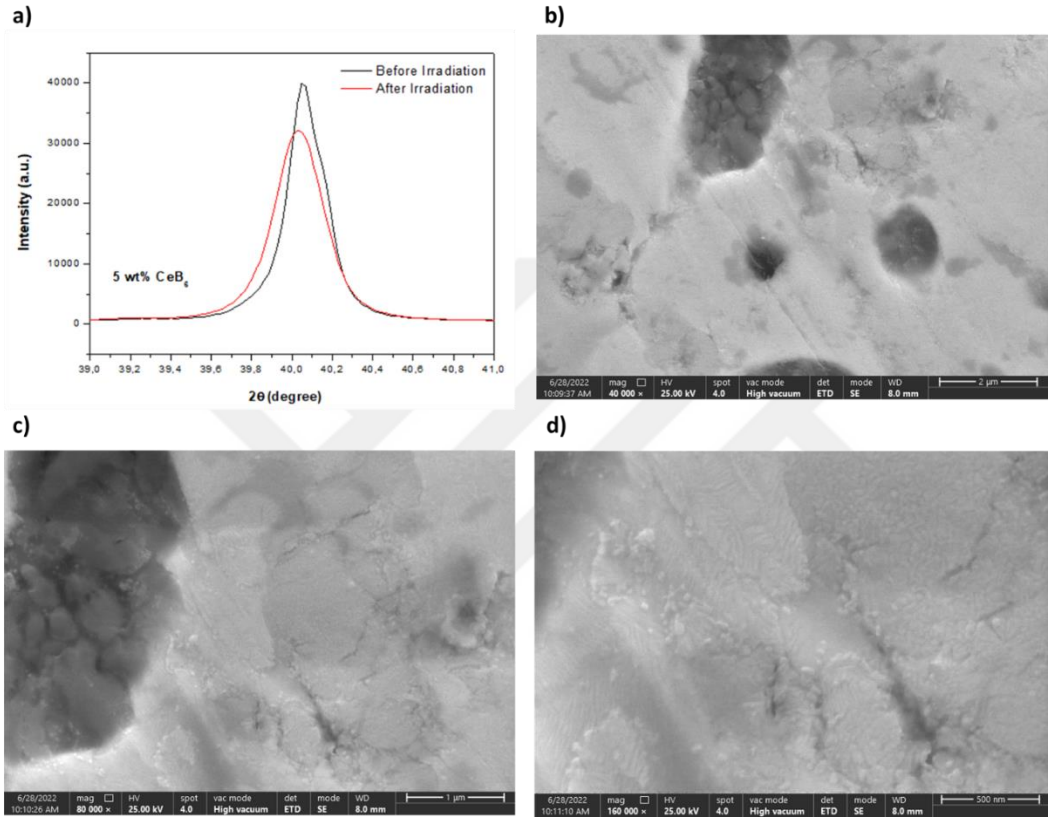

Figure 4.73 : a) XRD peak shifting of W1Ni-5 wt% CeB_6, and SEM images at b) 40000, c) 80000, d) 160000X.

XRD results of W1Ni, W1Ni-1, 2 and 5 wt% NdB_6 pressureless sintered samples after He^+ irradiation. It is shown in Figure 4.74. In XRD patterns, only peak shifting was observed. There was no another phase peaks.

W1Ni-1 wt% NdB_6 pressureless sintered sample peaks that is shown in Figure 4.75a were shifting to left after He^+ irradiation test. Different magnification (40000, 80000 and 160000X) of SEM images were shown in Figure 4.75b/c/d. Fuzz structure around holes was observed on surface after He^+ irradiation test. Also, pores which had small dots inside its were examined on surface that is given in Figure 4.75b,c.

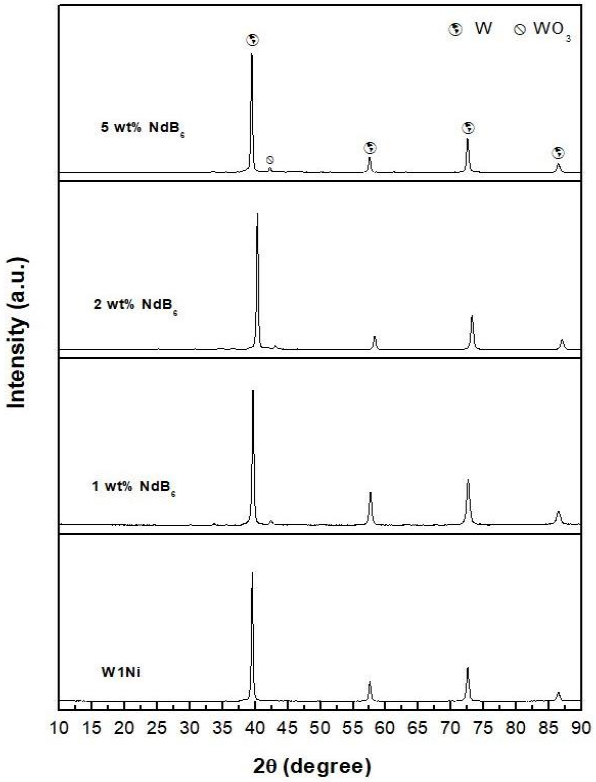

Figure 4.74 : XRD results of W1Ni, W1Ni-1, 2 and 5 wt% NdB_6 pressureless sintered samples after He^+ irradiation.

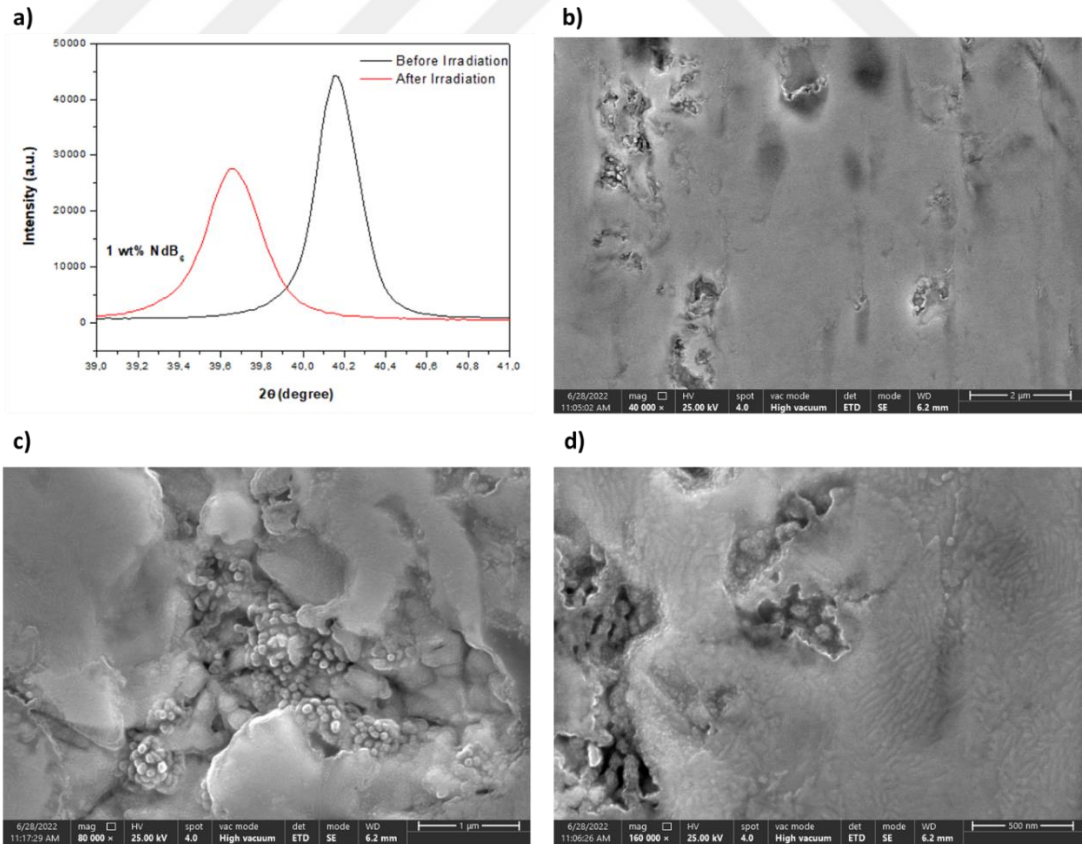

Figure 4.75 : a) XRD peak shifting of W1Ni-1 wt% NdB_6, and SEM images at b) 40000, c) 80000, d) 160000X.

W1Ni-2 wt% NdB_6 pressureless sintered sample peaks that is shown in Figure 4.76a were shifting to right after He^+ irradiation test. Different magnification (40000, 80000 and 160000X) of SEM images were shown in Figure 4.76b/c/d. Fuzz structure was not observed on surface after He^+ irradiation test. Also, small pores were examined on surface that is given in Figure 4.76b,c. W1Ni-5 wt% NdB_6 pressureless sintered sample peaks that is shown in Figure 4.77a were shifting to left He^+ irradiation test. Different magnification (20000, 80000 and 160000X) of SEM images were shown in Figure 4.77b/c/d. Surface deformation was observed on surface. When EDS was done for surface, oxygen and neodymium were too high.

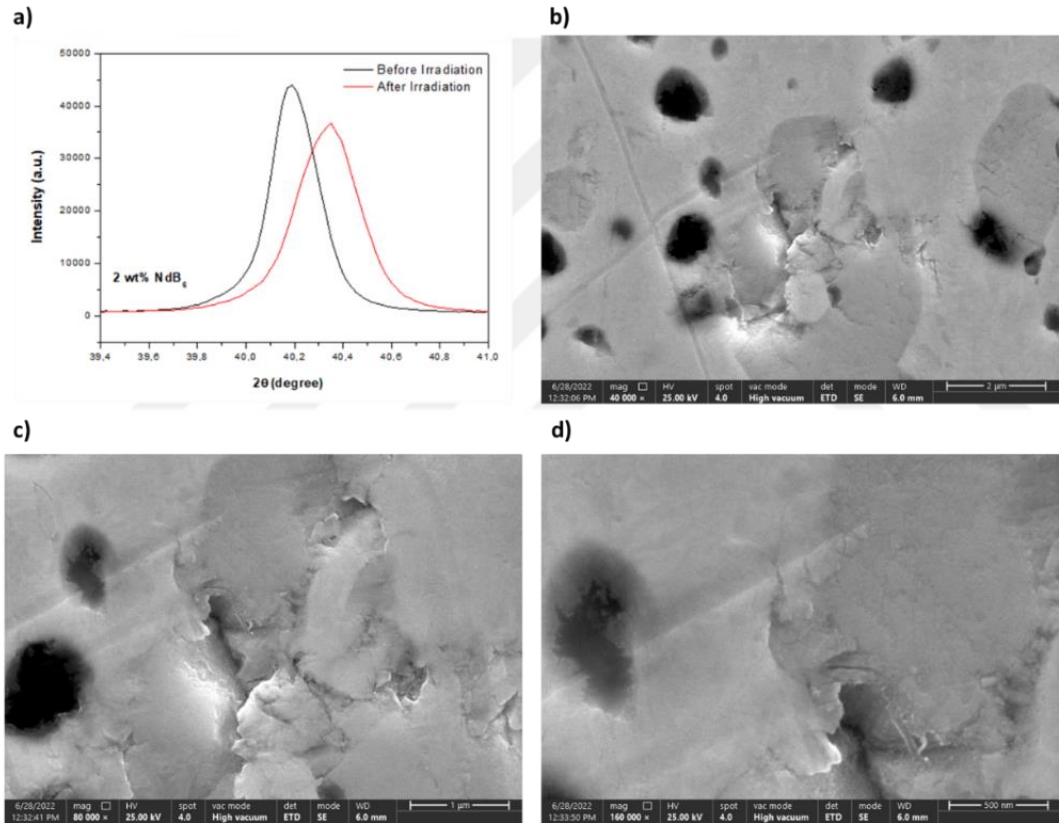

Figure 4.76 : a) XRD peak shifting of W1Ni-2 wt% NdB_6, and SEM images at b) 40000, c) 80000, d) 160000X.

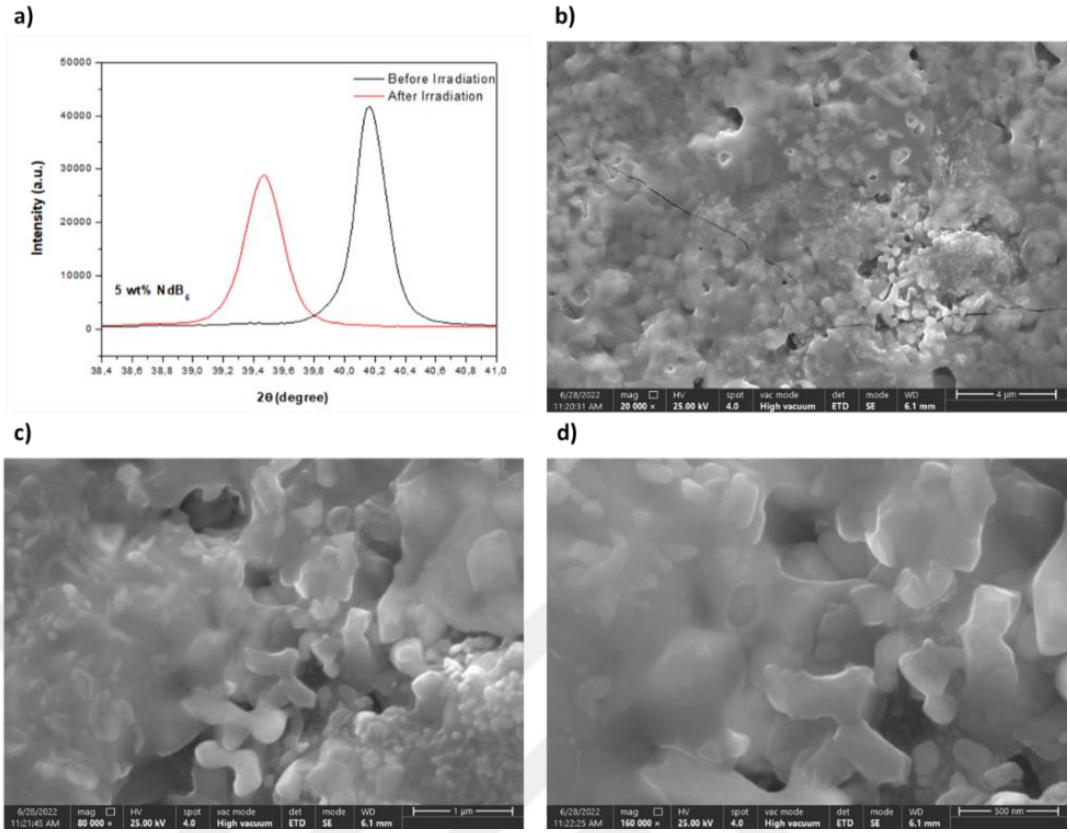

Figure 4.77 : a) XRD peak shifting of W1Ni-5 wt% NdB_6, and SEM images at b) 20000, c) 80000, d) 160000X.

XRD results of W1Ni, W1Ni-1, 2, 5 and 10 wt% ErB_4 pressureless sintered samples after He^+ irradiation test were given in Figure 4.78. Any oxide or carbide peaks were not observed, and only peak shifting was detected.

W1Ni-1 wt% ErB_4 pressureless sintered sample peaks that are shown in Figure 4.79a were shifting to left He^+ irradiation test. Different magnification (20000, 80000 and 160000X) of SEM images were shown in Figure 4.79b/c/d. This samples showed very good resistance to radiation. There were small and less pores on surface.

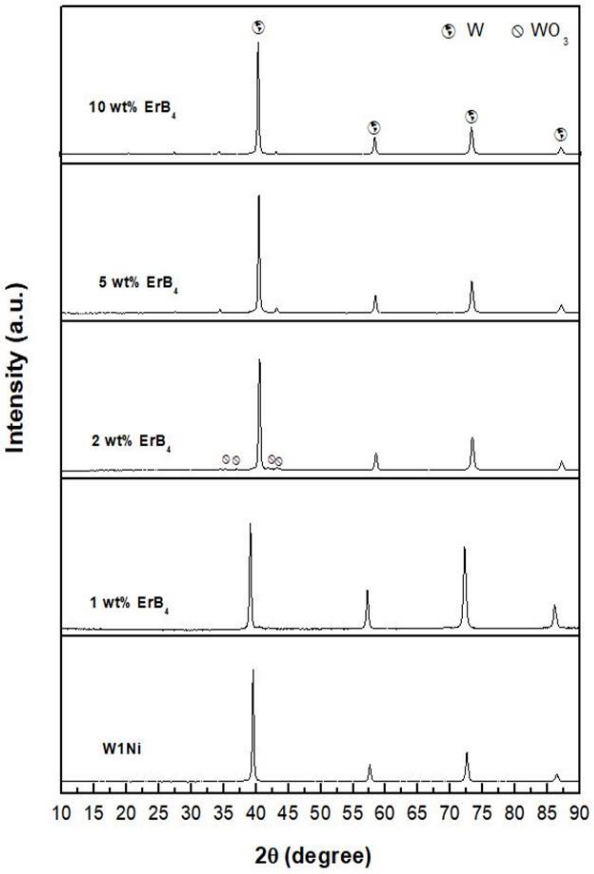

Figure 4.78 : XRD results of W1Ni, W1Ni-1, 2, 5 and 10 wt% ErB_4 pressureless sintered samples after He^+ irradiation.

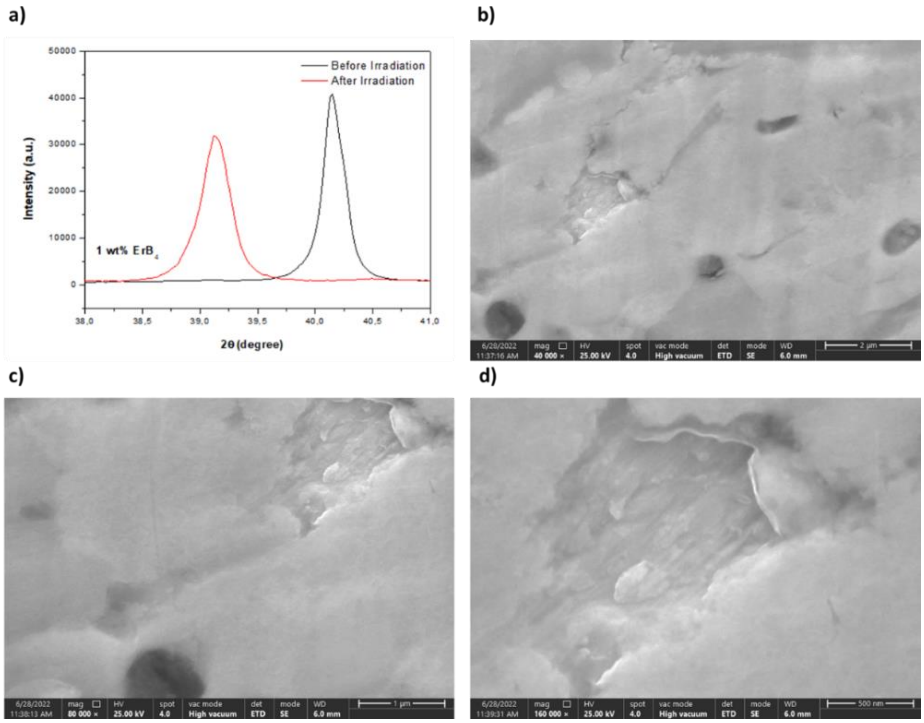

Figure 4.79 : a) XRD peak shifting of W1Ni-1 wt% ErB_4, and SEM images at b) 20000, c) 80000, d) 160000X.

W1Ni-2 wt% ErB_4 pressureless sintered sample peaks that is shown in Figure 4.80a were shifting to right He^+ irradiation test. Different magnification (20000, 80000 and 160000X) of SEM images were shown in Figure 4.80b/c/d. Fuzz structure was not observed on surface. Only Ni high area showed some fuzz structure. There were small holes on surface because of He^+ irradiation.

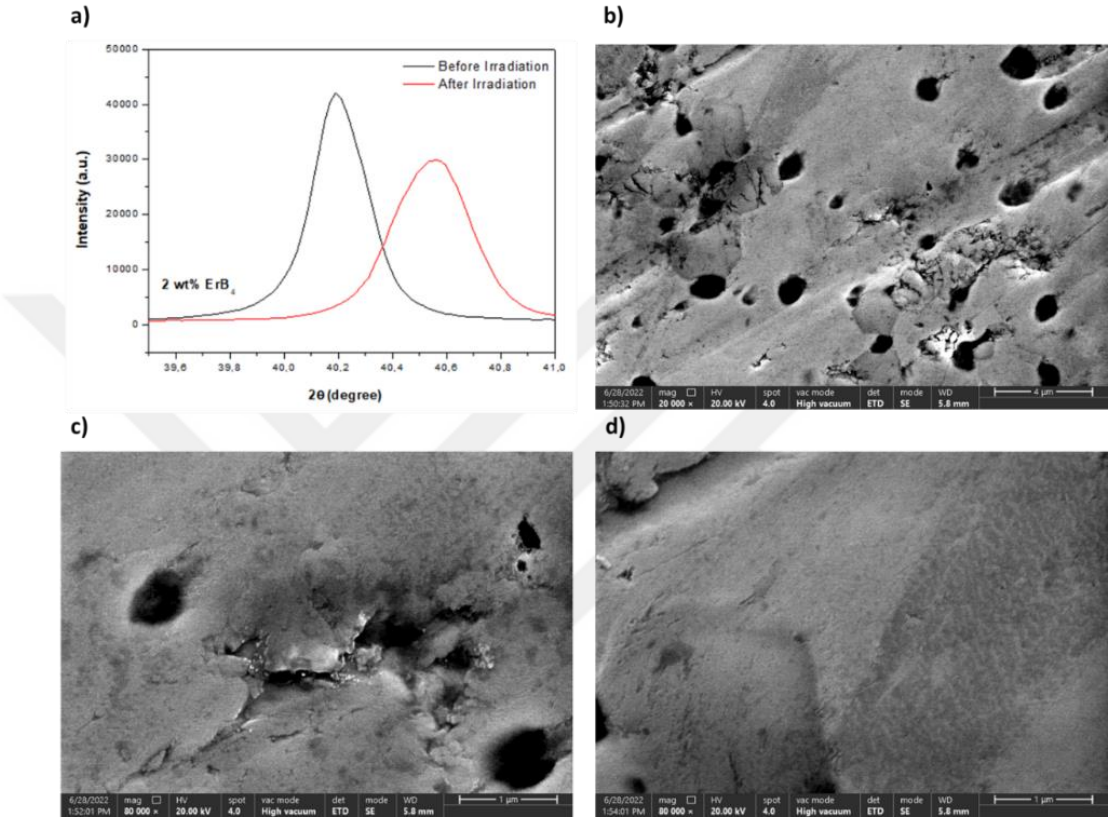

Figure 4.80 : a) XRD peak shifting of W1Ni-2 wt% ErB_4, and SEM images at b) 20000, c) 80000, d) 160000X.

W1Ni-5 wt% ErB_4 pressureless sintered sample peaks that is shown in Figure 4.81a were shifting to right He^+ irradiation test. Also, W1Ni-10 wt% ErB_4 pressureless sintered sample peaks that is shown in Figure 4.82a were shifting to left He^+ irradiation test. Different magnification (20000/40000 80000 and 160000X) of SEM images were shown in Figure 4.81b/c/d and in Figure 4.82b/c/d. Fuzz structure was not observed on surface for W1Ni-5 wt% ErB_4 sample. There were small dots on surface. Also, there were some colors changing on surface. Fuzz structure was not observed on surface with small dots for W1Ni-10 wt% ErB_4 pressureless sintered sample.

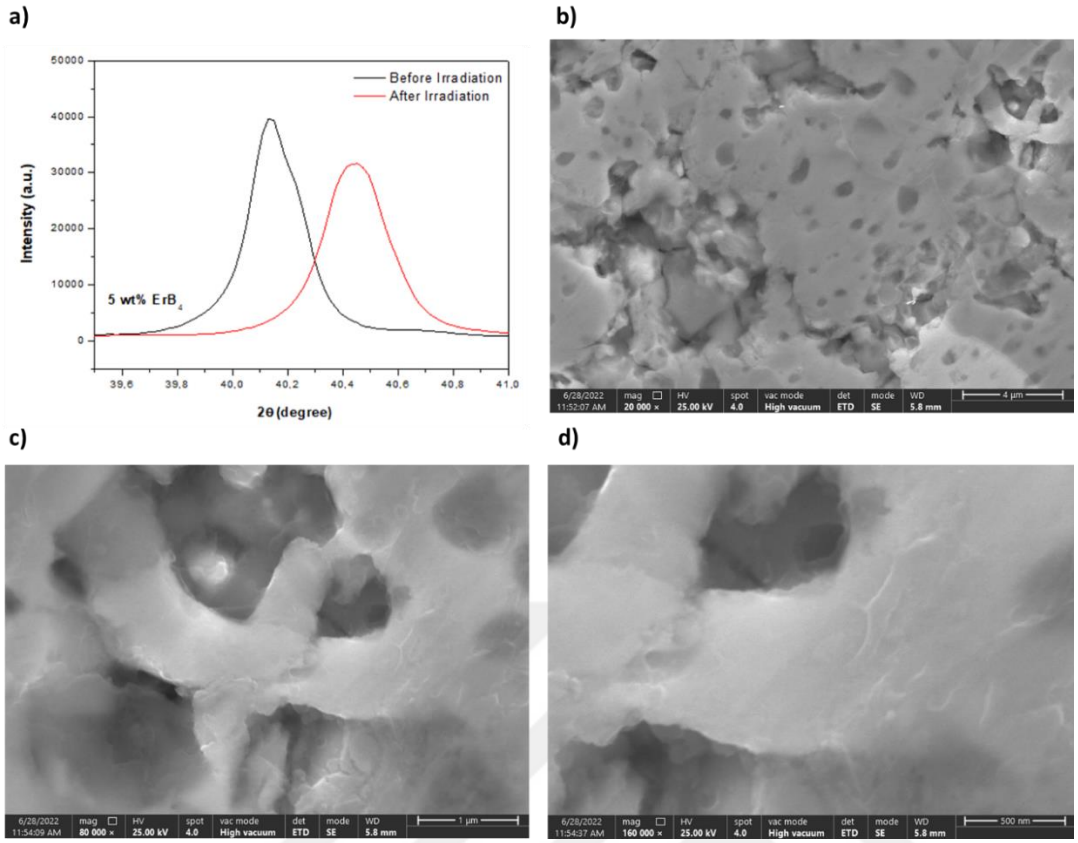

Figure 4.81 : a) XRD peak shifting of W1Ni-5 wt% ErB_4, and SEM images at b) 20000, c) 80000, d) 160000X.

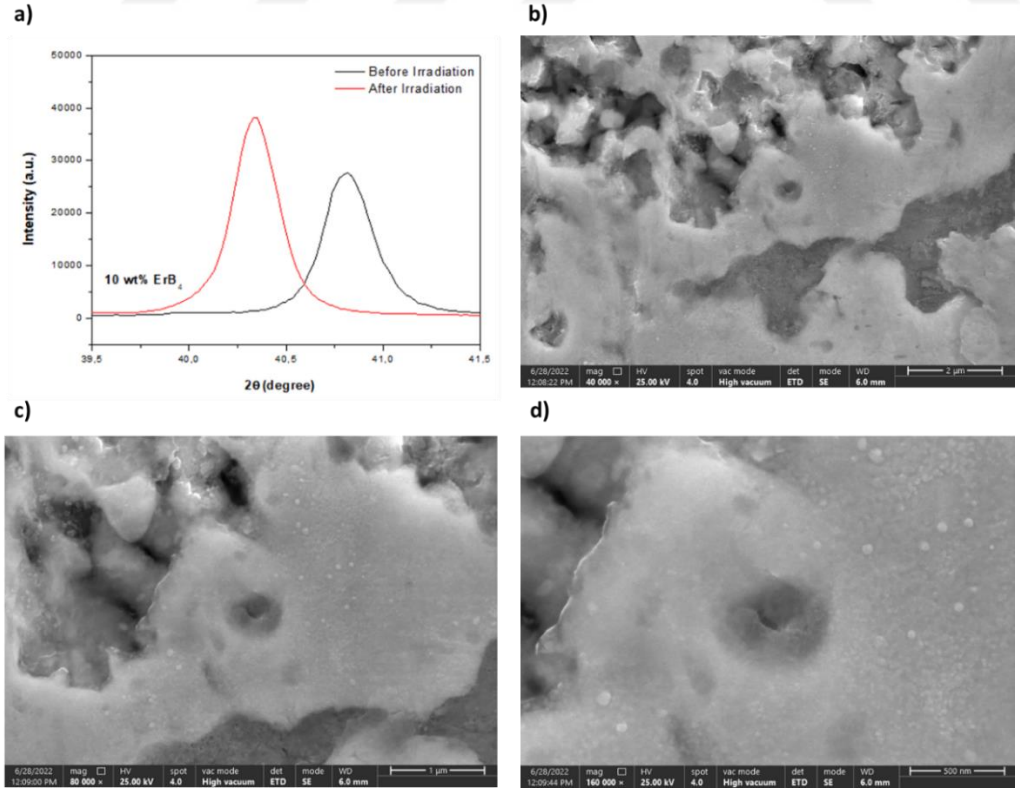

Figure 4.82 : a) XRD peak shifting of W1Ni-10 wt% ErB_4, and SEM images at b) 40000, c) 80000, d) 160000X.

4.2.2.2 Characterization of spark plasma sintered W1Ni composites

Firstly, CeB_6 powders were produced with mechanochemical synthesis with 5 h and HCl leaching. Then, 99 wt% W and 1 wt% Ni were mechanically alloyed for 6 h milling. After adding CeB_6 powders with different amounts (1, 5 and 10 wt%) to W1Ni with 6 h milling, SPS was applied to powder at 1410 °C for 1 min. XRD analysis was done to spark plasma sintered samples 10-90º with 2 º. As XRD results, four main peaks were obtained as W (ICDD Card No: 00-004-0806, Bravais lattice cubic, a = 0.316 nm). There was one phase which is small intensity to as WO_3 (ICDD Card No: 00-005-0364, Bravais lattice: monoclinic, a = 0.729 nm, b= 0.752 and c = 0.384 nm). When amount of CeB_6 was increased, intensity of main peaks decreased. After 5 wt% CeB_6 adding, W_2B (ICDD Card No: 00-025-0990, Bravais lattice: tetragonal, a = 0.557 nm and c = 0.474 nm) phase and W_2B_5 (ICDD Card No: 03-065-3591, Bravais lattice: hexagonal, a = 0.298 nm and c = 0.139 nm) phases were observed in structure. While main phase was W, W_2B started to be main phase because of more boron. Also, W peak did not observe for 10 wt% CeB_6. These results were shown in Figure 4.83.

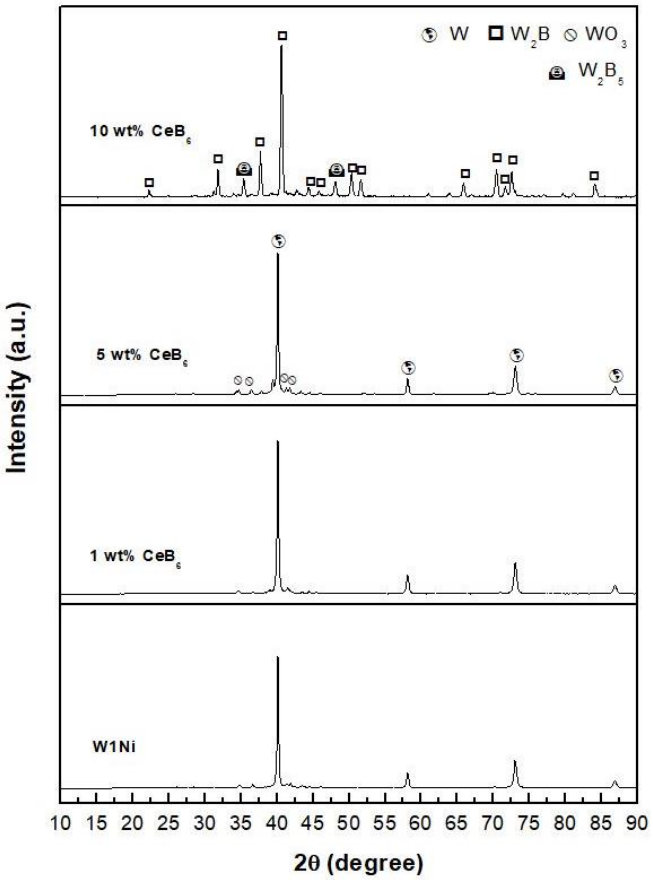

Figure 4.83 : XRD patterns of W1Ni composites reinforced with 1, 5 and 10 wt% CeB_6 with spark plasma sintering.

SEM images of W1Ni and reinforced with 1, 5 and 10 wt% CeB_6 particulates were given in Figure 4.84. As images, dark areas were observed after adding CeB_6 particulates. Homogeneous structure was observed for W1Ni-10 wt% CeB_6 samples due to the occurrence of W_2B structure.

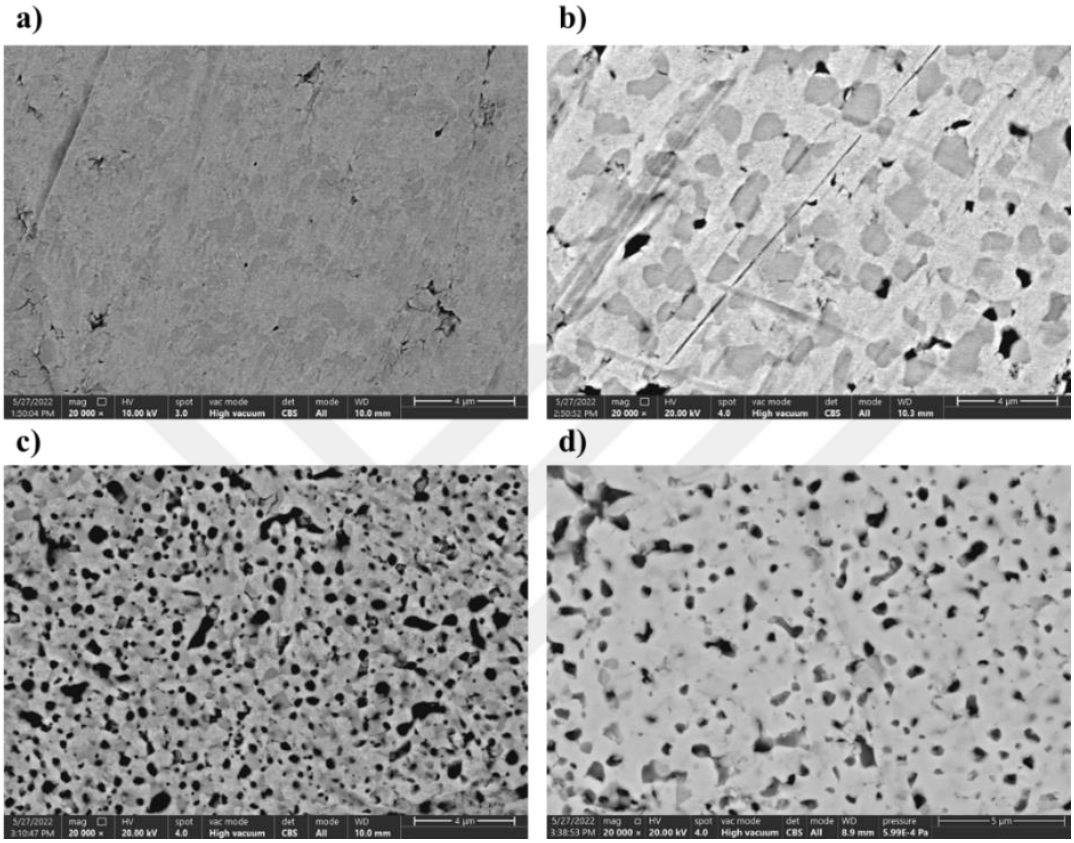

Figure 4.84 : SEM images of a) W1Ni, W1Ni-b) 1, c) 5 and d) 10 wt% CeB_6 at 20000X magnification.

Colorful EDS image and point EDS results for W1Ni were given in Figure 4.85. In this picture dark areas were observed as obtaining high Ni. When EDS results were examined, amount of W and Ni was observed as 99.2%, 0.8% and 86.6%, 13.4% for point 1 and 2, respectively.

Colorful EDS image and point EDS results for W1Ni-1, 2 and 5 wt% CeB_6 samples were given in Figure 4.86. All grey areas include high nickel amount with W and a little B. Cerium was not observed for this area. For white area, W was main phases nearly 90% with small amount B and Ni. Ce was main element for all dark areas. These dark areas were growing with increasing amount of Ce.

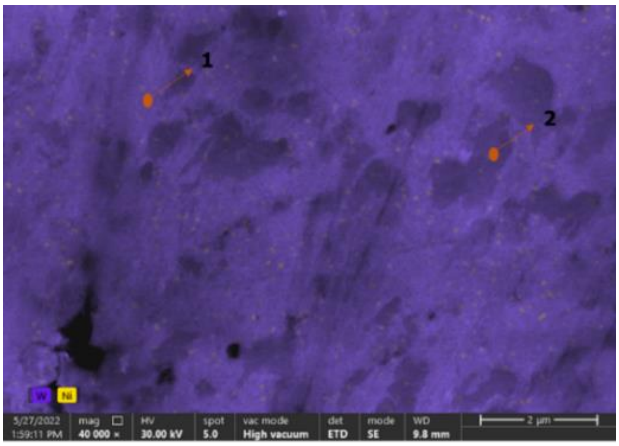

Points	W	Ni
1	99.2	0.8
2	86.6	13.4

Figure 4.85 : Colorful EDS image and point EDS results for W1Ni.

a)

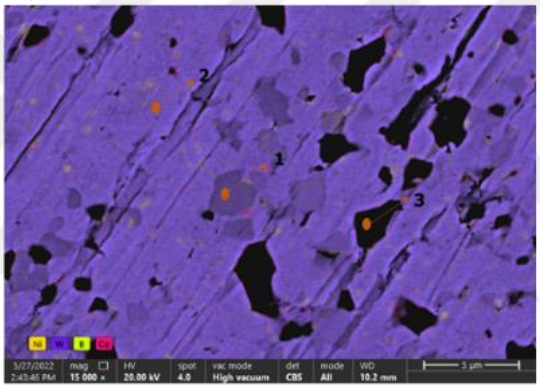

Points	W	Ni	B	Ce
1	72.3	20.8	6.8	0.1
2	91.9	0.7	7.5	0.0
3	78.2	0.4	0.0	21.3

b)

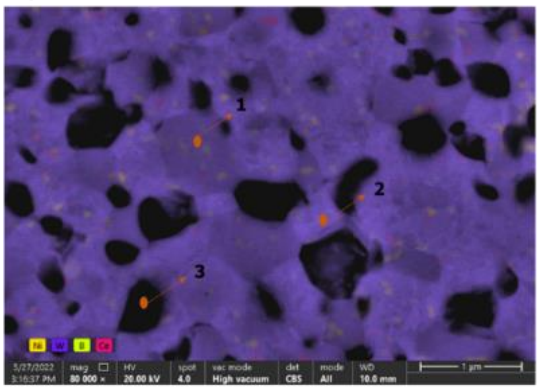

Points	W	Ni	B	Ce
1	83.4	9.4	7.0	0.2
2	90.2	2.4	6.9	0.5
3	85.6	1.4	6.2	6.8

c)

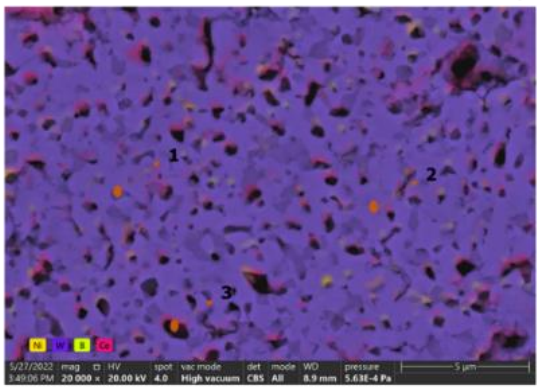

Points	W	Ni	B	Ce
1	76.9	11.4	11.3	0.5
2	86.1	1.6	10.7	1.6
3	73.3	1.6	6.6	18.6

Figure 4.86 : Colorful EDS image and point EDS results for W1Ni-a) 1, b) 5 and c) 10 wt% CeB_6.

Firstly, NdB_6 powders were produced with mechanochemical synthesis with 5 h and HCl leaching. Then, 99 wt% W and 1 wt% Ni were mechanically alloyed for 6 h milling. After adding NdB_6 powders with different amounts (1, 5 and 10 wt%) to W1Ni with 6 h milling, SPS was applied to powder at 1410 °C for 1 min. XRD analysis was done to spark plasma sintered samples 10-90º with 2 º. As XRD results, four main peaks were obtained as W (ICDD Card No: 00-004-0806, Bravais lattice cubic, a = 0.316 nm). There was one phase which is small intensity to as WO_3 (ICDD Card No: 00-005-0364, Bravais lattice: monoclinic, a = 0.729 nm, b= 0.752 and c = 0.384 nm). When amount of NdB_6 was increased, intensity of main peaks decreased. After 5 wt% NdB_6 adding, W_2B (ICDD Card No: 00-025-0990, Bravais lattice: tetragonal, a = 0.557 nm and c = 0.474 nm) phase and W_2B_5 (ICDD Card No: 03-065-3591, Bravais lattice: hexagonal, a = 0.298 nm and c = 0.139 nm) phases were observed in structure. While main phase was W, W_2B started to be main phase because of high boron. W_2B was started to be observed for 5 wt% NdB_6 and W phase was not detected for 10 wt% NdB_6. These results were shown in Figure 4.87.

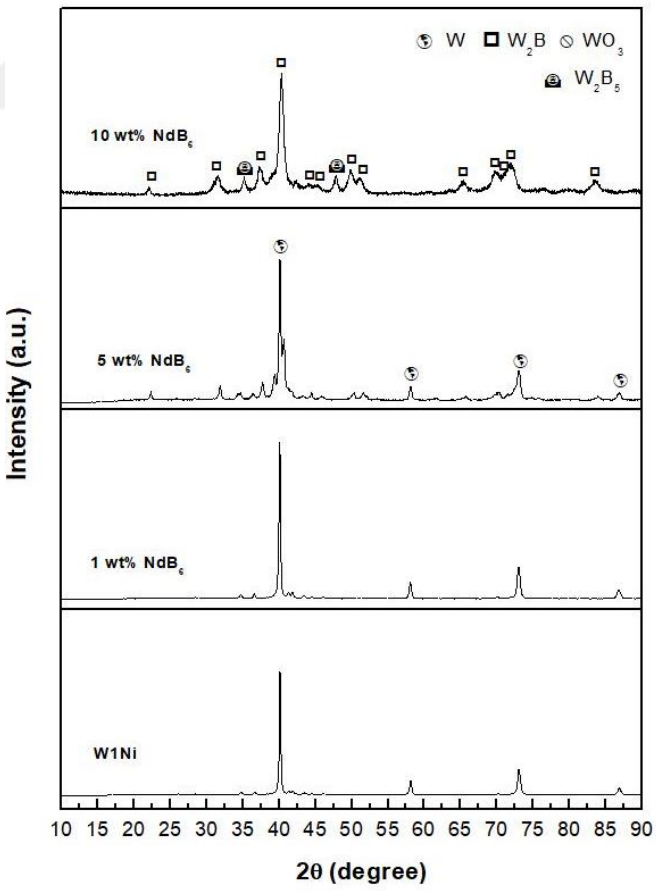

Figure 4.87 : XRD patterns of W1Ni composites reinforced with 1, 5 and 10 wt% NdB_6 with spark plasma sintering.

SEM images of W1Ni and reinforced with 1, 5 and 10 wt% NdB_6 particulates were given in Figure 4.88. As images, dark areas were observed after adding NdB_6 particulates. Homogeneous structure was observed for W1Ni-10 wt% NdB_6 samples due to the W_2B structure.

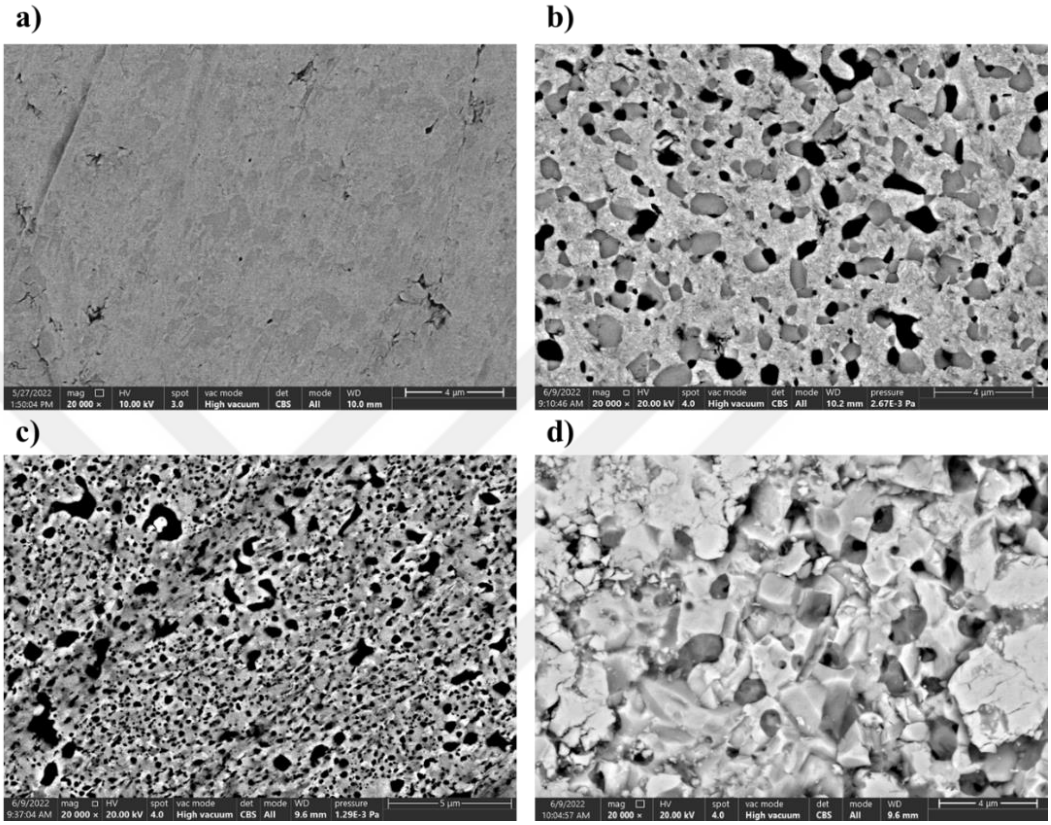

Figure 4.88 : SEM images of a) W1Ni, W1Ni-b) 1, c) 5 and d) 10 wt% NdB_6 at 20000X magnification.

Colorful EDS image and point EDS results for W1Ni-1, 5 and 10 wt% NdB_6 samples were given in Figure 4.89. All grey areas include high nickel amount with W and a little B. Neodmium did not observed for this area. For white area, W was main phases nearly 90% with small amount B and Ni. Nd was main element for all dark areas. These dark areas were growing with increasing amount of Nd.

a)

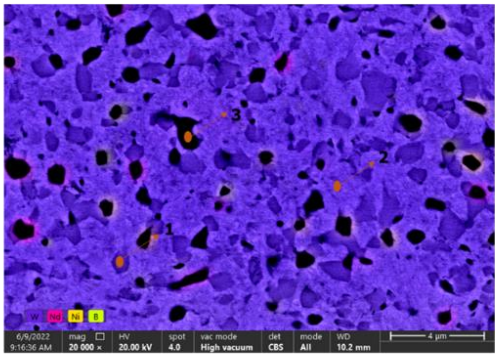

Points	W	Ni	B	Nd
1	80.8	11.3	7.6	0.3
2	90.4	2.2	7.2	0.2
3	79.0	1.0	10.6	9.3

b)

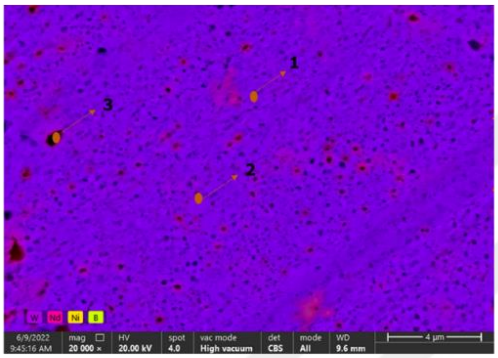

Points	W	Ni	B	Nd
1	84.6	3.5	8.3	3.6
2	89.3	1.3	7.4	2.0
3	79.4	1.8	8.6	10.1

c)

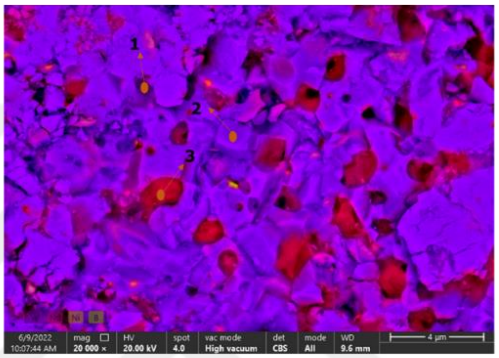

Points	W	Ni	B	Nd
1	76.9	11.4	11.3	0.5
2	88.7	0.2	10.8	0.4
3	16.1	0.5	5.4	78.0

Figure 4.89 : Colorful EDS image and point EDS results for W1Ni-a) 1, b) 5 and c) 10 wt% NdB_6.

Firstly, ErB_4 powders were produced with mechanochemical synthesis with 5 h milling and HCl leaching. Then, 99 wt% W and 1 wt% Ni were mechanically alloyed for 6 h milling. After adding ErB_4 powders with different amounts (1, 5 and 10 wt%) to W1Ni with 6 h milling, SPS was applied to powder at 1410 °C for 1 min. XRD analysis was done to spark plasma sintered samples 10-90º with 2 º. As XRD results, four main peaks were obtained as W (ICDD Card No: 00-004-0806, Bravais lattice cubic, a = 0.316 nm). There was one phase which is small intensity to as WO_3 (ICDD Card No: 00-005-0364, Bravais lattice: monoclinic, a = 0.729 nm, b= 0.752 and c = 0.384 nm). When amount of ErB_4 was increased, intensity of main peaks decreased. After 5 wt% ErB_4 adding, W_2B (ICDD Card No: 00-025-0990, Bravais lattice: tetragonal, a = 0.557 nm and c = 0.474 nm) phase and W_2B_5 (ICDD Card No: 03-065-3591, Bravais lattice: hexagonal, a = 0.298 nm and c = 0.139 nm) phases were observed in structure. While main phase was W, W_2B started to be main phase because of more boron. These results were shown in Figure 4.90.

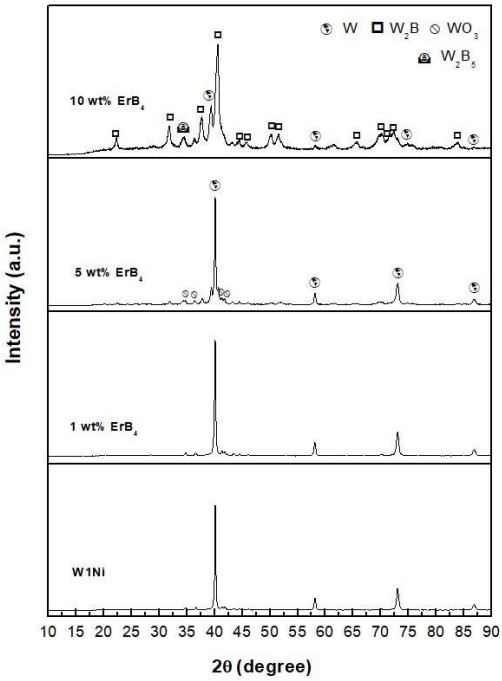

Figure 4.90 : XRD patterns of W1Ni composites reinforced with 1, 5 and 10 wt% ErB_4 with spark plasma sintering.

SEM images of W1Ni and reinforced with 1, 5 and 10 wt% ErB_4 particulates were given in Figure 4.91. As images, dark areas were observed after adding ErB_4 particulates. Homogeneous structure was observed for W1Ni-10 wt% ErB_4 samples because of occuring W_2B structure.

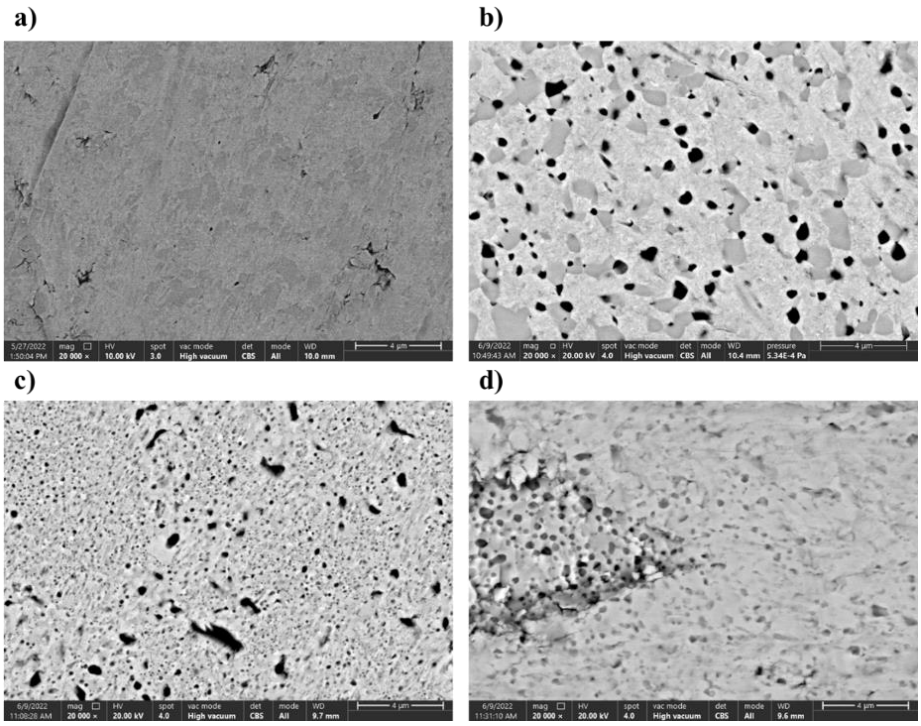

Figure 4.91 : SEM images of a) W1Ni, W1Ni-b) 1, c) 5 and d) 10 wt% ErB_4 at 20000X magnification.

Colorful EDS image and point EDS results for W1Ni-1, 5 and 10 wt% ErB_4 samples were given in Figure 4.92. All grey areas include high nickel amount with W and a little B. For white area, W was main phases nearly 90% with small amount B and Ni. Er was main element for all dark areas. These dark areas were growing with increasing amount of Er.

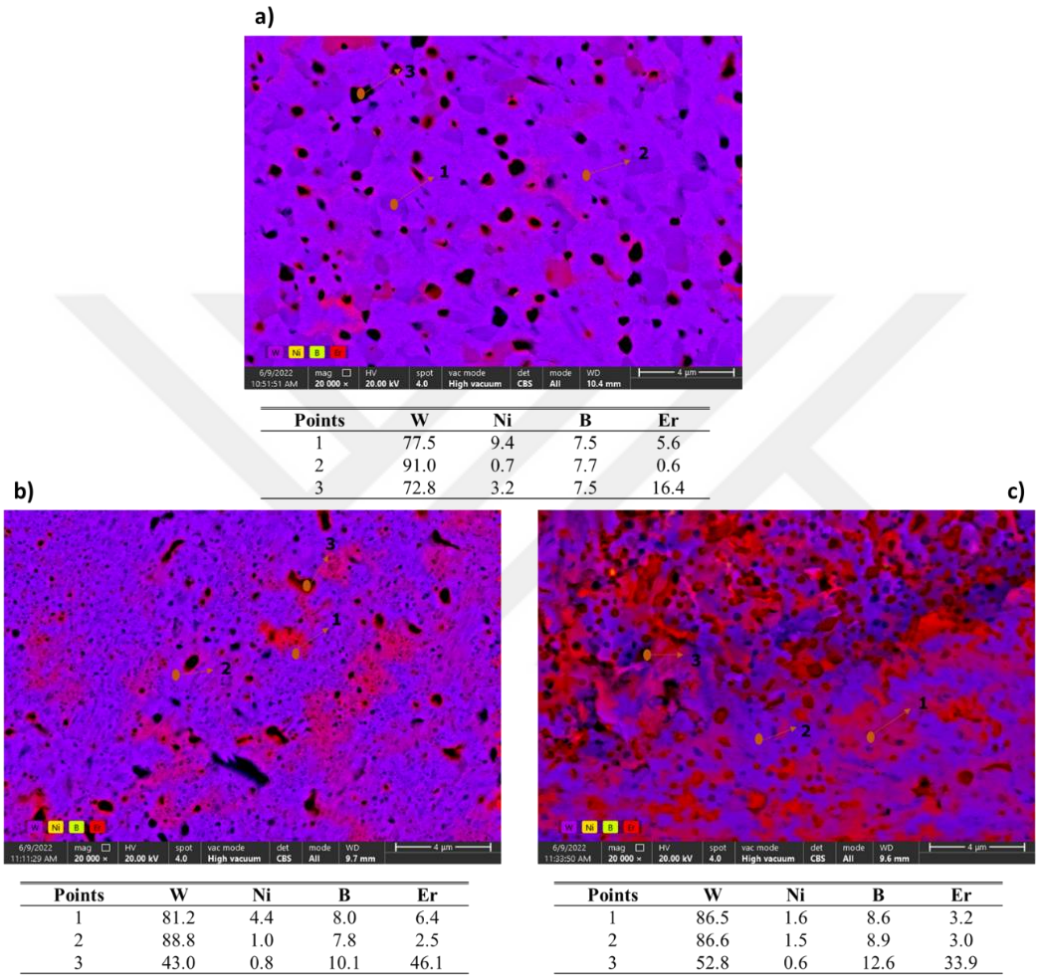

Points	W	Ni	B	Er
1	77.5	9.4	7.5	5.6
2	91.0	0.7	7.7	0.6
3	72.8	3.2	7.5	16.4

Points	W	Ni	B	Er
1	81.2	4.4	8.0	6.4
2	88.8	1.0	7.8	2.5
3	43.0	0.8	10.1	46.1

Points	W	Ni	B	Er
1	86.5	1.6	8.6	3.2
2	86.6	1.5	8.9	3.0
3	52.8	0.6	12.6	33.9

Figure 4.92 : Colorful EDS image and point EDS results for W1Ni-a) 1, b) 5 and c) 10 wt% ErB_4.

Theoretical, Archimedes' and relative densities of samples were given in the Table 4.6. As given results, when boride particulates added into W1Ni based composite, relative densities for all samples were decreased. W with 1 wt% Ni mechanically alloyed for 6 h, had the highest relative density as 91%. Then, with adding W1Ni-10 wt% CeB_6 gave higher relative density (98%) than W1Ni-1, 5 wt% CeB_6. Also, density of W1Ni-10 wt% NdB_6 sample was measured higher density (100%) than W1Ni-1, 5 wt% NdB_6. Finally, W1Ni-10 wt% ErB_4 had higher relative density (94%) than other adding ErB_4 particulates.

Table 4.6 : Density results of spark plasma sintered samples.

Samples	Theoretical Density (g/cm^3)	Archimedes' Density (g/cm^3)	Relative Density (%)
W1Ni	19.23	17.53	91
W1Ni - 1 CeB_6	18.52	16.42	89
W1Ni - 5 CeB_6	16.16	14.95	93
W1Ni - 10 CeB_6	13.99	13.71	98
W1Ni - 1 NdB_6	18.52	17.32	94
W1Ni - 5 NdB_6	16.16	15.39	95
W1Ni - 10 NdB_6	13.99	13.99	100
W1Ni - 1 ErB_4	18.79	17.18	91
W1Ni - 5 ErB_4	17.23	15.53	90
W1Ni - 10 ErB_4	15.66	14.79	94

Microhardness value of spark plasma sintered samples were given in Figure 4.93. Also, microhardness of W1Ni-10 wt% CeB_6, NdB_6 and ErB_4 were measured up 20 GPa because of obtaining W_2B phases. In literature, microhardness of W_2B is nearly 20 GPa [52,88–90]. For all the samples, 5 wt% boride particulate W1Ni base composites were given the highest microhardness value. For W1Ni-5 wt% CeB_6, NdB_6 and ErB_4 particulate W1Ni composites, microhardness values were measured as 10.11, 13.4 and 12.18 GPa, relatively. When amount of reinforcing boride particulate was increased, all microhardness values inreased.

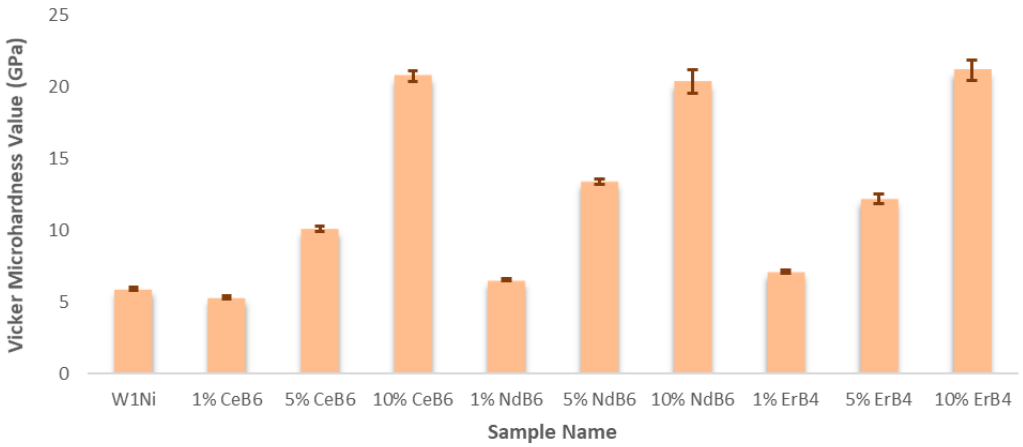

Figure 4.93 : Microhardness value of spark plasma sintered samples.

SEM images of microhardness indentations for W1Ni and W1Ni-1 wt% CeB_6 at 2500X magnification were shown in Figure 4.94. Microhardness value of W1Ni-1 wt% CeB_6 was lower than W1Ni. However, it was increasing with adding more CeB_6. Traces were started to be smaller with increasing amount of CeB_6.

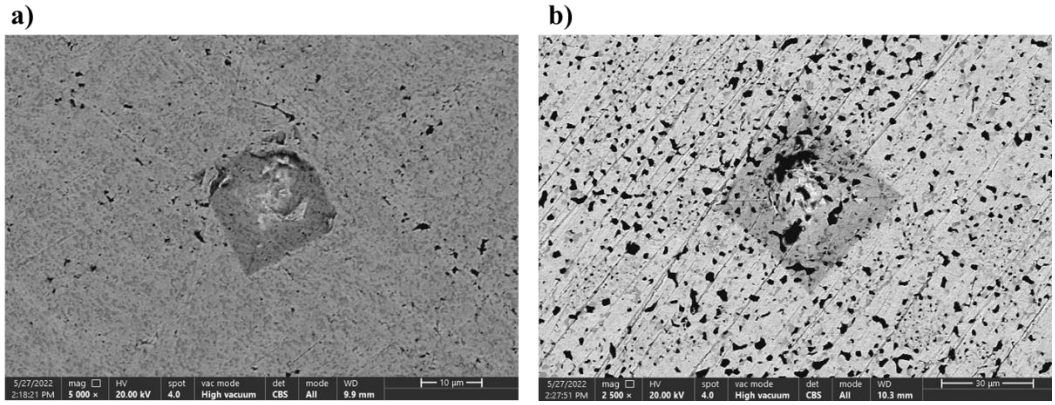

Figure 4.94 : SEM images of microhardness indentations for a) W1Ni, b) W1Ni-1 wt% CeB_6 at 2500X magnification.

SEM images of microhardness indentations for W1Ni and W1Ni-1, 5 wt% NdB_6 at 2500X magnification were shown in Figure 4.95. Traces were started to be smaller with increasing amount of NdB_6. W1Ni-10 wt% NdB_6 had very small indentations so that, it was not observed in microscope.

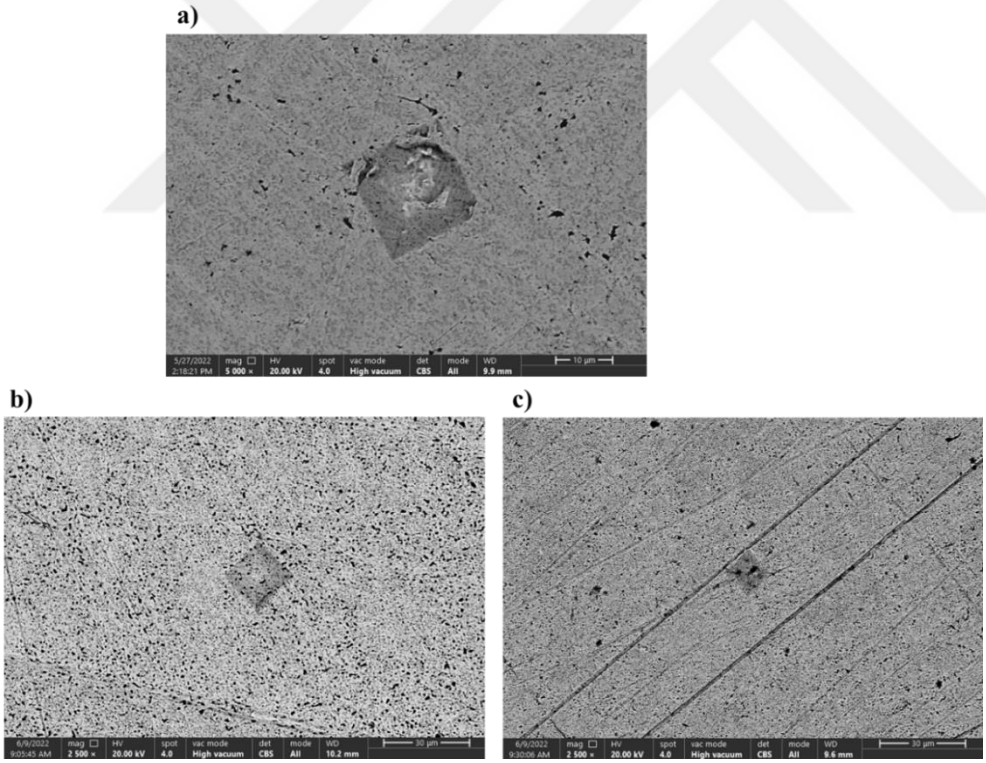

Figure 4.95 : SEM images of microhardness indentations for a) W1Ni, W1Ni-b) 1, c) 5 wt% NdB_6 at 2500X magnification.

SEM images of microhardness traces indentations for W1Ni and W1Ni-1, 5 wt% ErB_4 at 2500X magnification were shown in Figure 4.96. Traces were started to be smaller with increasing amount of ErB_4. Because of microhardness indentation of W1Ni-10 wt% ErB_4 was very small, it was not observed in microscope.

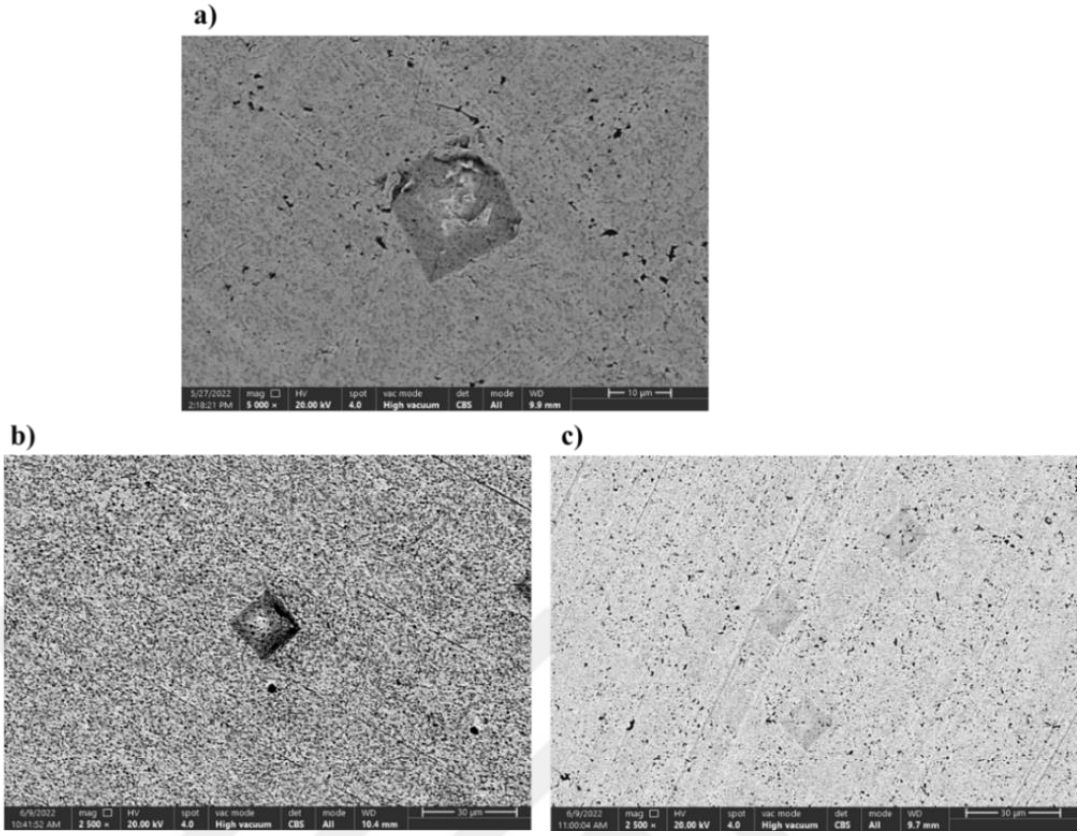

Figure 4.96 : SEM images of microhardness indentations for a) W1Ni, W1Ni-b) 1, c) 5 wt% ErB_4 at 2500X magnification.

Wear resistance test results were given in Table 4.7. As results, W1Ni composites had 0.832×10^{-4} mm^3 wear volume loss. After adding of boride particulates, wear resistance of all samples increased. For W1Ni-1, 5 and 10 wt% CeB_6 particulate reinforcing. Wear volume loss was 0.948, 0.673 and 0.21×10^{-4} mm^3, respectively. In addition, wear volume loss of W1Ni-1, 5 and 10 wt% NdB_6 particulate reinforcing samples were 1.088, 0.65 and 0.567×10^{-4} mm^3, respectively. Also, wear volume loss of W1Ni-1, 5 and 10 wt% ErB_4 particulate reinforcing samples were 1.77, 0.461 and 0.341×10^{-4} mm^3, respectively.

When relative wear volume loss was calculated, W1Ni-1 wt% ErB_4 SPS'd sample had the highest value, and W1Ni-10 wt% CeB_6 SPS'd sample had the lowest value. It was shown in Figure 4.97.

Table 4.7 : Wear resistance results of spark plasma sintered samples.

Samples	Wear Volume Loss (mm^3)×10^{-4}	Wear Rate (mm^3 N^{-1} m^{-1}) ×10^{-5}	Wear Friction	Relative Wear Volume Loss
W1Ni	0.832	0.104	0.345	1
W1Ni - 1 CeB_6	0.948	0.119	0.341	1,14
W1Ni - 5 CeB_6	0.673	0.084	0.325	0,81
W1Ni – 10 CeB_6	0.21	0.026	0.201	0,25
W1Ni – 1 NdB_6	1.088	0.136	0.332	1,31
W1Ni – 5 NdB_6	0.65	0.081	0.272	0,78
W1Ni – 10 NdB_6	0.567	0.071	0.479	0,68
W1Ni – 1 ErB_4	1.77	0.221	0.370	2,13
W1Ni – 5 ErB_4	0.461	0.058	0.244	0,55
W1Ni – 10 ErB_4	0.341	0.043	0.203	0,41

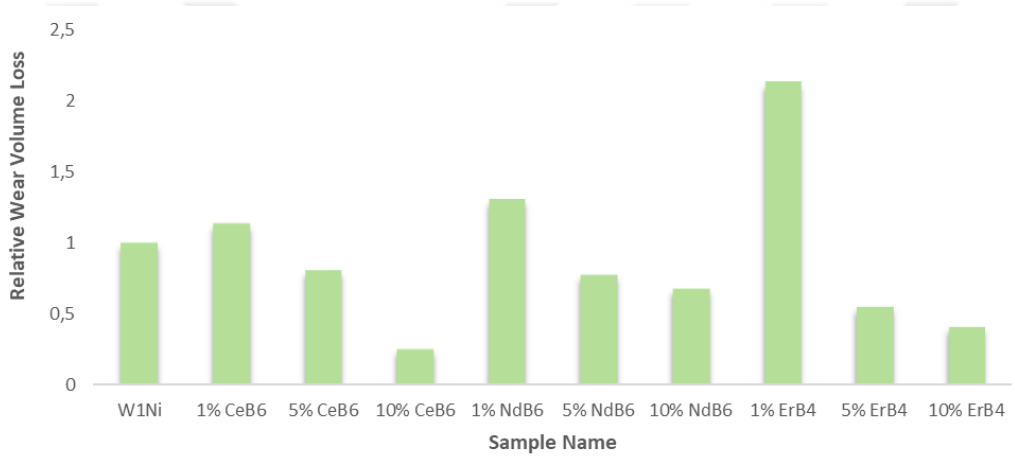

Figure 4.97 : Relative wear volume loss of spark plasma sintered samples.

Wear traces images in optical microscope of W1Ni and W1Ni-1 wt% CeB_6, 5 wt% CeB_6, 10 wt% CeB_6, 1 wt% NdB_6, 5 wt% NdB_6, 10 wt% NdB_6, 1 wt% ErB_4, 5 wt% ErB_4 and 10 wt% ErB_4 at 500 µm was shown in Figure 4.98. When images were compared with wear volume loss results that is shown in Table 4.7, W1Ni-10 wt% CeB_6 sample showed the lowest wear volume loss (0.21×10^{-4} mm^3).

Also, wear traces depth of W1Ni and W1Ni-1 wt% CeB_6, 5 wt% CeB_6, 10 wt% CeB_6, 1 wt% NdB_6, 5 wt% NdB_6, 10 wt% NdB_6, 1 wt% ErB_4, 5 wt% ErB_4 and 10 wt% ErB_4 was shown in Figure 4.99.

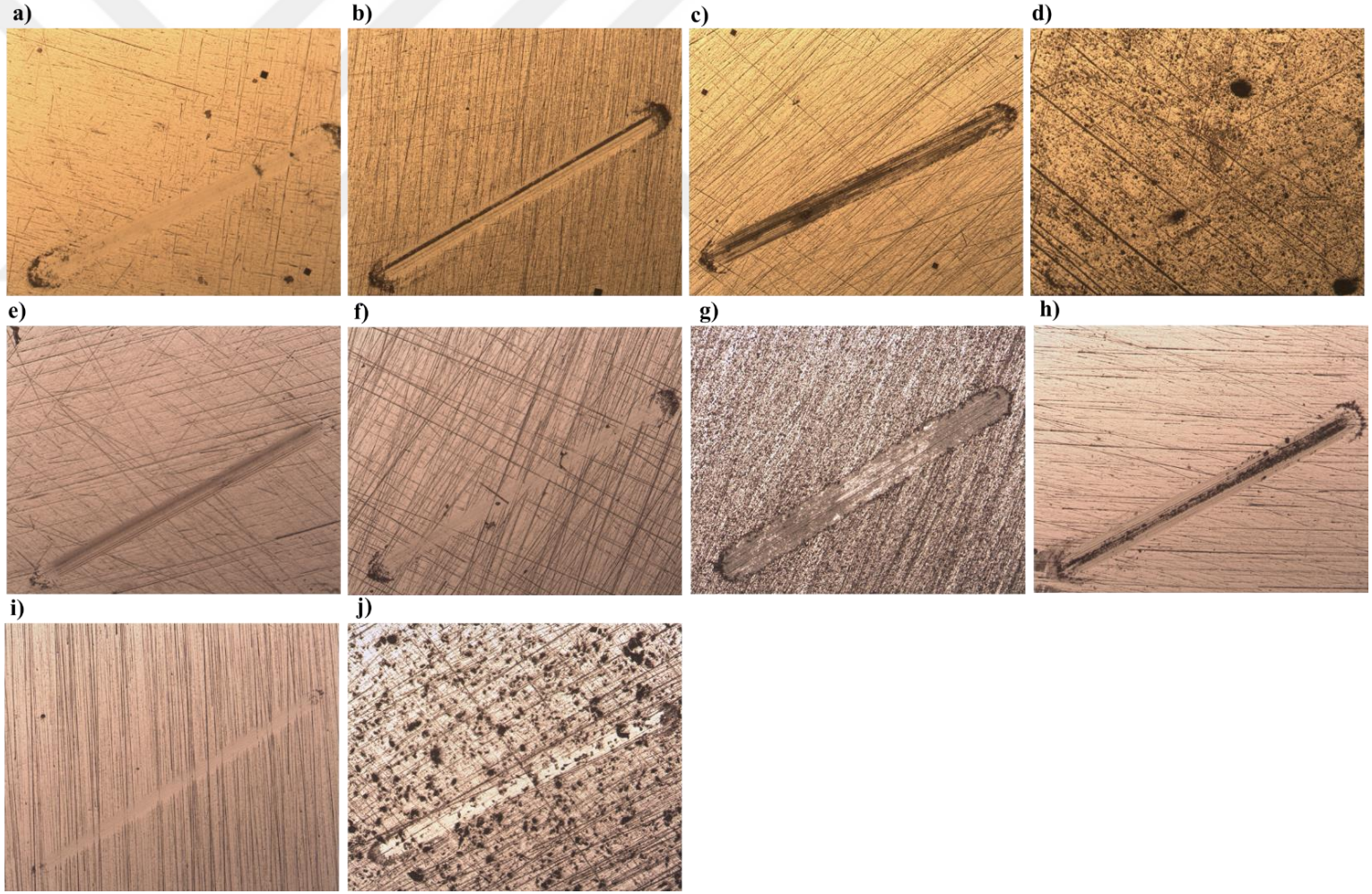

Figure 4.98 : Wear traces of a) W1Ni and W1Ni-b) 1 wt% CeB_6, c) 5 wt% CeB_6, d) 10 wt% CeB_6 e) 1 wt% NdB_6, f) 5 wt% NdB_6, g) 10 wt% NdB_6, h) 1 wt% ErB_4, i) 5 wt% ErB_4 and j) 10 wt% ErB_4 at 500 µm.

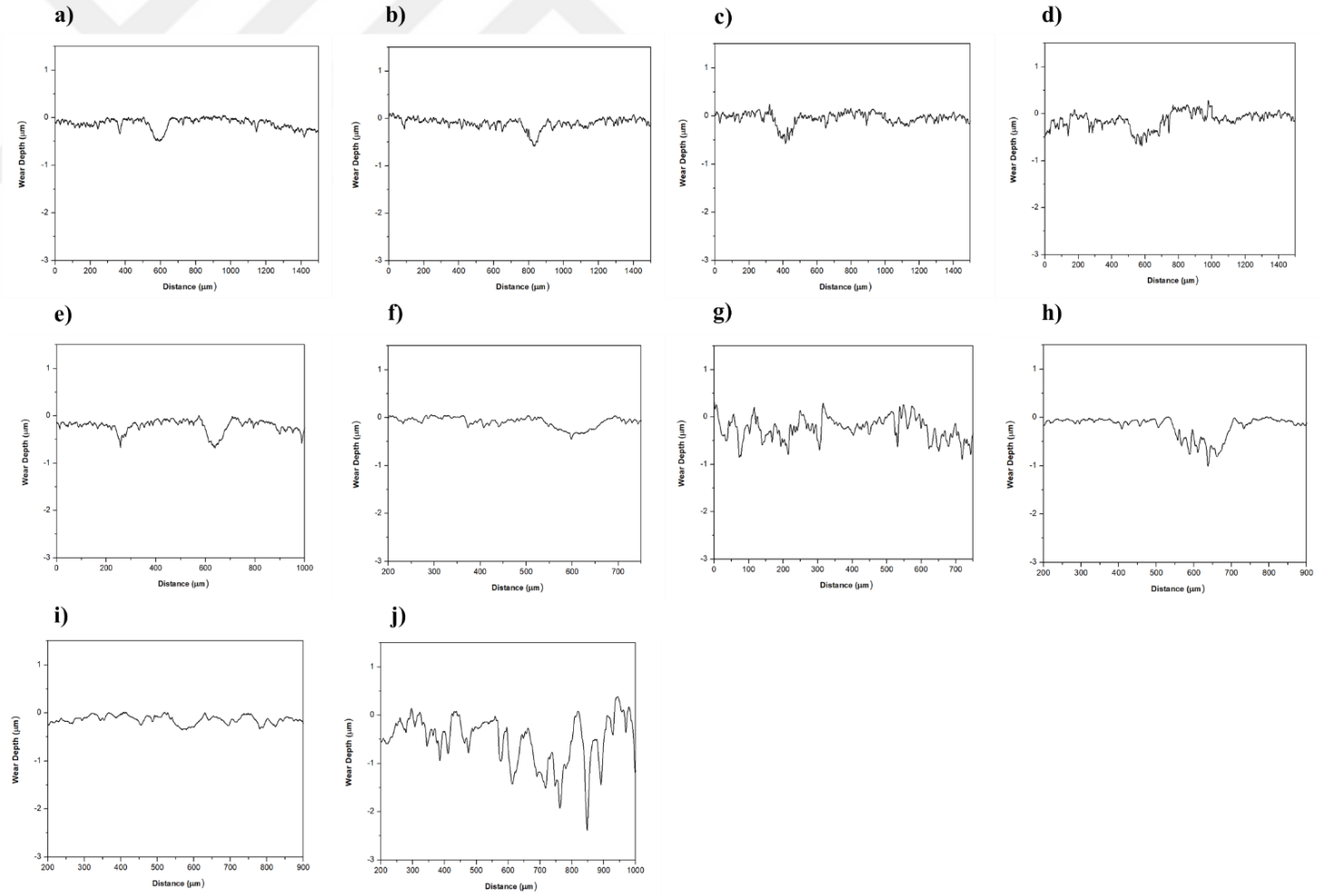

Figure 4.99 : Wear traces of a) W1Ni and W1Ni-b) 1 wt% CeB_6, c) 5 wt% CeB_6, d) 10 wt% CeB_6 e) 1 wt% NdB_6, f) 5 wt% NdB_6, g) 10 wt% NdB_6, h) 1 wt% ErB_4, i) 5 wt% ErB_4 and j) 10 wt% ErB_4.

Wear traces at high magnification (3000X) images for W1Ni-1 wt% NdB_6, 5 wt% NdB_6, 10 wt% NdB_6 were shown in Figure 4.100. Abrassive wear behaviour was observed in this structure.

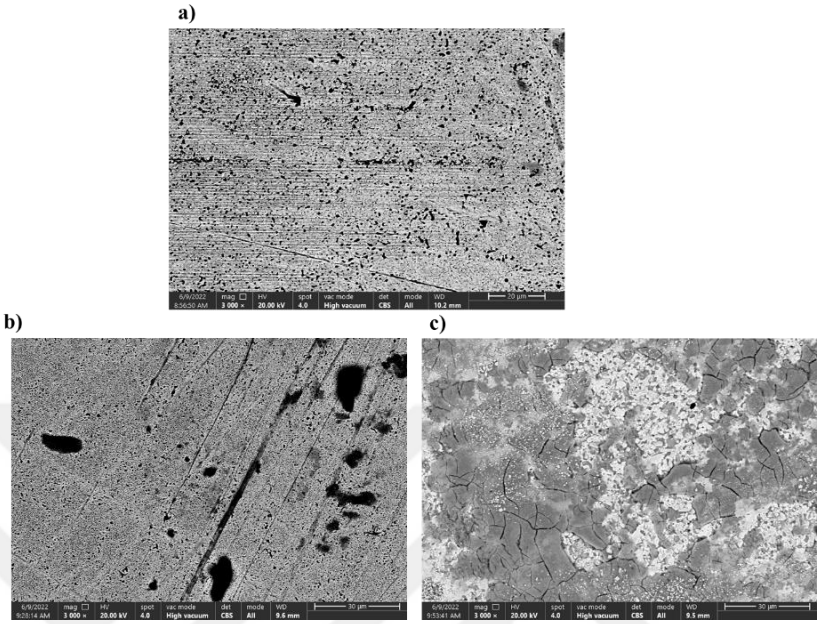

Figure 4.100 : Wear traces of W1Ni-a) 1 wt% NdB_6, b) 5 wt% NdB_6 and c) 10 wt% NdB_6 at 3000X magnification.

Wear traces at high magnification (3000X) images for W1Ni-1 wt% ErB_4, 5 wt% ErB_4 and 10 wt% ErB_4 were shown in Figure 4.101. Abrassive wear behaviour was observed in these structures.

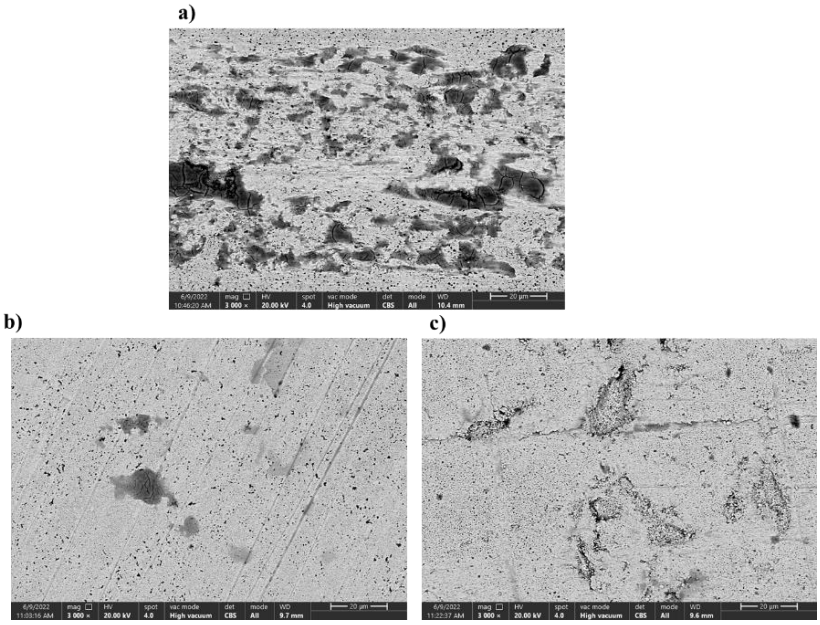

Figure 4.101 : Wear traces of W1Ni-a) 1 wt% ErB_4, b) 5 wt% ErB_4 and c) 10 wt% ErB_4 at 3000X magnification.

5. CONCLUSIONS

In this study, CeB_6, NdB_6 and ErB_4 rare-earth borides were produced with mechanochemical synthesis. Different milling time (0, 2, 3, 4, 5, 6, 7 and 8 h) and speed (920 and 1188 rpm) were tried for production. Also, 920 rpm and 5 h were used for mechanochemical synthesis. Then, pure boride powders were synthesized after HCl leaching process.

- After mechanochemical synthesis, MgO phase was came from reduction. This MgO phase was removed with HCl acid in purification part. According to XRD results, 4 M HCl acid was used for CeB_6 and NdB_6, however, 6 M HCl acid was used for ErB_4 due to remain MgO phase in 4 M leaching.
- Density of pure CeB_6, NdB_6 and ErB_4 powders were measured as 4.0882±0.007, 4.0304±0.015 and 6.1546±0.015 g/cm^3, respectively.
- Particle sizes of CeB_6, NdB_6 and ErB_4 powders were measured 109, 118.9 and 100.4 nm, respectively.
- When amount of B_2O_3 was decreased, NdB_4 phases started to be occur in NdB_6 reactions. In the XRD results, 30% loss of B_2O_3 gave the best results for production of pure NdB_4. Also, NdB_4 powder had 85.6 nm particle size and 5.0240±0.011 g/cm^3 density. In addition, NdB_4 and NdB_6 phases was produced at the same time with 20% loss of B_2O_3. Also, NdB_4 and NdB_6 powder had 136.6 nm particle size and 4.0911±0.003 g/cm^{3}density.

99 wt% W and 1 wt% Ni were mechanically alloyed for 800 rpm and 6 h. After that, different amounts of rare-earth boride powders (1, 2, 5 and 10 wt%) were added into W1Ni with 6 h mechanical alloying. Two different methods that are pressureless sintering (1400 ºC, 1 h) and spark plasma sintering (1410 ºC, 1 min) were used for consolidation of powders. After production, wear resistance, microhardness and He^+ irradiation tests were applied into samples.

- XRD patterns of W1Ni powders showed that four main W peaks were obtained with small amount of WC impurity. When the lattice strains increased, the crystallite sizes decreased because of the milling process.
- When amount of rare-earth boride particulate increased, density of W1Ni composite powders decreased. W1Ni had 16.8119±0.05 g/cm^3 density, it dropped to 13.2312±0.006 with W1Ni-10 wt% NdB_6.
- Adding with rare-earth boride particulate, particle size of powders was decreased. Also, lognormal distribution was obtained. The smallest particle size was measured as 65.2 nm for W1Ni-10 wt% NdB_6. When SEM and TEM results were determined, particle size of powders were nearly same with measurements. Powder morpohology was examined as mixed morphology.
- According to XRD results, four main W peaks were obtained with other smallest peaks after pressureless sintering. However, W_2B was started to be main phase after adding 5 wt% rare-earth borides.
- The highest density was obtained for W1Ni reinforcing with 10 wt% NdB_6 particulates SPS sample that had 100% relative density with measuring Archimedes' principle.
- Three different phases were observed in SEM images as grey, black and white color. W was always high for all areas. However, grey, black and white areas was determined as Ni, rare-earth boride and W rich areas.
- The PS'd W1Ni sample reinforced with 2 wt% CeB_6 particulates had the highest value (6,796 ± 0.085 GPa) and the lowest wear volume loss (0.992×10^{-4} mm^3).
- The SPS'd W1Ni sample reinforced with 10 wt% ErB_4 particulates had the highest value (21.16±0.72 GPa). The SPS'd W1Ni sample reinforced with 10 wt% ErB_4 particulates had the lowest wear volume loss (0.341×10^{-4} mm^3).
- After He^+ irradiation tests, XRD peaks of W1Ni and all reinforced with 2 wt% CeB_6, NdB_6, ErB_4 and 5 wt% ErB_4 pressureless sintered samples were shifting to right. Also, XRD peaks of reinforced with W1Ni-1 wt% CeB_6, NdB_6, ErB_4, 5 wt% CeB_6, NdB_6 and 10 wt% ErB_4 pressureless sintered samples were shifting to left side. While W1Ni-5 wt% NdB_6 pressureless sintered sample

gave high deformation on surface, W1Ni-2 wt% CeB_6 pressureless sintered sample had less surface deformation after irradiation test as SEM images results.

- Properties of W1Ni composite material was improved with adding rare-earth boride particulates. Enhanced hardness and wear resistance properties were achieved for potential high-temperature applications and fusion reactor applications.

REFERENCES

[1] **X. Kong, H. Wang, N. Li, H. Mu,** (2022). Multi-objective optimal allocation and performance evaluation for energy storage in energy systems, *Energy. 253 124061*. https://doi.org/https://doi.org/10.1016/j.energy.2022.124061.

[2] **Z. Fareed, U.K. Pata,** (2022). Renewable, non-renewable energy consumption and income in top ten renewable energy-consuming countries: Advanced Fourier based panel data approaches, *Renew. Energy. 194 805–821*. https://doi.org/https://doi.org/10.1016/j.renene.2022.05.156.

[3] **Z. Li, R. Luan, B. Lin,** (2022). The trend and factors affecting renewable energy distribution and disparity across countries, *Energy. 254 124265*. https://doi.org/https://doi.org/10.1016/j.energy.2022.124265.

[4] **T.H. Le,** (2022). Connectedness between nonrenewable and renewable energy consumption, economic growth and CO2 emission in Vietnam: New evidence from a wavelet analysis, *Renew. Energy. 195 442–454*. https://doi.org/https://doi.org/10.1016/j.renene.2022.05.083.

[5] **T.E.G. Nicholas, T.P. Davis, F. Federici, J. Leland, B.S. Patel, C. Vincent, S.H. Ward,** (2021). Re-examining the role of nuclear fusion in a renewables-based energy mix, *Energy Policy. 149 112043*. https://doi.org/https://doi.org/10.1016/j.enpol.2020.112043.

[6] **A.S. Annuar, R.A. Rahman, A. Munir, A. Murad, H.A. El-enshasy, R. Illias,** (2021). Recent progress in Chinese fusion research based on superconducting tokamak configuration, *Carbohydr. Polym. 118159*. https://doi.org/10.1016/j.xinn.2022.100269.

[7] **URL-1**|<No Title, (n.d.) https://interestingengineering.com/nuclear-fusion-.

[8] **URL-2**|<No Title, (n.d.) https://funginstitute.berkeley.edu/news/op-ed-fusi.

[9] **URL-3**|<No Title, (n.d.) https://www.twi-global.com/technical-knowledge/faq.

[10] **J.W. Coenen, J. Riesch, J.-H. You, H. Gietl, T. Hoeschen, R. Neu, B. Jasper, Y. Mao, A. Terra, C. Linsmeier, S. Sree, C. Broeckmann,** (2018). Tungsten Composite Materials for Fusion First Wall Applications, https://inis.iaea.org/search/search.aspx?orig_q=RN:50012702 (accessed June 26, 2022).

[11] **R.A. Pitts, S. Carpentier, F. Escourbiac, T. Hirai, V. Komarov, A.S. Kukushkin, S. Lisgo, A. Loarte, M. Merola, R. Mitteau, A.R. Raffray, M. Shimada, P.C. Stangeby,** (2011). Physics basis and design of the ITER plasma-facing components, *J. Nucl. Mater. 415 957–S964*.https://doi.org/https://doi.org/10.1016/j.jnucmat.2011.01.114.

[12] **B.G. Hong,** (2021). Improvements to physics performance and engineering technology required for a tokamak fusion reactor, *Fusion Eng. Des. 162 112116*.https://doi.org/https://doi.org/10.1016/j.fusengdes.2020. 112116.

[13] **Y. Xu, Y. Xu, Z. Wu, L. Luo, X. Zan, G. Yao, Y. Xi, Y. Wang, X. Ding, H. Bi, X. Zhu, Q. Xu, J. Wu, Y. Wu,** (2021). Plasma-surface interaction experimental device: PSIEC and its first plasma exposure experiments on bulk tungsten and coatings, *Fusion Eng. Des. 164 1–7*. https://doi.org/10.1016/j.fusengdes.2020.112198.

[14] **J. Riesch, A. Feichtmayer, J.W. Coenen, B. Curzadd, H. Gietl, T. Höschen, A. Manhard, T. Schwarz-Selinger, R. Neu,** (2022). Irradiation effects in tungsten—From surface effects to bulk mechanical properties, *Nucl. Mater. Energy 30 101093*. https://doi.org/10.1016/j.nme.2021.101093.

[15] **P. Mertens, V. Thompson, G.F. Matthews, D. Nicolai, G. Pintsuk, V. Riccardo, S. Devaux, B.** (2013). Sieglin, Bulk tungsten in the JET divertor: Potential influence of the exhaustion of ductility and grain growth on the lifetime, *J. Nucl. Mater. 438 401–S405*. https://doi.org/10.1016/j.jnucmat.2013.01.080.

[16] **K. Zhang, A. von Müller, H. Greuner, J.H. You,** (2020). Stress analysis of divertor plasma-facing component designs using tungsten particle-reinforced copper composite heat sink, *Fusion Eng. Des. 154 111510*. https://doi.org/10.1016/j.fusengdes.2020.111510.

[17] **H.C. Kim, E. Bang, N. Kwak, Y. Oh, H.N. Han, H. Choi, K. Kim, S.H. Hong,** (2019). Thermal and microstructural properties of spark plasma sintered tungsten for the application to plasma facing materials, *Fusion Eng. Des. 146 2649–2653*. https://doi.org/10.1016/j.fusengdes. 2019.04.071.

[18] **S. Nogami, I. Ozawa, D. Asami, N. Matsuta, S. Nakabayashi, S. Baumgärtner, P. Lied, K. Yabuuchi, T. Miyazawa, Y. Kikuchi, M. Wirtz, M. Rieth, A. Hasegawa,** (2022). Tungsten–tantalum alloys for fusion reactor applications, *J. Nucl. Mater. 566 153740*. https://doi.org/https://doi.org/10.1016/j.jnucmat.2022.153740.

[19] **L. E., S. W.D., (**1999). Tungsten: Properties, Chemistry, Technology of the Element, *Alloys and Chemical Compounds*.

[20] **G.-M. Song, Y.-J. Wang, Y. Zhou,** (2002). The mechanical and thermophysical properties of ZrC/W composites at elevated temperature, *Mater. Sci. Eng. A. 334 223–232*. https://doi.org/https://doi.org/10.1016/S0921-5093(01)01802-0.

[21] **C. Linsmeier, B. Unterberg, J.W. Coenen, R.P. Doerner, H. Greuner, A. Kreter, J. Linke, H. Maier,** (2017). Material testing facilities and programs for plasma-facing component testing, *Nucl. Fusion. 57 92012*. https://doi.org/10.1088/1741-4326/aa4feb.

[22] **X. Li, M. Zhang, G. Zhang, S. Wei, L. Xu, Y. Zhou,** (2022). Effect of spark plasma sintering temperature on structure and performance characteristics of Cu-20wt%W composite, *J. Alloys Compd. 912 165246.* https://doi.org/10.1016/j.jallcom.2022.165246.

[23] **A. Seyyedi, H. Abdoos,** (2022). An examination of microstructure and dry wear properties of Nano-Y2O3 incorporated in fine-grained W-Ni-Cu alloy prepared by conventional and spark plasma sintering, *Int. J. Refract. Met. Hard Mater. 102 105728*. https://doi.org/10.1016/j.ijrmhm.2021.105728.

[24] **S. Coskun, M.L. Övecoglu,** (2010). Microstructural characterizations of Ni activated sintered W – 2 wt % TiC composites produced via mechanical alloying, *497 80–89*. https://doi.org/10.1016/j.jallcom.2010.03.008.

[25] **A. Genç, S. Coskun, M.L. Öveçoglu,** (2010). Decarburization of TiC in Ni activated sintered W – x TiC (x = 0, 5, 10, 15 wt %) composites and the effects of heat treatment on the microstructural and physical properties, Int. J*ournal of Refractory Metals & Hard Materials 28 451–458*. https://doi.org/10.1016/j.ijrmhm.2010.02.004.

[26] **Ö.U. Demirkan, A. Genç, M. Lütfi,** (2012). Effects of Al2O3 addition on the microstructure and properties of Ni activated sintered W matrix composites, *Int. Journal of Refractory Metals and Hard Materials 32 33–38.* https://doi.org/10.1016/j.ijrmhm.2012.01.004.

[27] **H. Gökçe, Ö. Balci, D. A, Ö.U. Demirkan, A. Genç, M.L. Öveçoglu,** (2013). Characterization Investigations of W Ni Matrix Composites Reinforced with TiB2 and La2O3, *123 309–312*. https://doi.org/10.12693/APhysPolA.123.309.

[28] **A. Duygu, Ö. Balci, H. Gökçe, M. Lüt, İ. Duman**, (2013). Comparative investigations of the activated sintered W – 1 wt.% Ni composites reinforced with various oxide and boride particles, *Int. Journal of Refractory Metals and Hard Materials 41 577–584*. https://doi.org/10.1016/j.ijrmhm.2013.07.010.

[29] **Z.L. Lu, L.M. Luo, J.B. Chen, X.M. Huang, J.G. Cheng, Y.C. Wu,** (2015). Fabrication of W-Cu/CeO2 composites with excellent electric conductivity and high strength prepared from copper-coated tungsten and Ceria powders, *Mater. Sci. Eng. A. 626 61–66.* https://doi.org/10.1016/j.msea.2014.12.047.

[30] **D. Agaogulları, Ö. Balcı, M.L. Öveçoglu,** (2017). Effect of milling type on the microstructural and mechanical properties of W-Ni-ZrC-Y2O3 composites, *Ceram. Int. 43 7106–7114*. https://doi.org/10.1016/j.ceramint.2017.02.142.

[31] **Ö. Balcı, D. Ağaoğulları, M.S. Somer, M.L. Öveçoğlu,** (2020). Effect of Ambient and Cryogenic Milling on the Microstructure and Properties of Tungsten Matrix Composites Fabricated by Activated Sintering, *Cumhur. Sci. J. 41 160–168.*

[32] **A. Genç, S. Coskun, M.L. Öveçoglu,** (2010). Fabrication and properties of mechanically alloyed and Ni activated sintered W matrix composites reinforced with Y2O3 and TiB2 particles, *61*. https://doi.org/10.1016/j.matchar.2010.04.006.

[33] **H. Cui, N. Liu, L. Luo, Y. Xu, J. Cheng, Y. Wu,** (2022). A prospect of using ternary W-5 wt%V-5 wt%Ta alloy manufactured by mechanical alloying and spark plasma sintering as plasma-facing material, *J. Alloys Compd. 903 163899*. https://doi.org/10.1016/j.jallcom.2022.163899.

[34] **H. Materials, V.R. Talekar, A. Patra, S.K. Sahoo, S.K. Karak, B. Mishra,** (2019). Fabrication and characterization of nano-Y2O3, Al2O3, La2O3 dispersed mechanically alloyed and liquid phase sintered W-Ni for structural application, *Int. J. Refract. Metals Hard Mater. 82 183–198.* https://doi.org/10.1016/j.ijrmhm.2019.03.027.

[35] **G. Yao, X.P. Liu, Z.Y. Zhao, Z.H. Zhao, L.M. Luo, J.G. Cheng, X. Zan, Q. Xu, Y.C. Wu,** (2022). Evaluating surface damage behavior of W-(Y0.9La0.1)2O3 composites during spark plasma sintering process improvement, *J. Nucl. Mater. 558153322*. https://doi.org/10.1016/ j. jnucmat.2021.153322.

[36] **Y.F. Zhou, Z.Y. Zhao, X.Y. Tan, L.M. Luo, Y. Xu, X. Zan, Q. Xu, K. Tokunaga, X.Y. Zhu, Y.C. Wu,** (2019). Densification and microstructure evolution of W-TiC-Y2O3 during spark plasma sintering, *Int. J. Refract. Met. Hard Mater. 79 95–101*. https://doi.org/10.1016/j.ijrmhm.2018.11.014.

[37] **Y.X. Zhang, X.Y. Tan, L.M. Luo, Y. Xu, X. Zan, Q. Xu, K. Tokunaga, X.Y. Zhu, Y.C. Wu,** (2019). Combined effect of laser thermal shock and helium ion irradiation on W-Y2O3 composites, *Fusion Eng. Des. 140 102–106.* https://doi.org/10.1016/j.fusengdes.2019.01.134.

[38] **D. Ovalı, D. Ağaoğulları, M.L. Öveçoğlu**, (2020). Effects of oxide particles on the microstructural and mechanical properties of W-Ni-WB composites, *An Int. J. 38 347–353.*

[39] **D.G. Liu, P. Zhang, C.F. Ruan, L. Meng, L.M. Luo, Z.M. Wang, Y.C. Wu,** (2021). Fabrication and characterization of W/Cu/Ni-based high specific gravity alloy with Zr and Ti combined addition, *Int. J. Refract. Met. Hard Mater. 101 105674.* https://doi.org/10.1016/j.ijrmhm. 2021.105674.

[40] **H. Cui, N. Liu, L. Luo, Y. Xu, J. Cheng, Y. Wu,** (2021). Behavior of high-entropy W-rich alloys Wx(TaVCrTi)y under He+ irradiation, *Fusion Eng. Des. 172 112904.* https://doi.org/10.1016/j.fusengdes.2021. 112904.

[41] **J.S. Benjamin,** (1970). Dispersion strengthened superalloys by mechanical alloying, *Metall. Trans.*. https://doi.org/10.1007/BF03037835.

[42] **D.A. BOOZ, T.J. Kondis,** (1978). Method of producing metal flake, *Alum. Corp. Am.*

[43] **C. Suryanarayana,** (2004). Mechanical alloying and milling, *Mech. Alloy. Milling. 1–472*. https://doi.org/10.4150/kpmi.2006.13.5.371.

[44] **C. Li, R.M. German,** (1983). The properties of tungsten processed by chemically activated sintering, *Metall. Trans. A. 14 2031–2041*. https://doi.org/10.1007/BF02662370.

[45] **H.W. Hayden, J.H. Brophy,** (1963). The Activated Sintering of Tungsten with Group {VIII} Elements, *J. Electrochem. Soc. 110 805*. https://doi.org/10.1149/1.2425876.

[46] **S. Kim, S. Lee, Y. Do Kim, I. Moon,** (2003). High temperature compressive deformation and fracture characteristics of the activated sintered W – Ni compacts, *21 183–192*. https://doi.org/10.1016/S0263-4368(03)00031-3.

[47] **R.M. German,** (1996). Sintering Theory and Practice.

[48] **G. V Samsonov, V.I. Yakovlev,** (1969). Activation of the sintering of tungsten by the iron-group metals, *Sov. Powder Metall. Met. Ceram. 8 804–808.* https://doi.org/10.1007/BF00778338.

[49] **I.J. Toth, N.A. Lockington,** (1967). The kinetics of metallic activation sintering of tungsten, *J. Less Common Met. 12 353–365.* https://doi.org/https://doi.org/10.1016/0022-5088(67)90003-3.

[50] **B.C.W. Corti,** (1986). Sintering Aids in Powder Metallurgy, *184–195.*

[51] **O.A. Waseem, H.J. Ryu, (**2016). Tungsten-Based Composites for Nuclear Fusion Applications, in: R.O.A. Rahman, H.E.-D.M. Saleh (Eds.), *Nucl. Mater. Perform.*, IntechOpen, Rijeka, https://doi.org/10.5772/62434.

[52] **D. Neov, L. Slavov, A.A. Donkov, M.N. Mirzayev, E. Popov, E. Demir, K. Siemek, N. Djourelov, V.A. Turchenko, Z.A. Sharipov, P. Horodek, A.I. Beskrovnyi, A.H. Valizade, O.A. Samedov, A. Vladescu, K. Krezhov, I. Felicia,** (2022). Structural study of W2B obtained via mechanical alloying of W, B4C, TiC and graphite before and after He ions irradiation, *Nucl. Mater. Energy. 31 101201.* https://doi.org/10.1016/j.nme.2022.101201.

[53] **K.E. SPEAR, (**1976). Phase Behavior and Related Properties of Rare-Earth Borides, in: Phase Diagrams, *Elsevier, pp. 91–159.* https://doi.org/10.1016/B978-0-12-053204-9.50010-2.

[54] **T. Mori,** (2009). Novel physical properties of rare earth higher borides, *J. Phys. Conf. Ser. 176* https://doi.org/10.1088/1742-6596/176/1/012036.

[55] **X.H. Ji, Q.Y. Zhang, J.Q. Xu, Y.M. Zhao,** (2011). Rare-earth hexaborides nanostructures: Recent advances in materials, characterization and investigations of physical properties, *Prog. Solid State Chem. 39 51–69*. https://doi.org/10.1016/j.progsolidstchem.2011.04.001.

[56] **L.W. Swanson, D.R. McNeely,** (1979). Work functions of the (001) face of the hexaborides of Ba, La, Ce and Sm, *Surf. Sci. 83 11–28*. https://doi.org/10.1016/0039-6028(79)90477-1.

[57] **C. Fu, J. Xu, Y. Chang, Q. Wang, Y. Wang, B. Yu, P. Guo, J. Xu, H. Sun, Y. Luo, J. Liu,** (2017). Flexible three-dimensional CeB6 nanowire arrays and excellent field emission emitters, *J. Alloys Compd. 729 997–1003.* https://doi.org/10.1016/j.jallcom.2017.09.240.

[58] **J.K. Sonber, T.S.R.C. Murthy, K. Sairam, B. Paul, J.K. Chakravartty,** (2016). Effect of TiSi2 addition on densification of Cerium hexaboride, *Ceram. Int. 42 891–896.* https://doi.org/10.1016/j.ceramint. 2015.09.015.

[59] **C.Y. Zou, Y.M. Zhao, J.Q. Xu,** (2006). Synthesis of single-crystalline CeB6 nanowires, *J. Cryst. Growth. 291 112–116.* https://doi.org/10.1016/ j.jcrysgro.2006.02.042.

[60] **M. Zhang, X. Wang, X. Zhang, P. Wang, S. Xiong, L. Shi, Y. Qian,** (2009). Direct low-temperature synthesis of RB6 (R=Ce, Pr, Nd) nanocubes and nanoparticles, *J. Solid State Chem. 182 3098–3104.* https://doi.org/10.1016/j.jssc.2009.08.032.

[61] **A. Aprea, A. Maspero, N. Masciocchi, A. Guagliardi, A.F. Albisetti, G. Giunchi,** (2013). Nanosized rare-earth hexaborides: Low-temperature preparation and microstructural analysis, *Solid State Sci. 21 32–36.* https://doi.org/10.1016/j.solidstatesciences.2013.04.001.

[62] **K. Amalajyothi, L.J. Berchmans, S. Angappan, A. Visuvasam,** (2008). Electrosynthesis of cerium hexaboride by the molten salt technique, *J. Cryst. Growth. 310 3376–3379.* https://doi.org/https://doi.org/10.1016/ j. jcrysgro.2008.04.026.

[63] **M. Jha, R. Patra, S. Ghosh, A.K. Ganguli,** (2013). Vertically aligned nanorods of lanthanum hexaboride with efficient field emission properties, *Solid State Commun. 153 35–39.* https://doi.org/https://doi.org/10.1016/ j.ssc.2012.10.007.

[64] **Z. DOU, T. ZHANG, Y. GUO, J. HE,** (2012). Research on preparation optimization of nano CeB6 powder and its high temperature stability, *J. Rare Earths. 30 1129–1133.* https://doi.org/https://doi.org/10.1016/ S1002-0721(12)60192-6.

[65] **Y. Tanaka, U. Staub, Y. Narumi, K. Katsumata, V. Scagnoli, S. Shimomura, Y. Tabata, Y. Onuki,** (2004). Non-resonant X-ray Bragg diffraction by CeB6, *Phys. B Condens. Matter. 345 78–81.* https://doi.org/https://doi.org/10.1016/j.physb.2003.11.025.

[66] **H. Okamoto,** (2015). Supplemental Literature Review of Binary Phase Diagrams: Ag-Co, Ag-Er, Ag-Pd, B-Ce, Bi-La, Bi-Mn, Cu-Ge, Cu-Tm, Er-Y, Gd-Tl, H-La, and Hg-Te, J. *Phase Equilibria Diffus. 36 10–21.* https://doi.org/10.1007/s11669-014-0341-7.

[67] **T.S.R.C. Murthy, J.K. Sonber, K. Sairam, R.D. Bedse, J.K. Chakarvartty,** (2016). Development of Refractory and Rare Earth Metal Borides & Carbides for High Temperature Applications, *Mater. Today Proc. 3 3104–3113.* https://doi.org/10.1016/j.matpr.2016.09.026.

[68] **G. Bliznakov, P. Peshev,** (1964). The preparation of cerium, praseodymium, and neodymium hexaborides, *J. Less Common Met. 7 441–446.* https://doi.org/https://doi.org/10.1016/0022-5088(64)90041-4.

[69] **Z. DOU, T. ZHANG, Y. LIU, Y. GUO, J. HE,** (2011). Preparation of CeB6 nano-powders by self-propagating high-temperature synthesis (SHS), *J. Rare Earths 29 986–990.* https://doi.org/https://doi.org/10.1016/S1002-0721(10)60583-2.

[70] **L. Koroglu, E. Ayas,** (2020). In-situ synthesis and densification of CeB6 ceramics by spark plasma sintering from CeO2 and B powders: Effect of boron content and boron particle size on microstructural, mechanical and electrical properties, *Mater. Chem. Phys. 240 122253.* https://doi.org/10.1016/j.matchemphys.2019.122253.

[71] **G. Balakrishnan, M. Lees, D.M. Paul,** (2004). Rare earth hexaborides: large single crystals, *J. Magn. Magn. Mater. 272–276 601–602*. https://doi.org/10.1016/j.jmmm.2003.12.1390.

[72] **S. Otani, H. Nakagawa, Y. Nishi, N. Kieda,** (2000). Floating Zone Growth and High Temperature Hardness of Rare-Earth Hexaboride Crystals: LaB6, CeB6, PrB6, NdB6, and SmB6, *J. Solid State Chem. 154 238–241*. https://doi.org/https://doi.org/10.1006/jssc.2000.8842.

[73] **P.K. Liao, K.E. Spear, M.E. Schlesinger,** (1996). The B-Nd (boron-neodymium) system, *J. Phase Equilibria. 17 335–339.* https://doi.org/10.1007/BF02665560.

[74] **Y. Liu, W.J. Lu, J.N. Qin, D. Zhang,** (2007). A new route for the synthesis of NdB6 powder from Nd2O3-B4C system, *J. Alloys Compd. 431 337–341*. https://doi.org/10.1016/j.jallcom.2006.05.084.

[75] **J.K. Sonber,** (2016). Effect of NdB_6 addition on densification and properties of ZrB_2, *Ceram. - Silikaty. 41–47*. https://doi.org/10.13168/cs.2016.0006.

[76] **M. Reiffers, J. Šebek, E. Šantavá, N. Shitsevalova, S. Gabáni, G. Pristáš, K. Flachbart,** (2007). Heat capacity of NdB6, *J. Magn. Magn. Mater. 310.* https://doi.org/10.1016/j.jmmm.2006.10.587.

[77] **Z.-H. Dou, T.-A. Zhang, S.-G. Fan, Q.-Y. Huang, J.-L. Zhang, H.-Y. Xiao, N. Fu,** (2015). A new method of preparing NdB6 ultra-fine powders, *Rare Met.* https://doi.org/10.1007/s12598-015-0596-0.

[78] **T. Simsek, B. Avar, S. Ozcan, B. Kalkan,** (2019). Nano-sized neodymium hexaboride: Room temperature mechanochemical synthesis, *Phys. B Condens. Matter. 570 217–223.* https://doi.org/10.1016/j.physb.2019.06.047.

[79] **W. Han, H. Zhang, J. Chen, Y. Zhao, Q. Fan, Q. Li,** (2015). Synthesis of single-crystalline NdB6 submicroawls via a simple flux-controlled self-catalyzed method, *RSC Adv. 5 12605–12612.* https://doi.org/10.1039/c4ra13129k.

[80] **Q. Fan, Q. Zhang, Y. Zhao, Q. Ding,** (2013). Field emission from one-dimensional single-crystalline NdB6 nanowires, *J. Rare Earths. 31 145–148.* https://doi.org/10.1016/S1002-0721(12)60248-8.

[81] **X. Zhao, X. Liu, F. Lin, W. Liu, W. Su,** (1997). A new route for the synthesis of boron-rich rare-earth boride NdB6 under high pressure and high temperature, *J. Alloys Compd. 249 247–250.* https://doi.org/10.1016/S0925-8388(96)02856-3.

[82] **S. Michimura, A. Shigekawa, F. Iga, M. Sera, T. Takabatake, K. Ohoyama, Y. Okabe,** (2006). Magnetic frustrations in the Shastry-Sutherland system ErB4, *Phys. B Condens. Matter. 378–380 596–597.* https://doi.org/10.1016/j.physb.2006.01.161.

[83] **R.W. Mar, N.D. Stout,** (1974). Melting temperature and high-temperature enthalpies of erbium tetraboride, *J. Chem. Thermodyn. 6 943–947.* https://doi.org/https://doi.org/10.1016/0021-9614(74)90215-8.

[84] **P.K. Liao, K.E. Spear, M.E. Schlesinger,** (1996). The B-Er (Boron-Erbium) System, *J. Phase Equilibria 17 326–329.*

[85] **V. V. Novikov, A. V. Morozov, A. V. Matovnikov, N. V. Mitroshenkov, D. V. Avdashchenko, S. V. Kuznetsov, B.I. Kornev, O.A. Marakhina, V. V. Novikov, E.O. Bordacheva,** (2013). The properties of lattice, electronic and magnetic subsystems of erbium tetraboride based on calorimetric data at temperatures of 2-300 *K, J. Alloys Compd. 581 431–434.* https://doi.org/10.1016/j.jallcom.2013.07.074.

[86] **D. Ağaoğulları, Ö. Balcı, N. Akçamlı, C. Suryanarayana, İ. Duman, M. Öveçoğlu,** (2019). Mechanochemical synthesis and consolidation of nanostructured cerium hexaboride, *Process. Appl. Ceram. 13 32–43.* https://doi.org/10.2298/PAC1901032A.

[87] **D. Ağaoğullari, Ö. Balci, M.L. Öveçoğlu, C. Suryanarayana, I. Duman,** (2015)**.** Synthesis of bulk nanocrystalline samarium hexaboride, *J. Eur. Ceram. Soc. 35 4121–4136.* https://doi.org/10.1016/j.jeurceramsoc. 2015.07.037.

[88] **S. Sugiyama, H. Taimatsu,** (2004). Mechanical properties of WC-WB-W2B composites prepared by reaction sintering of B4C-W-WC powders, *J. Eur. Ceram. Soc. 24 871–876.* https://doi.org/10.1016/S0955-2219(03)00253-X.

[89] **M. Athanasakis, E. Ivanov, E. del Rio, S.A. Humphry-Baker,** (2020). A high temperature W2B–W composite for fusion reactor shielding, *J. Nucl. Mater. 532 152062*. https://doi.org/10.1016/j.jnucmat.2020.152062.

[90] **Z. Qin, W. Gong, X. Song, M. Wang, H. Wang, Q. Li,** (2018). Effect of pressure on the structural, electronic and mechanical properties of ultraincompressible W2B, *RSC Adv. 8 35664–35671.* https://doi.org/10.1039/c8ra05706k.

CURRICULUM VITAE

Name Surname **:** Burçak BOZTEMUR

EDUCATION **:**

Bachelor's Degree **:** 2020. Istanbul Technical University. Faculty of Chemical and Metallurgical Engineering. Metallurgical and Materials Engineering

Master's Degree **:** Istanbul Technical University. Department of Materials Science and Engineering. Ceramic Engineering Programme

PROFESSIONAL EXPERIENCE AND REWARDS:

- 2020-2022 Istanbul Technical University at the Particulate Materials Laboratory (PML)
- 2020-2022 Istanbul Technical University at TÜBİTAK 119M980 project
- 2022 Istanbul Technical University at Prof. Dr. Adnan Tekin Materials Science and Production Technologies Applied Research Center (ATARC)

PUBLICATIONS. PRESENTATIONS AND PATENTS ON THE THESIS:

- **Boztemur B.,** Alkraidi A., Öveçoğlu M.L., Ağaoğulları. D. 2022: Characterization Studies of W-1 wt% Ni Matrix Composites Reinforced with CeB_6 Particulates by Powder Metallurgy Methods. International Graduate Research Symposium. June 1-3. 2022 Istanbul. Turkey.